PHOTONIC CRYSTAL SURFACE EMITTING LASERS

by

AKHIL RAJ KUMAR KALAPALA

Presented to the Faculty of the Graduate School of
The University of Texas at Arlington
in Partial Fulfillment of the Requirements
for the Degree of

DOCTOR OF PHILOSOPHY

in

ELECTRICAL ENGINEERING

THE UNIVERSITY OF TEXAS AT ARLINGTON

May 2022

Doctoral Committee:

Professor Weidong Zhou, Chair
Professor James Coleman
Professor Catrina Coleman
Professor Yuze Alice Sun
Professor Michael Vasilyev

Dedicated to my soulmate Krishna Bhavana Sivaraju

Acknowledgements

"It is not all about the destination, trust the journey, for the journey shapes you"

Abstract

Photonic Crystal Surface Emitting Lasers

Akhil Raj Kumar Kalapala, PhD

The University of Texas at Arlington, 2022

Supervising Professor: Weidong Zhou

Since the initial proposal in 1999 by Noda *et al.*, photonic crystal surface emitting lasers (PCSELs) have proven to achieve large area, coherent lasing with a narrow, single mode beam. Owing to their unique orthogonal electrical/optical cavity scheme, PCSELs have emerged as one of the most promising platforms for high power diode lasers. The evanescent coupling of the optical mode in the active region with the photonic crystal layer enables large area two dimensional in-plane lasing mode in the photonic crystal cavity due to bandedge effect. Bragg's multi-order diffraction provides the necessary feedback for the lasing and enhances surface normal laser emission. Such in-plane lasing mode can be scaled to hundreds of micrometers or even millimeters to achieve high power laser emission while maintain the single mode characteristics.

In this thesis, monolithic high power PCSEL is reported on GaAs substrate with Watt class high output power from a single 200 µm x 200 µm emitter at 1040 nm using InGaAs MQWs active region. Right angled isosceles triangular airholes square lattice photonic crystal is fabricated using reactive ion etching process. Metalorganic chemical vapor deposition assisted regrowth process has been employed to preserve airholes (voids) in the photonic crystal cavity for electrical fabrication process. COMSOL Multiphysics and S^4 based on rigorous coupled wave analysis software packages are explored to investigate the modal characteristics of triangular airholes photonic crystal structure.

Innovative indium bump flip-chip bonding process has been optimized to enable uniform charge injection into large PCSEL emitter and surface emission is collected from the backside through substrate. Thermal issues triggered due to high current operation are mitigated by taking advantage of flip-chip bonded Si with comparatively high thermal conductivity of 150 $Wm^{-1}K^{-1}$ better than that of GaAs 45 $Wm^{-1}K^{-1}$. The PCSEL/Si flip-chip bonding also demonstrates high yield 2D array (8x8 devices) scaling of PCSEL emitters with various PC lattice designs enabling beam steering on a single chip, coherent PCSEL array and lateral confinement PCSELs.

The measured spectral characteristics show a dominant mode with narrow full width half maximum of 0.05 nm and excellent side mode suppression ratio of greater than 40 dB is achieved. The L-I-V and spectral characteristics of the PCSEL device is measured in both pulsed operation and continuous wave (c.w.) operation. The experiment results are also correlated to theoretical and numerical analysis to understand the mode properties and lasing conditions.

The cavity scaling challenges on PCSELs while maintaining the single mode emission are also investigated. Innovative approach to estimate the maximum single mode emission size of the PCSEL is reported using quality factor and wave vector relationship. The gain-threshold discrimination between fundamental mode and higher order modes is calculated for various photonic crystal cavity designs and formulated the feasibility of scaling PCSELs to millimeters scale. The temporal changes in the photonic crystal cavity at higher current injection levels that trigger multi-mode emission are summarized and lateral heterostructure photonic crystal cavities are recommended for optical confinement to achieve single mode emission and compensate the electrically induced changes.

Table of Contents

List of Illustrations

List of Tables

Chapter 1

INTRODUCTION

1.1 Motivation

Lasers have a significant impact in our present world with multiple technologies associated to direct energy and sensing applications [1], [2]. High-power, high-intensity, narrow-divergence, highly directional laser sources have been instrumental in material processing, electronics processing, modern medical and surgical procedures, optical communications, entertainment industry and furthermore. Recently, Light Detection and Ranging (LiDAR) and 3D sensing applications in autonomous cars, factory autonomous robots and mobile phones have changed the course of technology and enabled smart society and smart processing [3]. This increased the demand for compact, portable and high-efficient single mode semiconductor lasers with excellent beam and spectral properties.

Several semiconductor laser architectures are continuously investigated to cater the needs of technology to achieve improved properties such as high frequency operation, narrow linewidth or high output power. Starting with edge-emitting lasers, that are configured to be the first-generation laser architecture, the light bounces between two parallel facets while confined in a ridge or gain-guided stripe. Overcoming the cavity losses with the gain provided by the active region, the amplified light is emitted as laser parallel to the plane of wafer's surface. By increasing the size of the cavity, high output power can be achieved, however with compromised asymmetric beam properties [4] as shown in Figure 1-1(a). Opto-mechanical components like cylindrical lens can be employed to correct the beam shape as shown in Figure 1-1(b) at the cost of reduced wall-plug efficiency. Such

complicated multi-component alignment structures provide challenges when mounted on moving objects like automobiles and 3D dynamic sensing packages.
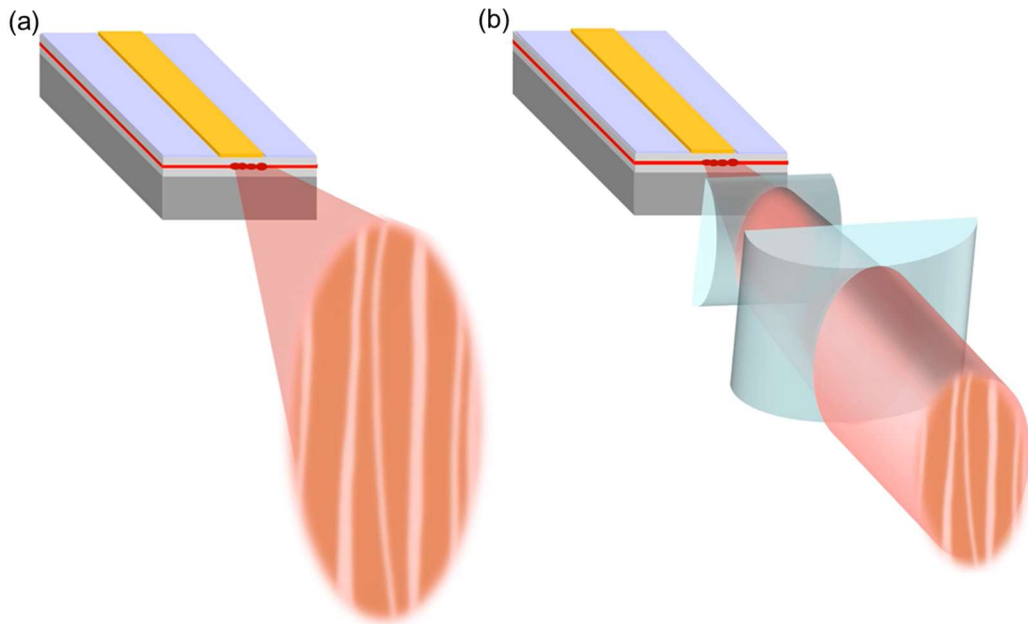
Figure 1-1 (a) Typical edge emitting laser architecture with asymmetric beam emitted from the edge of the facet; (b) edge emitting laser with multiple optical components to correct the beam shape [4].

Surface-emitting lasers (SEL) are advantageous for high power laser applications due to their unique properties of circular beams, the absence of catastrophic optical damage (COD), and their suitability for 2D integration for power scaling. Ideally, these lasers should be monolithic, electrically pumped (EP), with single mode emission and close to diffraction limited optical beam output. Both VCSELs (vertical-cavity surface-emitting lasers) and VECSELs (vertical external cavity surface-emitting lasers) have been investigated for high power laser applications with impressive power levels above 100 W achieved already[5]–[8].

VCSELs are monolithic with electrical injection and can achieve high beam quality with circular beam shapes as shown in Figure 1-2 and allow two dimensional (2D) arrays and on chip integration capabilities with complementary metal-oxide-semiconductor (CMOS) electronics. However, the emission area reduced to a few micrometers to enable single mode emission, limiting the output power to a few milli Watt levels [9]. Scaling of VCSEL emitter size triggers the competition from higher order transverse modes and critically degrades the beam quality (brightness) limiting the applications in communication, computing, and 3D sensing. The only way to achieve high power is by scaling the array of VCSELs instead of individual emitter sizes [7], [8], [10], [11]. In addition, high divergence angles of the emitted beam reduce the coupling efficiency when VCSELs are integrated with optical fibers or on-chip packages. Additional micro-lens system packages similar to the one showed in edge emitter case is employed to collimate the beam in VCSELs [10].
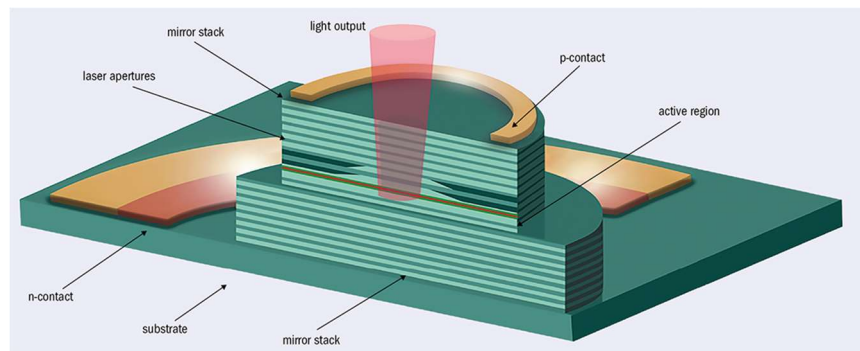
Figure 1-2 Schematic of the cross-sectional view of the vertical cavity surface emitting laser showing top and bottom DBR structures and beam emission [12].

On the other hand, while excellent beam quality and Watt class power can be obtained from VECSELs [13], the need of optical pumping and external mirror element limits its utility in practical high power laser systems. Additionally, the use of multi-layer distributed Bragg reflectors (DBRs) in these traditional VCSEL and VECSEL cavities not

3

only creates a major bottleneck in charge injection efficiency and thermal performance, but it also becomes technically challenging to realize DBRs at longer wavelengths.

Recently it has been discovered that high quality-factor (Q-factor) cavities can be achieved through the use of a single, defect-free photonic crystal (PC) which is evanescently coupled to a neighboring gain region [14]–[22]. In these devices, coined photonic crystal surface-emitting lasers (PCSELs), the lasing state corresponds to a single, high-Q point in the PC band structure, which exists above the light line. Since its initial proposal in 1999 by Noda *et al.* [20], electrically driven PCSELs have shown to achieve large area, coherent single-mode lasing with narrow beam divergence, and a single lobed beam [9], [23]–[27]. By adjusting the differential gain threshold through various PC lattice configurations, an output optical power greater than 7 W under continuous-wave (c.w.) conditions has been demonstrated by Noda et al. with an emission wavelength of 940 nm [9], [14], [23], [28]. Due to the excellent beam quality (M^2~1-2) a brightness of 320 MWcm^{-2} sr^{-1} has been achieved from a single mode single 800 μm sized emitter [29]. Recently, a 150 W single emitter PCSEL was reported [3]. PCSELs are also attractive as versatile, single-chip light sources with the capacity for control of the polarization, beam pattern and beam direction [30], [31]. With control of charge injection and lateral mode coupling, coherent PCSEL arrays can also be realized [32] for PCSEL power scaling on a chip. PCSELs have also been reported, in addition to regrowth processes, based on single growth with a deep etching process [33]. Heterogeneously integrated PCSELs at 1,550 nm with InP based MQWs on a silicon platform have also been reported based on a transfer printing technique [24], [34]–[37]. This provides roadmap for the III-V/Si photonic devices and co-packaging architectures while taking advantage of matured Si processing capabilities to enable high density heterogenous integration.

1.2 Overview of Dissertation

This dissertation is composed of complete PCSEL background theory, design considerations, simulation techniques, fabrication process, characterization and innovative approaches for future scaling of PCSELs.

Chapter 1 introduces the basic background and motivation for the requirement of high-power and high-brightness surface emitting lasers, merits and different strategic approaches realizing the electrically pumped PCSELs.

Chapter 2 begins with the physics involved in photonic crystal cavity and bandedge effect theory. It proceeds with the laser principle, epitaxial heterostructure design, selection of gain material, and maximizing extraction efficiency.

Chapter 3 presents different photonic crystal cavities including circular airhole, triangular airhole, Dirac-cone and double lattice designs, respective modal properties and gain-threshold estimation.

Chapter 4 details the fabrication process of circular airhole PCSEL including photonic crystal cavity patterning, Molecular beam epitaxy regrowth and double-ring epi-up fabrication process. Followed by series resistance optimization, electrode design optimization, and triangular airhole PCSEL fabrication process with metal organic chemical vapor deposition regrowth. In addition, the flip-chip bonding process for uniform charge injection is explained.

Chapter 5 presents the test set up built for characterizing the resonance modes, optically pumped resonance results of triangular airhole square lattice PCSEL before and after regrowth, lattice compensation for airhole refilling during regrowth, followed by electrical characterization in pulsed and c.w. operation. The watt class laser emitted power and spectral characteristics results are summarized and discussed.

Chapter 6 discusses the quality factor and wavevector relationship to estimate the maximum single mode emission size of PCSEL. It also includes the temporal changes in the PC cavity due to high density of carriers injected at high current operations such as spatial hole burning and photonic band gap. And provides theoretical solutions such as lateral heterostructure PC cavities to reduce these affects.

The concluding remarks and future research details are presented in Chapter 7.

Chapter 2

PHOTONIC CRYSTAL SURFACE EMITTING LASERS

2.1 Photonic Crystal Bandedge Effect

One of the strategic approaches to control the light-matter interaction is to create a periodic modulation of refractive index in the orders of optical wavelength, coined as *Photonic Crystal* (PC) cavities where the light may be tightly confined to form resonances with high quality Q factor [38]–[41]. In a two-dimensional (2D) PC, often referred as photonic crystal slab (PCS), the periodicity is maintained along the in-plane (x- and y-axis) and homogeneous along the vertical (z-axis) direction. A scan electron microscope (SEM) image of a photonic crystal cavity with circular airholes and square lattice is shown in Figure 2-1(a). Light propagates in-plane in this periodic refractive index contrast structure and undergoes multiple Bragg's diffraction.
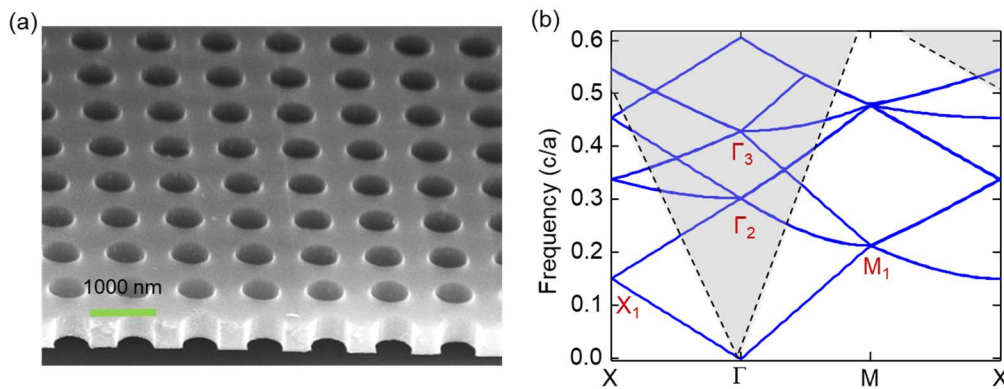
Figure 2-1 (a) Scan electron microscope (SEM) image of Si PC cavity with square lattice circular airholes; and (b) dispersion chart of a PC cavity showing different resonant bands. Note Γ points (Γ_2 and Γ_3) are located above the light line (grey region with dashed-line) offers the desirable surface normal lasing characteristics [42].

Similar to the energy levels in electronic band structure, the probable allowed photon energy levels in a PC cavity can be computed by solving Maxwell's equations [43] using Rigorous Coupled Wave Analysis (RCWA) or Finite Discrete Time Domain (FDTD) techniques. This results in photonic band structure as a function of wavevector k shown in Figure 2-1(b). The gradient of the photonic band structure results in zero at some locations resulting in a *Band Edge*. Multiple band edges can be identified in the photonic band structure exhibiting different sort of wave coupling depending on the Bragg conditions. Waves travel in different coupling directions at these points, resulting in a considerable rise in mode density [41]. These points are referred as X_1, M_1, Γ_2, and Γ_3 and points as shown in Figure 2-2(b).

(a)   (b)
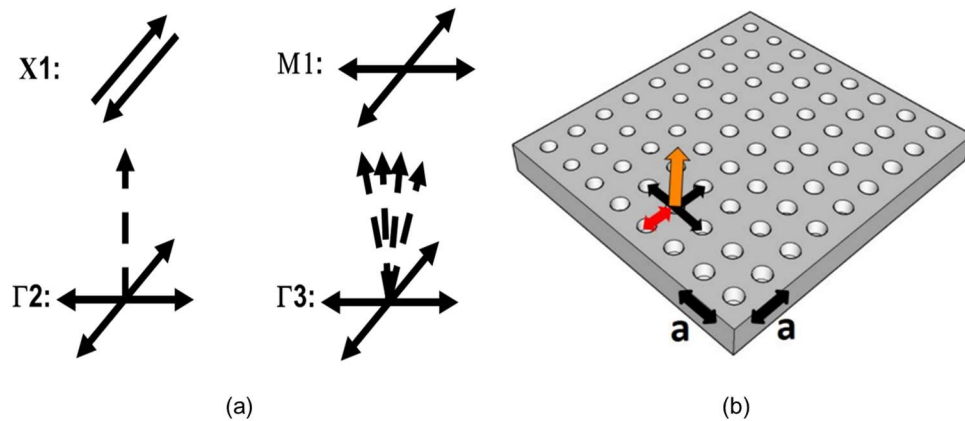
Figure 2-2 (a) Schematic of various band edge modes and their respetive couples waves propagating in different directions [21]; and (b) Schematic of the PC cavity showing the propagation of lightwaves based on Bragg's first order black and orange arrows (90° in-plane and 90° out of plane) and second order diffraction red arrow (180° in-plane) [44]

Any high Q band edge can result in lasing and properties such as mode stability, beam patterns and polarizations are dependent on the band edge. The group velocity at the photonic band edge is zero and the 2D Distributed Feed Back (DFB) effect gives rise to a standing wave [9]. With the right gain conditions maintained at the band-edge

resonance, it is possible to produce single-mode oscillation. These band edges induce both in-plan as well as diffraction in the direction normal to photonic crystal plane paving way to surface emissions. This expands the application of the 2D photonic crystals to high output power, single mode, and surface emitting lasing.

At X_1 point two lightwaves that are propagating in the opposite directions in the plane of PC surface couple to form a standing wave. As seen from Figure 2-2(a) this point is below the light-line, it is not leaky and does not correspond to surface emission. However, this provides the necessary feedback and high in-plane Q values to support edge lasing. Conventional distributed feedback (DFB) edge emitting lasers use the similar architecture to achieve lasing and narrow spectral characteristics. Another point M_1 is similar to X_1 point, but light couples in four equivalent directions to form a 2D standing wave in the plane of PC cavity and also a non-leaky mode. Unlike X_1 and M_1 points, Γ points have some interesting features. Lightwaves propagating in single direction undergo multiple diffractions including backward diffraction 180° due to Bragg's second order diffraction shown in red arrows in Figure 2-2(b) and diffraction in two other two equivalent +90° and -90° directions because of Bragg's first order diffraction shown in black arrows. These diffracted waves are again reflected back forming a large area 2D standing wave in the plane of PC. As both Γ points are located above the light-line, the modes become leaky and surface emission can be achieved. At Γ_2 point, due to first-order Bragg diffraction, light is diffracted in a direction normal to the photonic crystal plane (z-direction). As a result, surface normal lasing can be achieved. In addition to the surface normal emission, angular dependent surface emission is achieved at Γ_3 point which is instrumental in laser beam steering applications. Depending on the requirement, different Γ points are explored.

2.2 Laser Principle

In PCSEL, the light is vertically confined in the active layer with the help of cladding layers in the heterostructure and gets amplified as it propagates in-plane. When a two-dimensional (2D) square-lattice photonic crystal slab is placed close to the active layer, though the light is confined in the active region, the evanescent wave penetrates the PC layer as shown in Figure 2-3(a) and (b). If the pitch or lattice constant '*a*' of the square-lattice PC matches to the wavelength of the light propagating in the active layer, the evanescently coupled light from active layer will undergo multiple Bragg diffractions inside the PC layer as shown in Figure 2-2(b).

Considering a symmetric PC cavity with same lattice constant in both x- and y directions, that is equal one wavelength in the PC material, lightwaves propagate in the +y direction (0°), gets reflected backwards (180°) due to Bragg's second order diffraction. In addition, the PC geometry also satisfies Bragg's first order diffraction, the lightwaves get diffracted to the perpendicular directions (+90° and -90°) that are in turn again reflected backwards. As a result, lightwaves propagate in four directions and gets coupled to each other forming a large area 2D standing wave in the plane of the PC surface as shown in Figure 2-3(d) [21]. In addition, if the resonant bands are designed to match the peak gain of the active region at Γ_2 point, the in-plane 2D mode leaks out in surface normal direction (vertical z) as the first-order Bragg diffraction condition is satisfied, resulting in a vertically diffracted surface normal emission with high output power [9], [45].
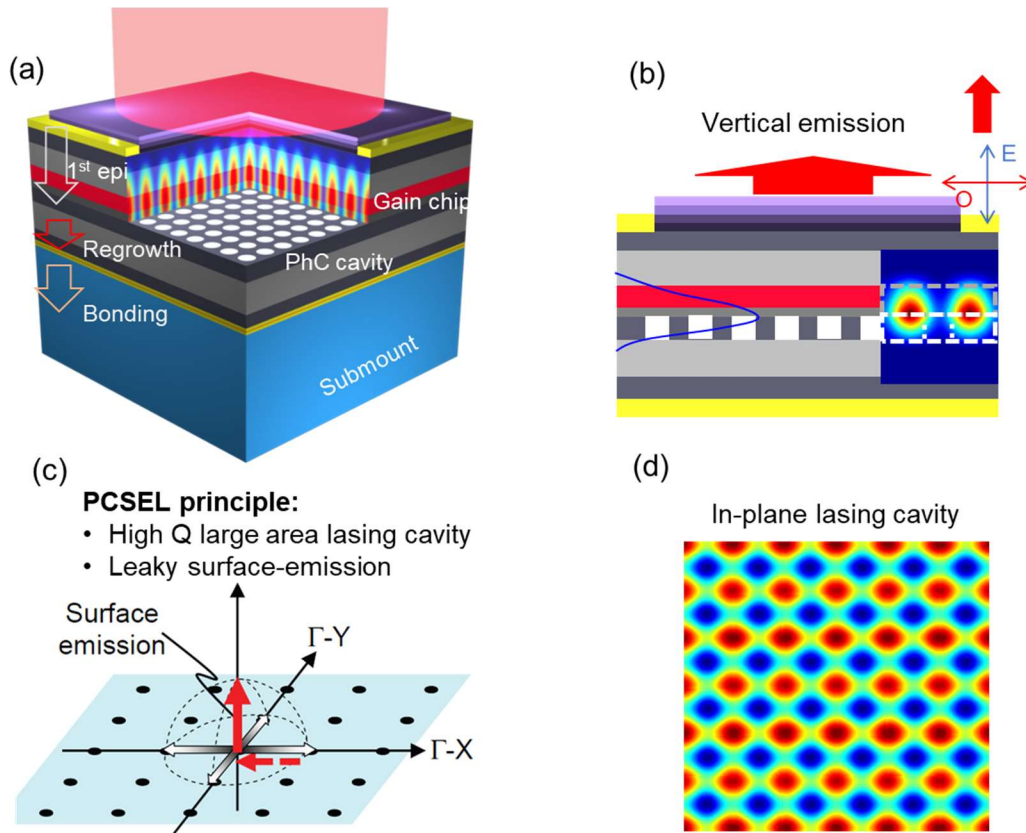
Figure 2-3 (a) PCSEL 3D schematic view, with simulated lasing mode overlap illustrating the evanescent coupling between gain layer and PC cavity laser; (b) Cross-sectional view showing vertical emission; (c) *k*-space representation; and (d) Simulated in- plane lasing mode [9].

2.3 Heterostructure Design Optimization

Heterostructure design plays a crucial role in optical confinement and uniform injection of the charge carriers into the active region. Unlike VCSELs where the optical mode is confined by DBR structures and provide required cavity feedback, in PCSELs, a photonic crystal cavity replaces the DBR structures to provide the necessary feedback and resonance for lasing. Therefore, to vertically confine the optical mode, the MQW active region is sandwiched with relatively low refractive index cladding layers, similar to edge emitter laser for vertical optical confinement approach. In addition, the PC cavity also provides lateral optical confinement when the PC sizes are larger than 50 µm and the emitter size can be scaled to hundreds of µm, or even mm scale while maintaining single mode emission, compared to single mode VCSELs with a few µm emitter sizes that employee mesa structures for lateral optical confinement.

2.3.1 980 nm InGaAs-AlGaAs MQW PCSEL Heterostructure

The initial 980 nm heterostructure design consists of three periods of InGaAs QWs and AlGaAs Barriers as active region. A 50 µm diameter finite 3D model with the PCSEL heterostructure is developed in COMSOL Multiphysics software based on finite-element analysis as shown in Figure 2-4(a). Electrical performance parameters of the PCSEL such as I-V characteristics, uniform carrier distribution in QWs, series resistance, doping concentration and carrier accumulation at interfaces and in the photonic crystal layer; and spontaneous emitted power per unit volume are simulated by using the physical models such as axial symmetry, continuous quasi-fermi level, optical transitions and auger recombination with high resolution non-uniform mesh as shown in Figure 2-4(b).
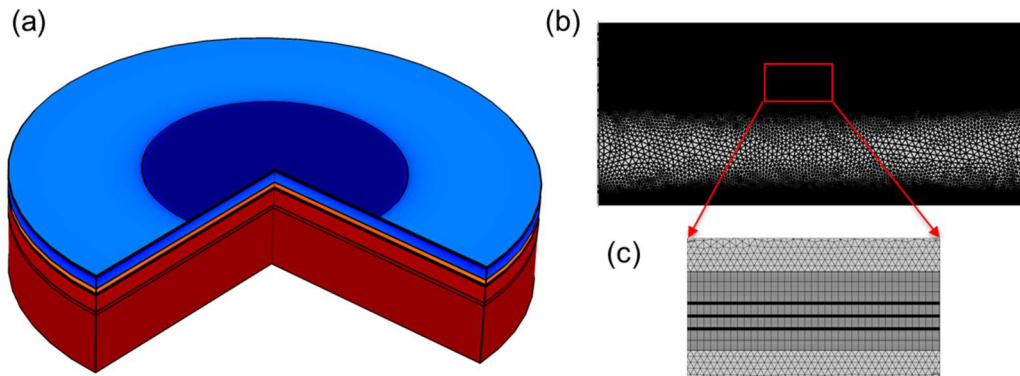
Figure 2-4 (a) 50 µm diameter finite 3D PCSEL model developed in COMSOL Multiphysics software; (b) non-uniform meshing in various layers of the PCSEL heterostructure; and (c) finite meshing in MQW layers

As shown in Figure 2-5(a), the simulated I-V characteristics are low because of high series resistance caused due to carrier accumulation in PC layer. This increases the series resistance and carriers in the PC cavity, that in turn increases the absorption losses, as a result the gain-threshold for lasing mode would also increase. In addition, the carrier accumulation is also observed at AlGaAs-GaAs cladding layer interfaces due to sudden change in the material properties as shown in Figure 2-5(c). Band bending is also observed at high current injection of 5 kA/cm^2 and non-uniform carrier distribution among three QWs as shown in Figure 2-5(b) and (d). This is because the barrier height is very high that limited the electron flow to adjacent QWs. As a result, the radiative recombination is also non-uniform and occur at single well instead of three wells as observed in Figure 2-5(d).
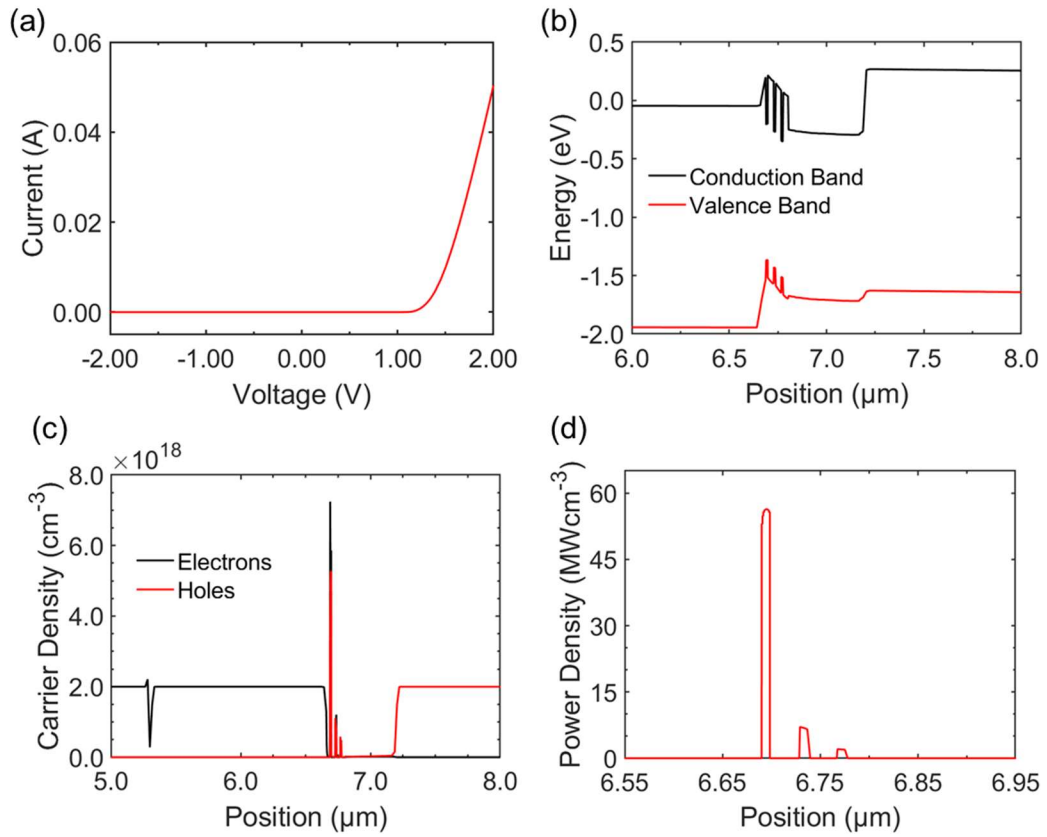
Figure 2-5 Simulated electrical characteristics for 980 nm InGaAs-AlGaAs heterostructure using COMSOL model: (a) I-V characteristics; (b) band diagram at 5 kA/cm^2 current density; (c) carrier concentration at 5 kA/cm^2 at different layers; and (d) Spontaneous emitted power per unit volume.

2.3.2 980 nm InGaAs-GaAs MQW PCSEL Heterostructure

To solve these above issues, the heterostructure is optimized with reduced barrier height by replacing AlGaAs barriers with GaAs barriers in the initial 980 nm heterostructure design. To avoid the flow of electrons into the PC layer AlGaAs electron blocking layer is introduced between the active region and PC layer. This high bandgap material traps or blocks the electrons that roll over into the PC layer at higher current injection levels and helps in minimizing carrier induced cavity losses. In addition, step index layers are added at AlGaAs-GaAs layer interfaces to reduce the carrier accumulation at the interfaces. The p+ GaAs layer thickness is also optimized to enhance lateral charge diffusion and to provide phase matched condition to reflect the downward reflected PCSEL emission.

This resulted in improved I-V characteristics, band alignment, uniform carrier distribution and uniform spontaneous emitted power per unit volume in three QWs as shown in Figure 2-6. The band bending at high current injection that was observed in AlGaAs barrier design is not observed in GaAs barriers. There is a clear uniform distribution of carrier among all the QWs. The carrier accumulation in photonic crystal layer is reduced with the help of AlGaAs e-blocking layer. However, the accumulation of carriers is still observed at the AlGaAs-GaAs clad-contact interface. This shows that the step index employed at the AlGaAs-GaAs interface to reduce the carrier accumulation did not solve the problem. Further improvement to the heterostructure is carried out and explained in detail in section 2.3.3.
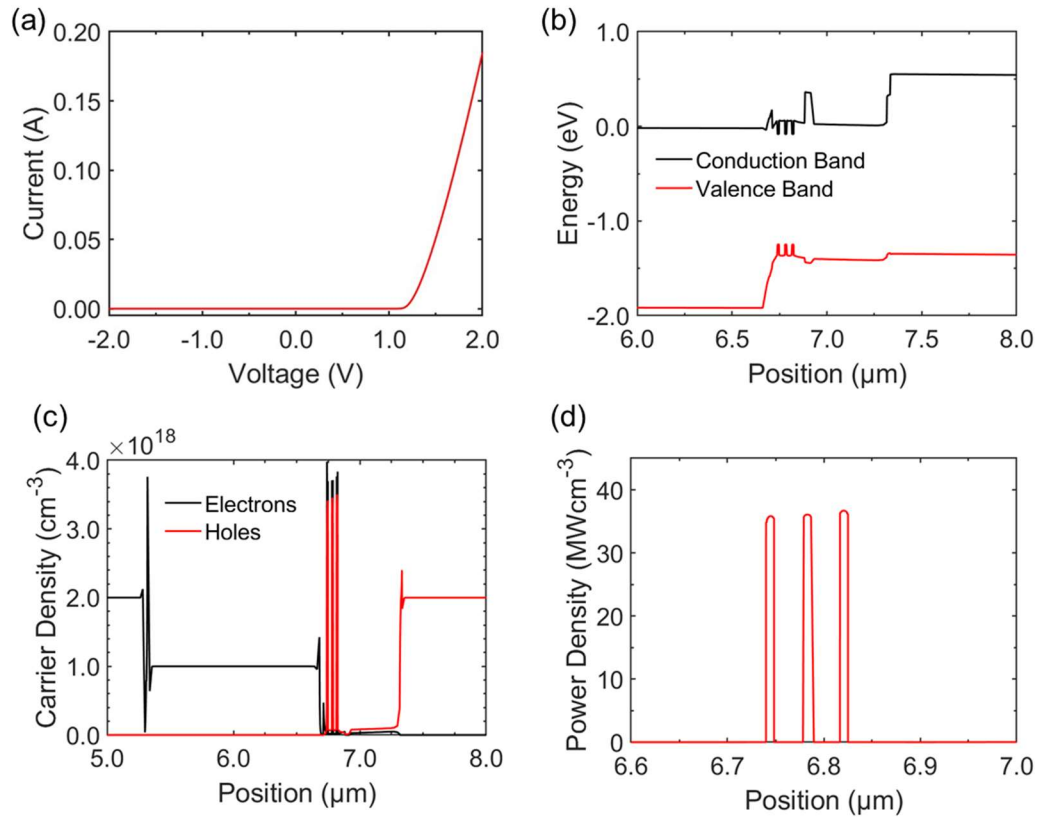
Figure 2-6 Simulated electrical characteristics for optimized 980 nm InGaAs-GaAs heterostructure design using COMSOL model: (a) I-V characteristics; (b) band diagram at 5 kA/cm^2 current density; (c) carrier concentration at different layers; and (d) Spontaneous emitted power per unit volume.

2.3.3 1040 nm InGaAs-GaAs MQW PCSEL Graded Heterostructure

The AlGaAs e-blocking layer introduced between active region and PC layer has reduced the density of electrons flowing into the PC layer and improved the I-V characteristics. However, the step index at the AlGaAs-GaAs cladding interfaces did not solve the carrier accumulation problem. Therefore, the step index is changed to linearly graded AlGaAs index at the AlGaAs-GaAs cladding interface. The Aluminum composition in interface layers is linearly changed from 0% to 38% to achieve graded refractive index. Similarly, the doping concentration is also graded in the cladding layer solve these issues.

Uniform charge injection is critical for high power and high beam quality PCSEL emission. The COMSOL Multiphysics simulations carried out to evaluate the electrode design, lateral carrier diffusion limitations, series resistance, doping concentration and carrier accumulation at interfaces and the photonic crystal layer indicates improved overall PCSEL electrical performance such as I-V characteristics, uniform carrier distribution in QWs and spontaneous emitted power per unit volume.

Shown in Figure 2-7(a) are the I-V characteristics for a 1040 nm InGaAs-GaAs MQW 50 µm PCSEL heterostructure with graded AlGaAs layers. PC is modelled as lattice matching GaAs layer with effective refractive index based on the geometry of the PC layer. The series resistance extracted from the I-V data is 3.26Ω. The heterostructure band diagram simulated at 5 kA/cm^2 (which is around 10 times above threshold current density) indicates no band bending as shown in Figure 2-7(b). In addition, there is no accumulation of charge carriers at various layers or interfaces as observed from Figure 2-7(c) and uniform recombination is observed among all the three QWs as seen in Figure 2-7(d).
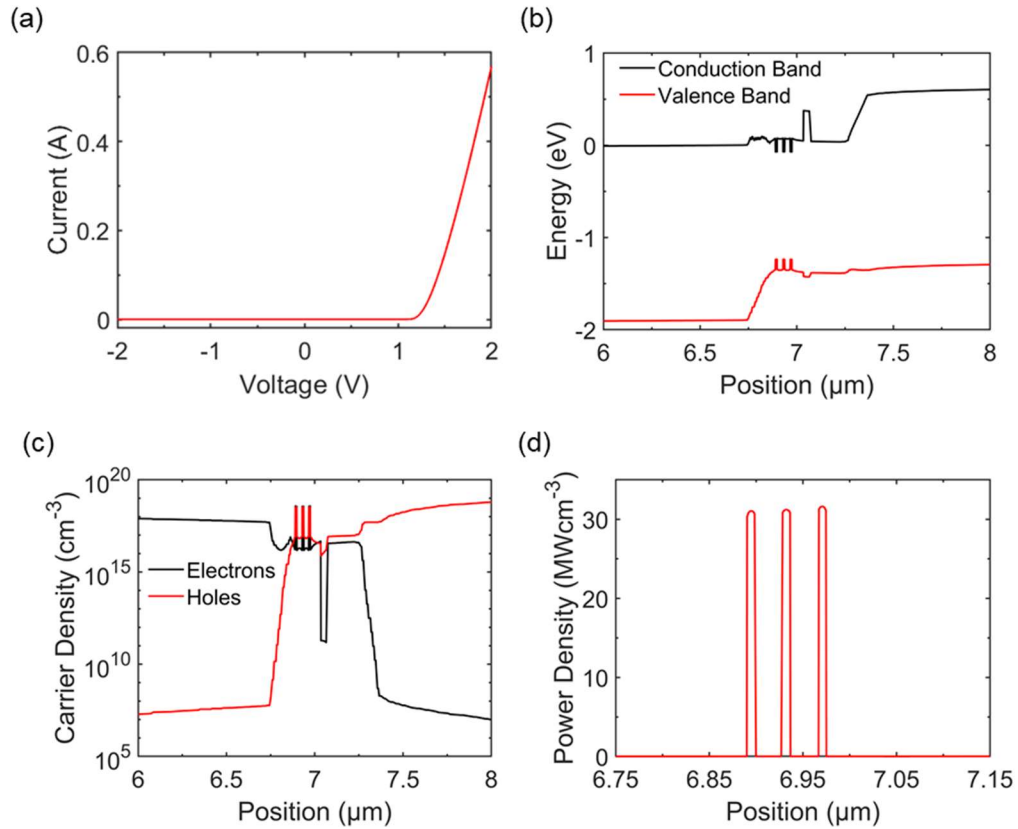
Figure 2-7 Simulated electrical characteristics for AlGaAs graded heterostructure using COMSOL model: (a) I-V characteristics; (b) band diagram at 5 kA/cm² current density indicating no charge built-up at interfaces; (c) carrier concentration at 5 kA/cm² at different layers indicating uniform charge distributions within 3 QW layers; and (d) Spontaneous emitted power per unit volume.

The electrical characteristics simulated for different heterostructure designs using COMSOL Multiphysics software are summarized in Figure 2-8. The graded Aluminum composition at the GaAs-AlGaAs clad-contact interface has completely reduced the carrier accumulation at the interfaces. All the carriers are directed to active region without accumulation at the layer interfaces or in the photonic crystal layers. I-V characteristics are

slightly improved and the spontaneous emitted power per unit volume in QWs is uniform among the three wells as shown in Figure 2-8(a). The series resistance extracted from the I-V characteristics of different heterostructures designs as shown in Figure 2-8(b) results in reduced values indicating the optimization of heterostructure for electrical performance of PCSEL.
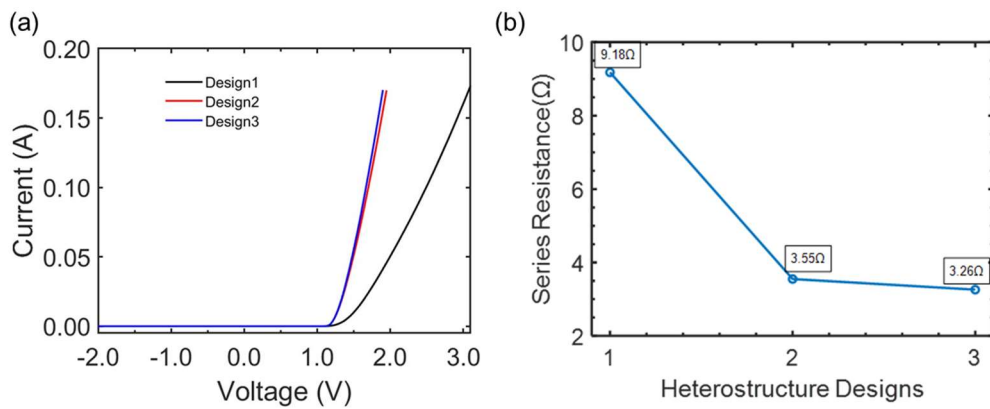
Figure 2-8 Comparison of (a) I-V characteristics of different heterostructure designs; and (b) series reistance for different heterostructures designs simulated using COMSOL Multiphysics software. Note, Design 1: initial 980 nm epitaxial heterostructure; Design 2: 980 nm epitaxial heterostructure with e-blocking layer and step-index at interfaces; and Design 3: optimized final 1040 nm heterostructure with AlGaAs graded layers for improved carrier distribution into MQW active region.

2.4 Gain Medium: InGaAs Multiple Quantum Wells

The target PCSEL emission wavelength is 1040 nm that has less atmospheric attenuation for LiDAR and 3D optical sensing applications compared to other wavelengths. Strain compensated 3-period 8.35 nm $In_{0.25}Ga_{0.75}As$/ 30 nm GaAs MQWs are used as the gain medium. To simulate the material gain properties of these InGaAs/GaAs MQW active region, RSoft LaserMOD package is used, and gain spectra are simulated near the 1040 nm wavelength range at different temperature and charge density conditions as shown in Figure 2-9(a) and (b). The corresponding wavelength shift in the peak material gain is also reviewed to design the photonic crystal cavity lattice parameters to match the resonant modes with the gain peak. It is observed that there is a 20 nm red shift and peak value reduced from 2140 cm^{-1} to 1650 cm^{-1} as the ambient temperature is changed from 300 K to 350 K. On the other hand, the peak gain value increased to 4000 cm^{-1} as the carrier density is increased to 4 x 10^{12} cm^{-2} as observed in Figure 2-9(b).
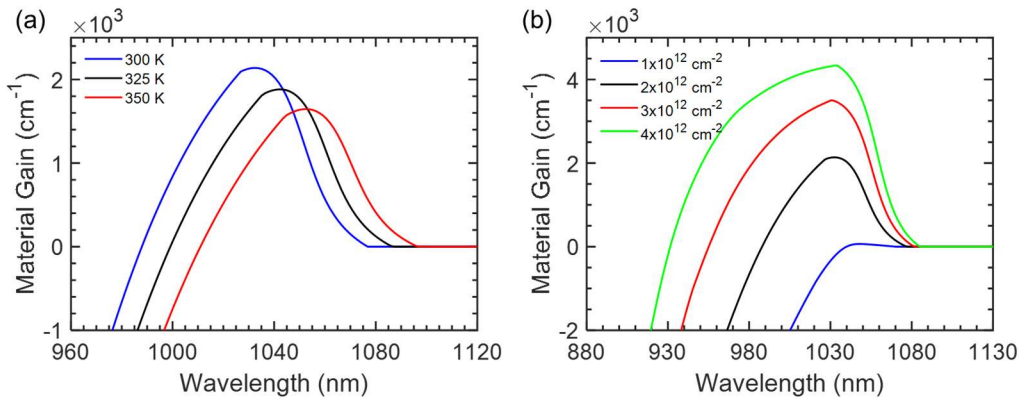
Figure 2-9 Gain spectra simulated using RSoft LaserMOD simulation package (a) at different ambient temperature to evaluate the shift in gain spectra at higher temperatures; (b) at different carrier densities to estimate the peak material gain

2.5 Optimization for Maximum Extraction Efficiency

Another consideration to maximize the output power is the optimal optical design of extraction efficiency. The surface normal PCSEL output radiation forms laser beam in both the upward and downward directions. The downward emitted power can contribute to the laser output power by using the bottom reflector structures such as p-metal or DBRs. In the fabrication step, the thickness of the p-GaAs contact layer is tuned to the constructive interference conditions and a higher extraction efficiency can be achieved.

The goal is to achieve maximum extraction efficiency by reflecting the downward power in the upward direction as shown in Figure 2-11(a). The p-contact metal deposited on the p+ GaAs layer acts as a partial reflector for the epi-down PCSEL design where the laser is emitted from the GaAs substrate. However, if the thickness of the p+ GaAs is not properly optimized there could be phase mismatch between upward and downward reflected power that leads to poor or no emission from the laser cavity.

(a)   (b)   (c)
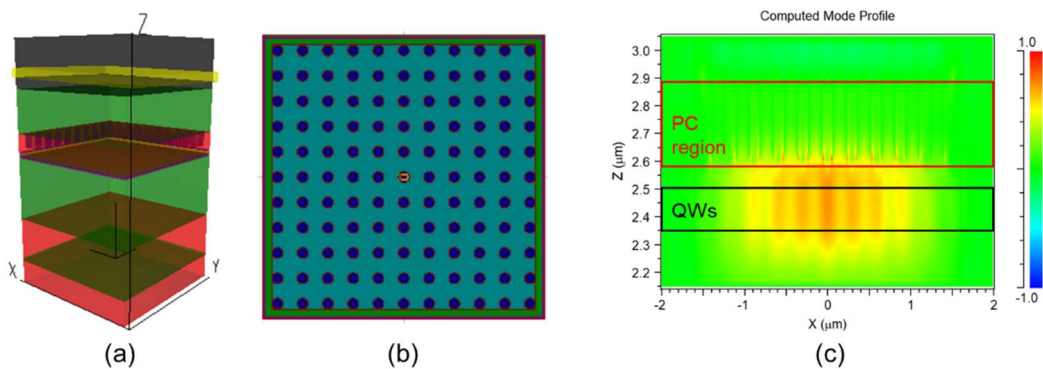
Figure 2-10 (a) Schematic of the 3D finite PCSEL model developed in the RSoft FullWAVE simulation package; (b) top-view showing PC lattice design with circular airholes square lattice; and (c) simulation of the optical mode confined in the QWs regions.

To optimize the thickness of p+ GaAs and to achieve maximum extraction efficiency, a finite sized 3D PCSEL model is developed in RSoft FullWAVE package. This model contains 10 periods of airholes in the GaAs layer as photonic crystal cavity as shown in Figure 2-10(a) and (b). The overall device size is 4 μm x 4 μm x 4 μm. Au metal is placed below the p+ GaAs layer as reflector and p-ohmic contact.

The QWs active region is modelled as a plane wave source with a peak wavelength of 1.040 μm emitting in upward (towards substrate) and downward (towards p+ GaAs layer) directions simultaneously. Figure 2-10(c) shows the optical mode confined in the QWs region. A detector is placed above the substrate to monitor the emission field intensity. The field propagating downward gets reflected by the Au metal pad. When both upward and downward reflected fields are propagating, maximum and minimum transmission is observed at in the detector as shown in Figure 2-11(b). The phase condition of the fields is controlled by varying the p+ GaAs thickness. As observed in Figure 2-11(c), maximum extraction efficiency is obtained when the thickness of the p+ GaAs layer is 144 nm due to constructive interference of upward and downward propagating emission or the phase match condition. Similarly, at 235 nm thick p+ GaAs layer, the upward and downward emissions are interfering destructively causing very less or no emission in the upward surface normal direction as shown in Figure 2-11(d).
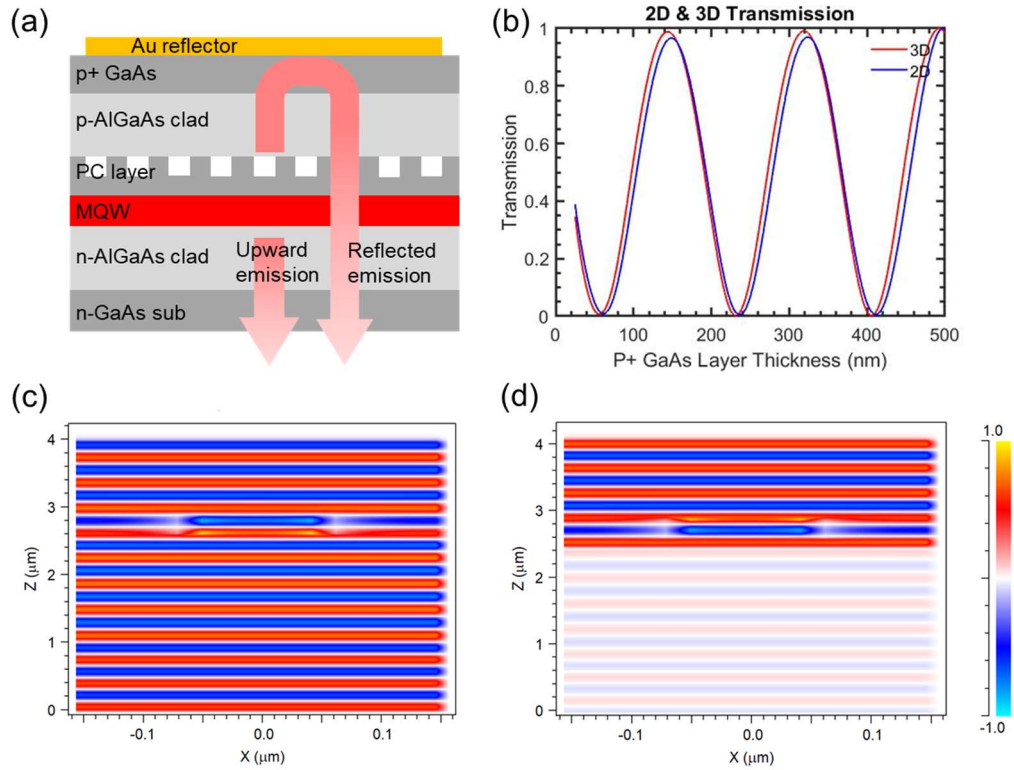
Figure 2-11 (a) Schematic of the PCSEL showing the upward and reflected emissions caused due to Au reflector; (b) transmission profile of the upward and downward combined emission at various p+ GaAs layer thickness; (c) phase matched constructive interference between upward and downward reflected emission at 144 nm p+ GaAs thickness; and (d) destructive interference between upward and downward reflected emission at 235 nm p+ GaAs thickness

Chapter 3

PHOTONIC CRYSTAL CAVITY DESIGNS

In principle, any sufficiently high-Q resonance can be chosen for the lasing mode, since one can always adjust the feature size of the PC to place the frequency of such resonance at the center of the gain spectrum. However, in practice, there are substantial benefits for choosing a lasing state corresponding to a resonance with zero group velocity in the plane of the PC slab, as such modes will not readily radiate out of the edges of the device [21], [46], [47]. Most previous PCSEL designs have focused on lasing at the momentum (k) space Γ (k = 0) point, where the desired photonic crystal band exhibits a critical point [9]. This mode at the Γ (k = 0) point is intrinsically leaky (as it is located above the light-line) with emission perpendicular to the in-plane direction. Previous studies have demonstrated lasing at other high-symmetry points in the Brillouin zone, which allows for a measure of beam steering of the output emission [48].

3.1 Circular Airhole PCSEL Cavity Design

The lasing characteristics of the PCSEL are mainly dependent on the geometry of the PC slab. By changing lattice constant a, the frequency of the lasing mode can be optimized to match the active region gain peak that helps in reducing the gain threshold. Uniformity of the airhole shape is required to reduce the in-plane scattering losses in the PC slab. Initially a circular airhole square lattice PC cavity is designed with lattice constant a=292 nm and radius of the airhole r=66 nm shown in Figure 3-1(a) to achieve resonance at 980 nm to match the gain of $In_{0.18}Ga_{0.82}As$ MQW / $Al_{0.25}Ga_{0.75}As$ barrier active region. The corresponding photonic band diagram is shown in Figure 3-1(b).
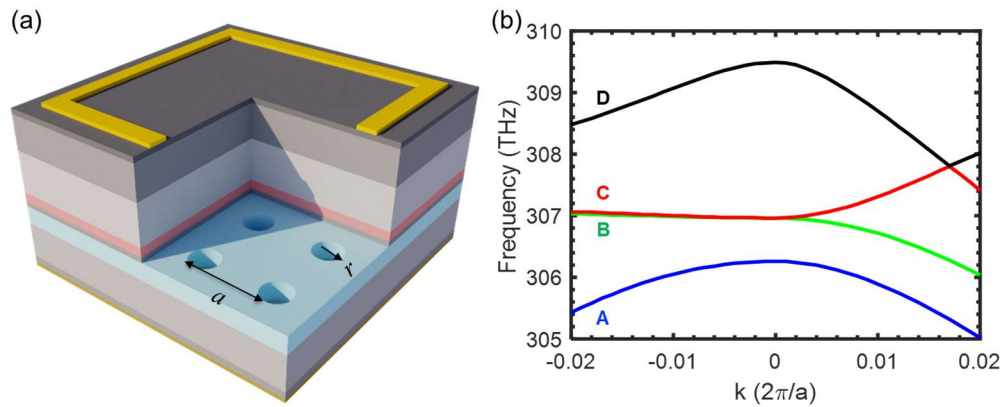
Figure 3-1 (a) Schematic of the circular airhole square lattice PCSEL design with '*a*' lattice constant and '*r*' radius of the circular airhole; (b) dispersion chart showing different resonant bands simulated using COMSOL Multiphysics software.

3.1.1 Cavity Resonance Modes in Circular Airhole PCSEL

As shown in Figure 3-1(b) dispersion plot, four resonant modes are observed at the frequency range close to 307 THz that correspond to 980 nm wavelengths for the PC cavity with the lattice constant *a*=292 nm, radius of the airhole *r*=66 nm and PC thickness, *t*= 293 nm. These four modes are transverse-electric (TE) modes computed by solving the electric field distribution within the PC surface plane. Each mode has different *Q* value, E-field distribution over MQW region and eventually different confinement factors that influence the gain-threshold condition and performance of the PCSEL.

3.1.2 Modal Characteristics in Circular Airhole PCSEL

Figure 3-2 shows the amplitude of the magnetic field (H_z component) distribution around the airhole in a unit cell for four resonant modes in the direction perpendicular to the PC plane. To evaluate the lasing mode and estimate the gain threshold condition, the electric field distribution in at different z values perpendicular to the PC surface plane is simulated for all the modes and shown in Figure 3-3.

Figure 3-2 Magnitude of the in-plane H_z component of the four resonant modes in circular airhole PC cavity (a) mode A; (b) mode B; (c) mode C; and (d) mode D.

Figure 3-3 Magnitude of the E_y component of the four resonant modes in circular airhole PC cavity showing the optical confinement in the MQW active region (a) mode A; (b) mode B; (c) mode C; and (d) mode D. Note, PC: photonic crystal layer and MQW: multiple quantum well layer.

3.1.3 Coupling Efficiency and Gain Threshold Estimation

The lasing mode forms as the in-plane guided mode in the PC cavity layer, and evanescently couples with the neighboring active gain layer containing multiple quantum wells (MQWs). To define the overlaps of the lasing mode with the MQWs and PC layers, we define the confinement factors with the following equations:

$$\Gamma_{QW} = \frac{\int_{QW} \varepsilon |E|^2 \cdot dv}{\int_{cavity} \varepsilon |E|^2 \cdot dv} \tag{3.1}$$

$$\Gamma_{PC} = \frac{\int_{PC} \varepsilon |E|^2 \cdot dv}{\int_{cavity} \varepsilon |E|^2 \cdot dv} \tag{3.2}$$

The radiation loss α for the cavity can be related to the cavity quality factor Q, with the following equation:

$$\alpha = \frac{2\pi}{Q \cdot a} \tag{3.3}$$

where a is the lattice constant, and the quality factor Q can be derived from the Fano fitting of the resonances obtained in the reflection spectra [49]. Therefore, the gain threshold can be derived as follows:

$$g_{th} = \frac{\alpha}{\Gamma_{QW}} \tag{3.4}$$

Additionally, the increment in the size of airhole reduces the vertical Q-factor which in turn increases the gain threshold. However, a very high Q reduces the gain threshold, but decreases the emitted output power. Therefore, vertical Q-factor is optimized (typically in the order of 10^4) with trade-off between output power and gain threshold.

3.1.4 Gain Threshold Estimation in Circular Airhole PCSEL

Based on these fundamental equations, the confinement factor, quality factor and radiation loss, the corresponding gain threshold values for each mode are calculated as shown in the Table 3-2.

Table 3-1 Modal characteristics of four resonant modes in circular airhole PCSEL cavity at 980 nm

Mode	λ (nm)	Q	α (cm^{-1})	Γ_{QW} (%)	g_{th} (cm^{-1})
A	981.49	2.84×10^6	0.07	4.72	1.61
B	979.08	8.32×10^5	2.58	4.01	64.52
C	979.07	8.28×10^5	2.59	4.01	64.52
D	972.22	1.48×10^6	0.14	4.52	3.10

In the circular airhole PC cavity, a symmetric in-plane electromagnetic field is generated due to the symmetric airhole shape as shown in Figure 3-2(a). This causes destructive interference between the opposite travelling waves for normal emission in the PC, leading to reduced or no emission in the surface normal direction. This is referred as dark mode or non-leaky mode even though the mode is located at Γ_2 point. This is clearly observed in Table 3-1, mode A has the lowest gain threshold value of 1.61 cm^{-1}, making it to be lasing mode. However, due to high Q value in the order of 10^6, the in-plane mode does not couple out due to destructive interference of vertically diffracted lightwaves, resulting in reduced radiation constant. In practice, the circular airholes are not ideally symmetric due to the limitations in the fabrication process. As a result, emission can be achieved, but the output power in the surface normal direction may not be significantly enhanced.

3.2 Triangular Airhole PCSEL Cavity Design

Unlike the symmetric circular airhole shape, triangular airhole shape results in the asymmetric in-plane electromagnetic field and enables the constructive interference of vertical diffraction of the PC mode. That enhances the surface emission in the normal direction of PC slab and results in high output power in triangular airhole PC cavities compared to that of circular airholes.

A right angled isosceles triangular airhole square lattice PC is designed with lattice constant a=309 nm and side length of the airhole s=272 nm as shown in Figure 3-4(a) to achieve resonance at 1040 nm. The corresponding photonic band diagram is shown in Figure 3-4(b).

(a)   (b)
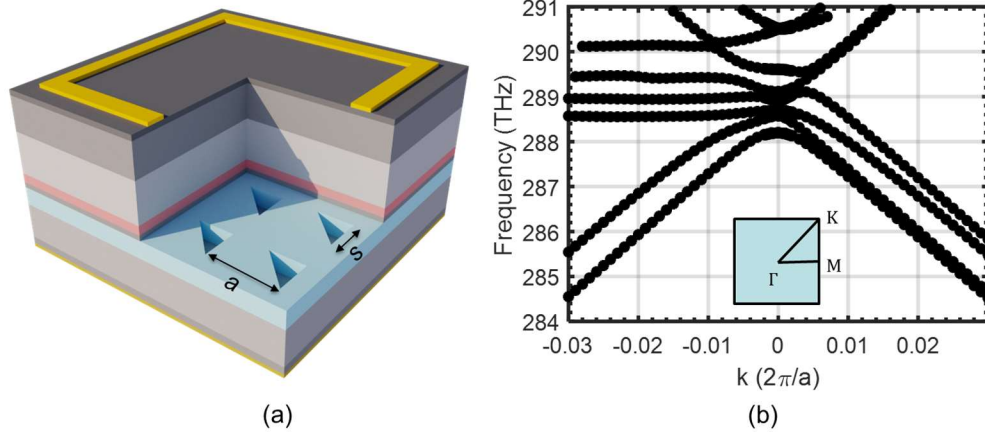
Figure 3-4 (a) Schematic of the triangular airhole square lattice PCSEL design with '*a*' lattice constant and '*s*' side length of the right-angled isosceles triangle; (b) dispersion chart showing different resonant bands simulated using COMSOL Multiphysics software.

3.2.1 Cavity Resonance Modes in Triangular Airhole PCSEL

As shown in Figure 3-5 dispersion plot, four resonant modes are observed at the frequency range close to 288 THz that corresponds to 1040 nm wavelengths for the PC cavity with the lattice constant, a=309 nm, triangle side length, s=273 nm and PC thickness,

t= 285 nm. These four modes are transverse-electric (TE) modes computed by solving the electric field distribution within the PC surface plane. Each mode has different Q value, E-field distribution over MQW region and eventually different confinement factors that influence the gain-threshold condition and performance of the PCSEL.
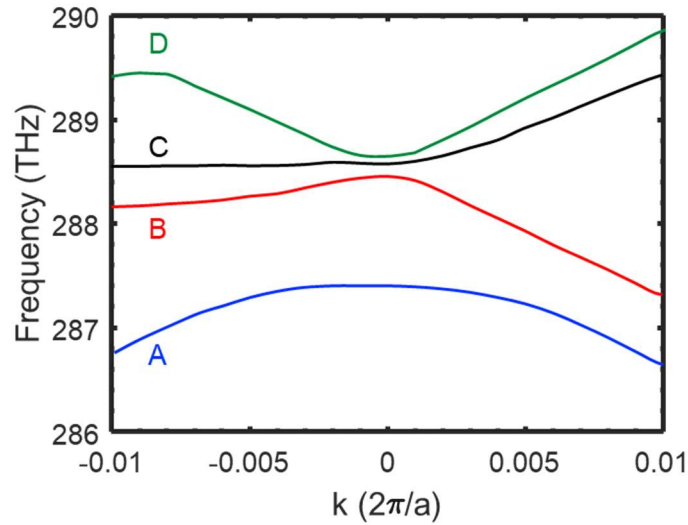
Figure 3-5 Resonant bands near k=0 (Γ_2 point) of triangular airhole PC cavity. The TE-like modes near the frequency of the gain spectra are named as A, B, C and D.

3.2.2 Modal Characteristics in Triangular Airhole PCSEL

Figure 3-6 shows the amplitude of the magnetic field (H_z component) distribution around the airhole in a unit cell for four resonant modes in the direction perpendicular to the PC plane. To evaluate the lasing mode and estimate the gain threshold condition, the electric field distribution in at different z values perpendicular to the PC surface plane is simulated for all the modes and shown in Figure 3-7.

(a) (b) (c) (d)
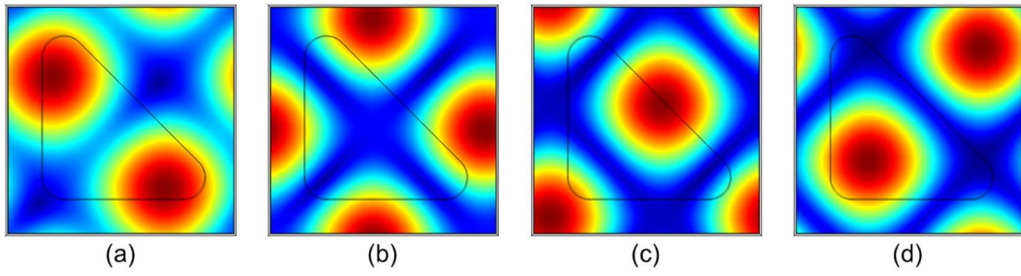
Figure 3-6 Magnitude of the in-plane H_z component of the four resonant modes in triangular airhole PC cavity (a) mode A; (b) mode B; (c) mode C; and (d) mode D.

PC layer

MQW layer

Z
X

(a) (b) (c) (d)
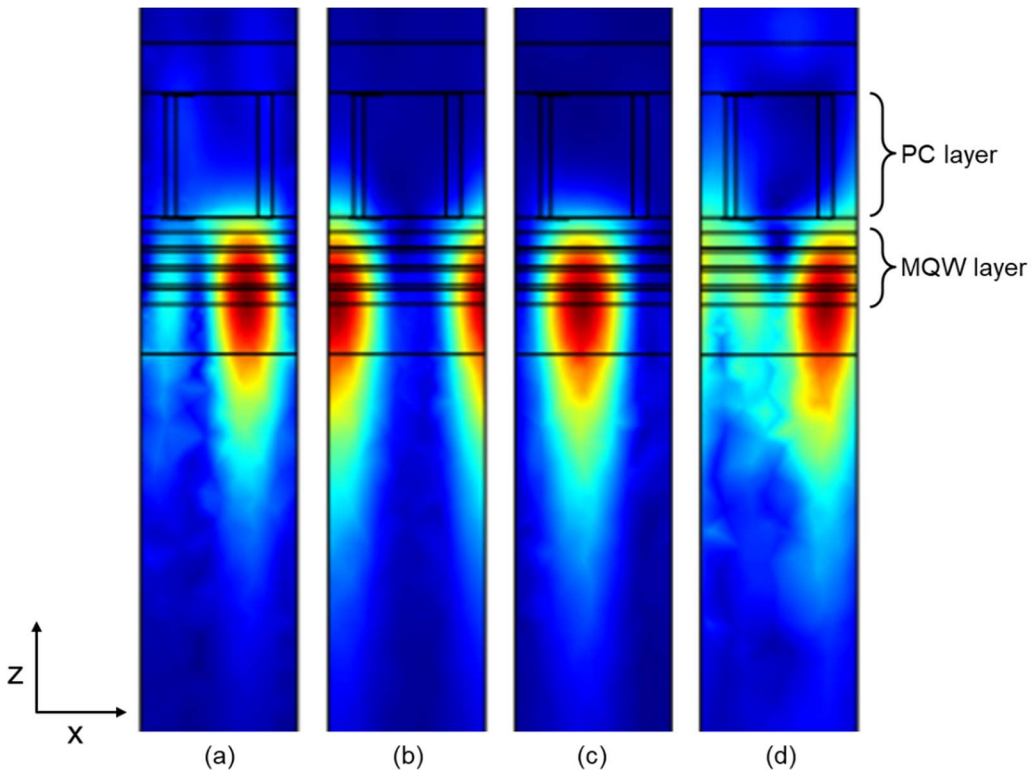
Figure 3-7 Magnitude of the E_y component of the four resonant modes in the plane vertical to the PC surface showing the optical confinement in the MQW active region (a) mode A; (b) mode B; (c) mode C; and (d) mode D.

3.2.3 Gain Threshold Estimation in Triangular Airhole PCSEL

With reference to the equations described in section 3.1.3, the confinement factor, quality factor, radiation loss, and the corresponding gain threshold values for each mode are computed in the Table 3-2.

Table 3-2 Modal characteristics of four resonant modes in triangular airhole PCSEL cavity at 1040 nm

Mode	λ (nm)	Q	α (cm^{-1})	Γ_{QW} (%)	g_{th} (cm^{-1})
A	1043.74	4.20×10^4	4.81	6.10	78.88
B	1040.00	8.34×10^4	2.41	6.42	37.51
C	1039.55	9.33×10^3	21.65	6.20	349.25
D	1039.31	2.86×10^3	70.76	5.58	1268.17

Based on the above gain-threshold simulations, mode B with lowest gain threshold value of 37.51 cm^{-1} would lase first. However, at high current injection levels, gain will be increased as shown in Figure 2-9 and mode A would also lase as it has the next lowest gain-threshold value of 78.88 cm^{-1}. The PC geometry should be optimized to increase the gain-threshold difference between the different bands of Γ_2 point located near the frequency of peak gain. Some of such PC geometries include circular airhole Dirac-cone and double lattice composite cavities as explained in the later sections.

3.3 Dirac-cone PCSEL Cavity Design

In a photonic crystal slab, a Dirac-cone can be formed by creating degeneracy at the Γ-point between a pair of two-fold degenerate dipole states and a singly degenerate state. Strong mixing of these linear photonic bands leads to Dirac-cone band structure. The quality-factor (Q-factor) of these bands has a distinct feature, *i.e.* two of the modes in the three bands have a low-Q values in the order of 10^3 which are of dipole nature, except for one mode at the Γ-point, which has an infinite Q-factor which is of quadruple nature. Theoretically, such a quadruple band structure is not suitable for lasers since the infinite high-Q mode will not emit output power. However, due to imperfections in the PCSEL fabrication process, the infinite-Q factor of the quadruple mode turns to a finite high-Q factor in the order of 10^5, which is an ideal value for lasing and also high output power emission. The other two modes with low-Q will have a very high threshold compared to the quadruple mode (more than 3 times). The lasing of other modes would happen at an extremely high current injection densities of 20 kA/cm^2 making the laser to be single mode (single-band) emission for wider range of current injection. In addition, the Q-factor as a function of wave vector k is a very narrowly peaked function, i.e. as we move away from Γ-point, Q decreases quickly. This is termed as degenerate width and an attractive result for pure single-mode operation as it determines the maximum single emission device of a PCSEL, explained in detailed in chapter 6.

Figure shows the schematic of the large circular airhole PC cavity to achieve Dirac-cone behavior in the photonic band structure at the frequency that matches the peak wavelength of the MQWs gain. The lattice parameters are tuned to a=313 nm, radius of airhole r=115 nm. The thickness of the PC layer t = 285 nm and the gain-threshold of the PCSEL lasing mode can be optimized by changing the thickness of the PC layer.
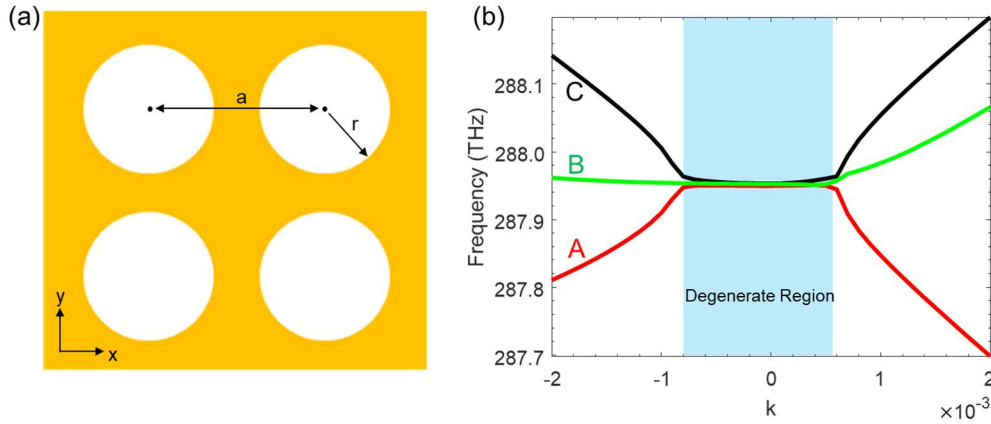
Figure 3-8 (a) schematic of the circular airhole Dirac-cone PC cavity top view. Note *a* is the lattice constant and *r* is the radius of airhole; and (b) Mixing of degenerate resonant bands near k=0 (Γ_2 point) forming the Dirac-cone photonic band structure, the modes are named as A, B and C.

3.3.1 Cavity Resonance Modes in Dirac-cone PCSEL

The three resonant modes named as A, B and C are observed at the frequency range close to 288 THz that corresponds to 1040 nm wavelengths for the PC cavity with the lattice constant a=313 nm, radius of the airhole r=115 nm and PC thickness t= 285 nm as shown in the **Error! Reference source not found.**. The width of the degenerate region on the k-space determines the maximum single mode emission These three modes are designed to be transverse-electric (TE) modes.

The corresponding Q-k relationship of these three modes simulated using COMSOL Multiphysics software is shown in Figure 3-9. As explained earlier, mode C is the quadruple nature mode with high Q value of 6×10^5 and the remaining two dipole nature modes A and B have Q values in the order of 10^3. The E-field distribution of these three modes over MQW region and the confinement factors are summarized.
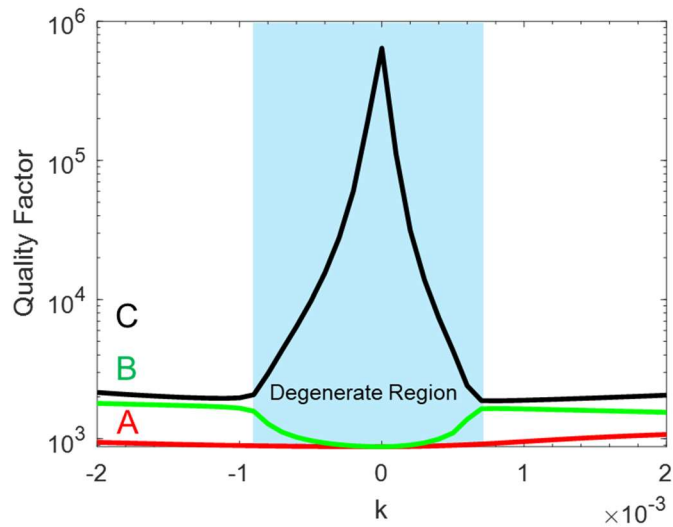
Figure 3-9 Q-k relationship of the three degenerate modes near the Γ point (k=0), Note: the modes are named as A, B and C

3.3.2 Modal Characteristics in Dirac-cone PCSEL

Figure 3-6 shows the amplitude of the magnetic field (H_z component) distribution around the airhole in a unit cell for four resonant modes in the direction perpendicular to the PC plane. To evaluate the lasing mode and estimate the gain threshold condition, the electric field distribution in at different z values perpendicular to the PC surface plane is simulated for all the modes and shown in Figure 3-7.
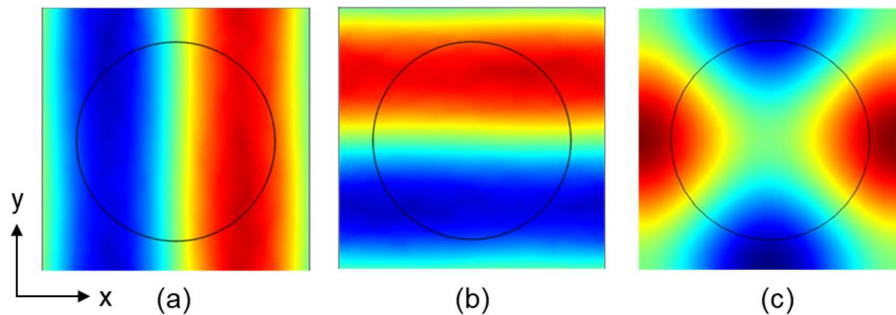
Figure 3-10 Magnitude of the in-plane H_z component of the three resonant modes in circular airhole Dirac-cone PC cavity (a) mode A; (b) mode B; and (c) mode C.
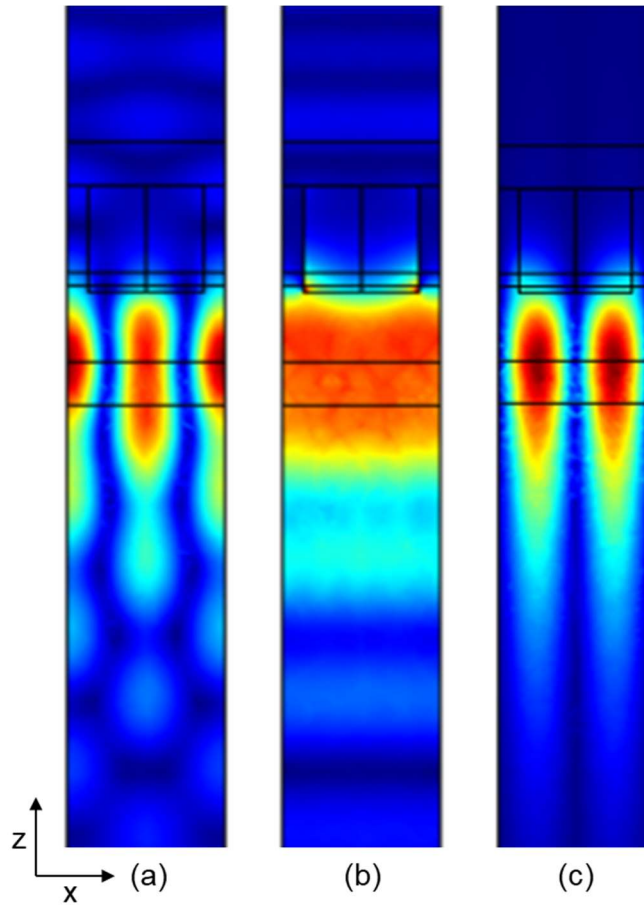
Figure 3-11 Magnitude of the E_y component of the three resonant modes in circular airhole Dirac-cone showing the optical confinement in the MQW active region (a) mode A; (b) mode B; and (c) mode C.

3.3.3 Gain Threshold Estimation of Modes in Dirac-cone PCSEL

The gain threshold values of the three degenerate modes are calculated based on the Q-factor, confinement factor, and radiation loss are summarized in Table 3-3. As discussed earlier, mode C with high-Q value of 5.35×10^5 has the lowest gain-threshold value of 5.32 cm^{-1} and the remaining two modes A and B gain-threshold values are three orders higher than of mode C. As a result, mode C would lase first and provides a large range of operating current for single mode emission.

Table 3-3 Modal characteristics of three resonant modes in circular airhole Dirac-cone PCSEL cavity at 1040 nm

Mode	λ (nm)	Q	α (cm^{-1})	Γ_{QW} (%)	g_{th} (cm^{-1})
A	1038.06	9.97×10^2	201.34	6.32	3185.83
B	1038.33	9.05×10^2	221.81	6.14	3612.58
C	1038.59	5.35×10^5	0.37	7.04	5.32

3.4 Double Lattice PCSEL Cavity Design

To achieve large area single mode PCSEL operation, double lattice is one of the PC geometries like circular airhole Dirac-cone. As introduced by Noda *et al.* double-lattice photonic crystal cavities contain two square lattices with secondary lattice shifted by one-quarter wavelength in x- and y-directions. The main advantage of the secondary airholes is the destructive interference created between the 180° diffracted waves that reduce the lateral confinement and suppress higher order modes. This results in large gain threshold difference between fundamental mode and higher order modes, and eventually increases the size of PCSEL device to mm scale with single mode emission.
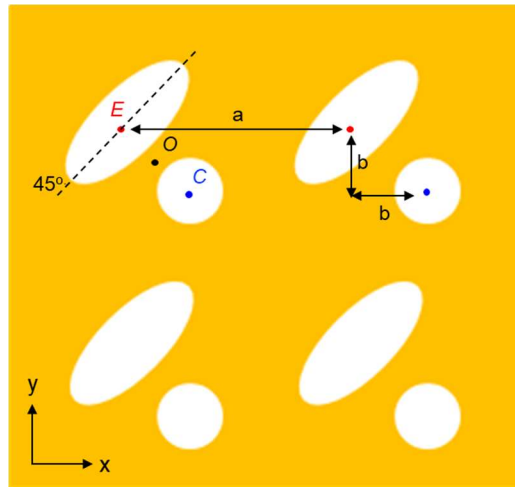
Figure 3-12 Schematic of the double lattice PC cavity top view. Note: *E* is the center of the ellipse which is rotated +45° in plane; *O* is the center of the unit cell; *C* is the center of the circle; *a* is the lattice constant, *b* is 0.25x*a* (quarter wavelength) spacing between primary and secondary lattice

Figure 3-12 shows the square double lattice PC cavity. The primary lattice is a 45°
rotated elliptical airhole square lattice and the secondary lattice is circular airhole square
lattice which is shifted by a quarter of lattice constant in the x- and y-directions in the plane
of PC surface. The thickness of the PC layer is varied to increase the gain the threshold of
the fundamental mode and higher order modes, as a result, the gain-threshold difference
between those two modes is also increased leading single mode operation even at larger
device sizes.

3.4.1 Cavity Resonance Modes in Double Lattice PCSEL

Similar to the triangular airhole PC cavity modes, four resonant modes are
observed at the frequency range close to 288 THz that corresponds to 1040 nm
wavelengths in the double lattice PC cavity as shown in Figure 3-13. The lattice constant,
a=313 nm, semi-major axis of ellipse x=96 nm, semi-minor axis of ellipse y= 43 nm and
radius of the secondary airhole r=39 nm.
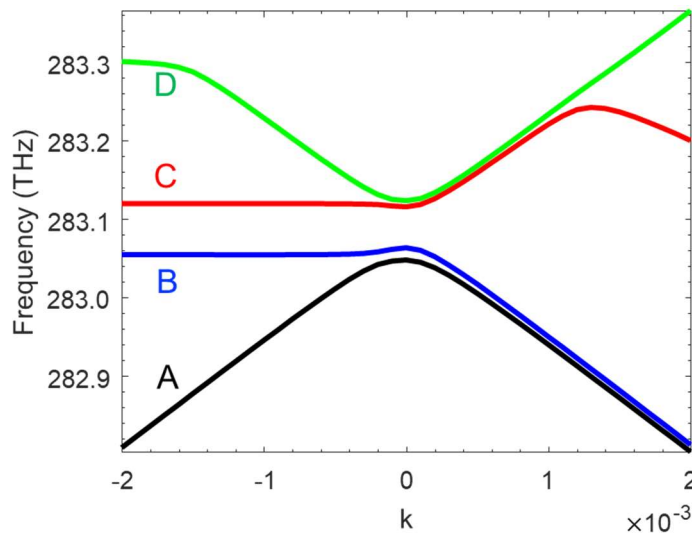
Figure 3-13 Resonant bands near k=0 (Γ_2 point) for the double lattice PC cavity, the TE-
like modes near the frequency of gain peak are named as A, B, C and D.

3.4.2 Modal Characteristics in Double Lattice PCSEL
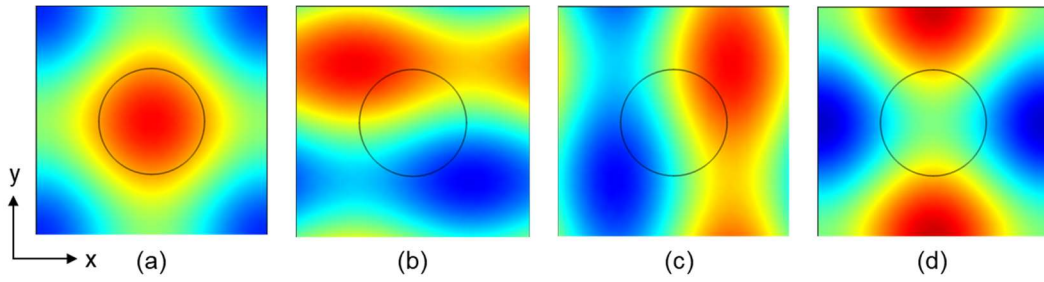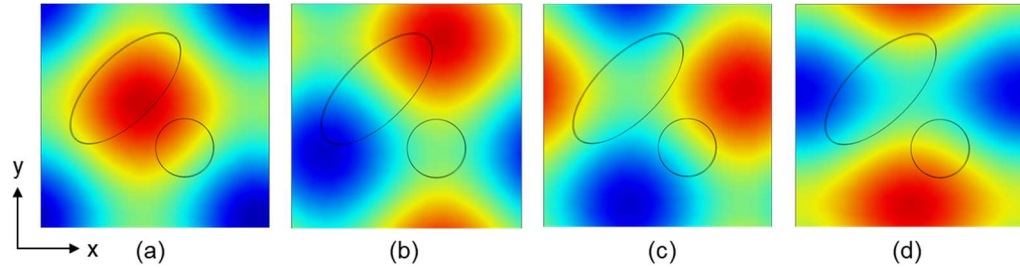

Figure 3-14 Magnitude of the in-plane H_z component of the four resonant modes in composite double lattice PC cavity (a) mode A; (b) mode B; (c) mode C; and (d) mode D.
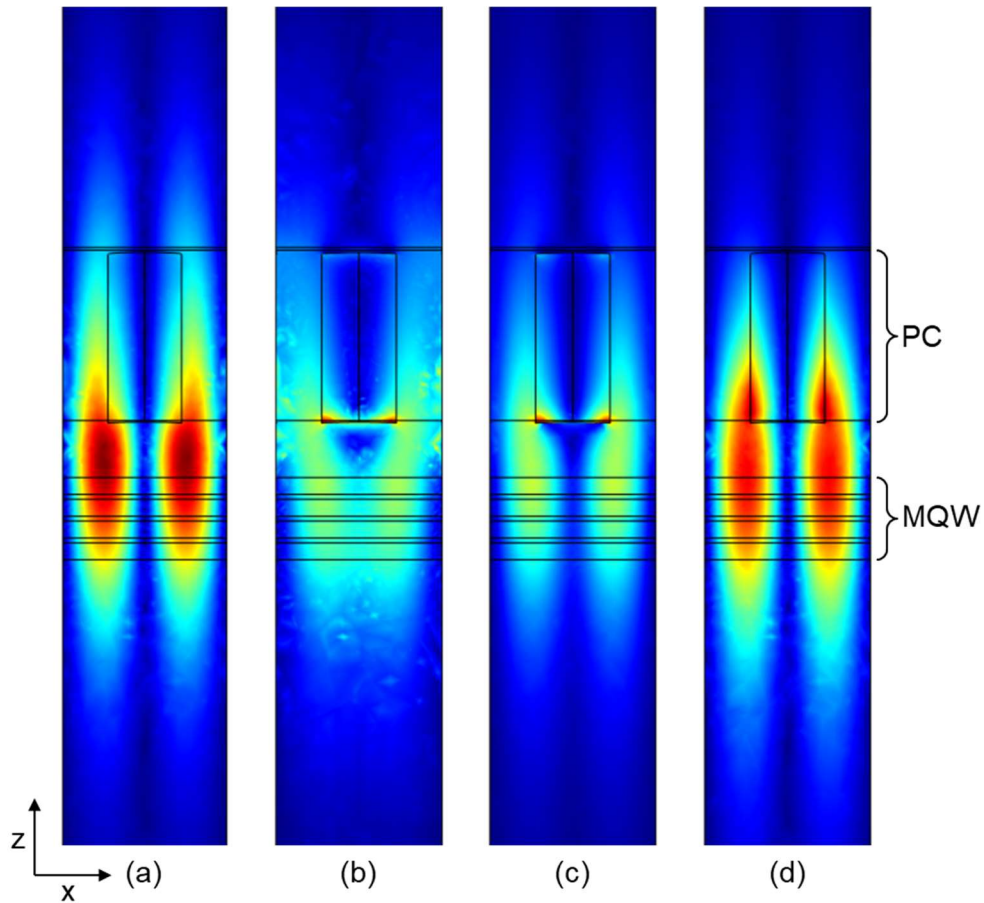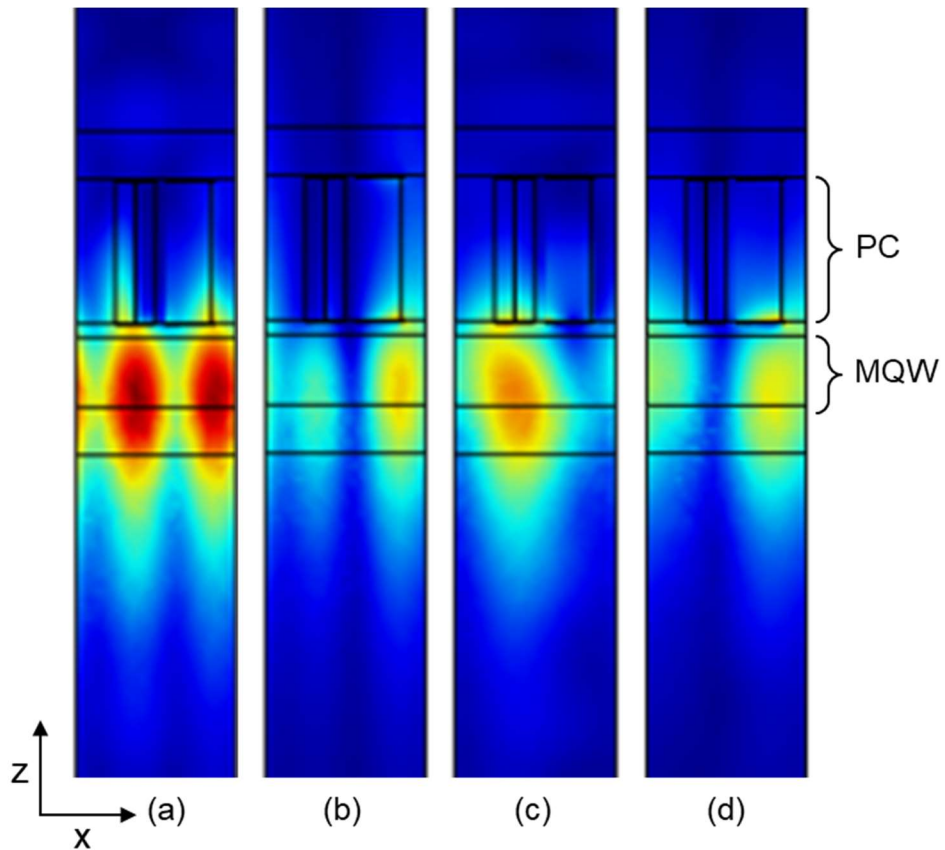

Figure 3-15 Magnitude of the E_y component of the four resonant modes in composite double lattice PC cavity showing the optical confinement in the MQW active region (a) mode A; (b) mode B; (c) mode C; and (d) mode D.

The four TE-like resonant modes as shown in Figure 3-13 have different electromagnetic field distributions. The amplitude of the magnetic field (H_z component) distributions in the direction perpendicular to the PC plane around the airhole in a unit cell for the respective resonant modes are shown in Figure 3-14. The lasing mode and the gain threshold condition are estimated based on the electric field distribution at different z values perpendicular to the PC surface plane for the respective modes as shown in Figure 3-15. The electric field confinement and Q-factor determines the lasing mode.

3.4.3 Gain Threshold Estimation of Modes in Double Lattice PCSEL

Based on these fundamental equations, the confinement factor, quality factor and radiation loss, the corresponding gain threshold values for each mode are calculated as shown in the Table 3-2.

Table 3-4 Modal characteristics of four resonant modes in double lattice PCSEL cavity at 1040 nm

Mode	λ (nm)	Q	α (cm^{-1})	Γ_{QW} (%)	g_{th} (cm^{-1})
A	1056.38	7.96 x 10^4	2.52	5.14	49.03
B	1056.31	2.45 x 10^4	8.19	4.92	166.51
C	1056.08	5.77 x 10^3	34.74	2.76	1258.99
D	1056.04	3.18 x 10^3	63.22	4.26	1484.16

As observed in the modal properties of the four modes, the Q-value and confinement factor for mode A is higher and caused lowest gain-threshold condition of 49.03 cm^{-1} for lasing. The next lower gain-threshold value is for mode B which is around 166.51 cm^{-1} and would also lase at higher current injection levels. Mode C and D would not lase even at high current injects as their gain-threshold values are more than ten times higher compared to lasing mode.

3.5 Analysis on Different PC Cavity Designs

The different PC lattice designs investigated above show different modal and lasing characteristics. The small circular airhole PC cavity design offers very low gain threshold condition, however the radiation loss α which corresponds to the emitted power leaking out through surface is very low. This is due to the symmetry in the in-plane electric field generated by symmetric circular airhole shape. As a result, the lightwaves coupled in four different directions in PC plane gets destructive interference for vertical diffraction and very less power is leaked out in surface normal direction.

To break the symmetry issue, right angled isosceles triangular airhole is considered and the airhole size is also enlarged to increase the radiation constant. This resulted in slightly higher gain-threshold condition than circular airhole PC, but the output power would be increased. In terms of modal characteristics, triangular airholes PC cavity has other modes with gain-threshold close to lasing mode limiting the device operation to be at lower current levels. Increment in current injection would lead to multi-mode emission. At the same time, scaling the triangular airhole PCSEL emitters to larger sizes would trigger higher order modes to lase decreasing the beam quality (brightness).

To suppress the multi-mode emission circular airhole Dirac-cone cavity is investigated. As observed, the gain-threshold difference between the lasing mode and non-lasing modes is very high in circular airhole Dirac-cone cavity. This expands the current injection levels to a few tens of Amperes without other modes lasing and results in high outpower in Watts range with single mode operation. Similarly, the Q-k relationship explored in detail in chapter 6 indicate that circular airhole Dirac-cone cavities and can be scale upto mm range while maintaining the single mode operation. Further investigation is required on Dirac-cone lattice design in terms of emitted power as there could be chances

42

of destructive interference happening in vertically diffracted lightwaves if the PC airhole shape is symmetric. To avoid that, a small perturbation can be created during the regrowth process like variation of airhole radius across the thickness of PC layer that can help reduce the destructive interference. In addition, in-plane the perturbation can also be created in the plane of PC by introducing a small secondary airhole as observed in double lattice PC cavity.

The double lattice PC cavity combines both the advantages of triangular airhole and Dirac-cone cavities. It provides the asymmetry in the airhole to nullify the destructive interference in vertically diffracted lightwaves and at the same time increases the differential gain-threshold between fundamental mode and higher order modes. As a result, double lattice PCSELs can be operated at high current levels and emit high output power in tens of Watts with single mode operation. Higher output power in hundreds of Watts can be achieved by expanding the device size to mm scale while precisely adjusting the spacing between the primary and secondary lattices to maintain the differential gain-threshold. At extremely high current injections, greater than ten times threshold, mode B would also start to lase in double lattice cavities, in contrast this does not happen in Dirac-cone as the next lasing mode gain-threshold is ten times higher than that of lasing mode. However, the gain-threshold for lasing mode in double lattice PC cavities would be higher than that of triangular airhole and Dirac-cone cavities for the same device size.

Therefore, it depends on the end user requirements to consider the PC cavity design. For output power in Watts range, triangular airhole can be employed with comparatively low-gain threshold condition. For output in tens of Watts with large single mode regime Dirac-cone is the good choice. For extremely high output power in hundreds of Watts, with compromised multi-mode emission at high current injection, double lattice cavities can be explored.

Chapter 4

PCSEL FABRICATION

The PCSEL device fabrication process is composed of three primary steps: Initial growth, photonic crystal patterning, and regrowth. In the initial growth n-AlGaAs cladding layer, an active layer containing InGaAs/GaAs multi quantum wells (MQWs), an AlGaAs electron-blocking layer and a GaAs layer are successively grown on an n-GaAs substrate using the Molecular Beam Epitaxy (MBE) process as shown in **Error! Reference source not found.**. The photoluminescence is measured from the initial growth heterostructure to confirm the quality, uniformity and peak wavelength of the MQWs active region across different regions on the 2-inch wafer as shown in Figure 4-1(a) and (b). Depending on the indium composition in the InGaAs QWs, the peak wavelength of the photoluminescence spectrum changes from 980 nm to 1040 nm.
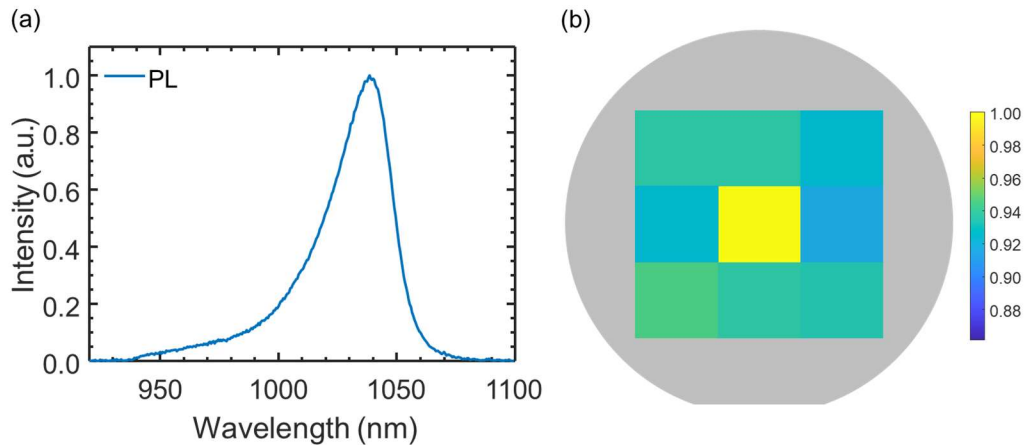
Figure 4-1 Surface photoluminescence (PL) measured from the half-laser heterostructure (initial growth) to confirm the peak wavelength of the QWs; and (b) PL mapping at different regions of a 2-inch wafer heterostructure to verify the uniformity of emission wavelength and peak intensity at different regions

4.1 Circular Airhole PCSEL Fabrication

4.1.1 Circular Airhole PC Cavity Pattering

The second step is the e-beam lithography (EBL) process to pattern the photonic crystal cavity on GaAs layer. A 10 mm x 10 mm square piece (sample) is cleaved from the 2-inch wafer with peak photoluminescence at 980 nm from $In_{0.18}Ga_{0.82}As/Al_{0.25}Ga_{0.75}As$ QW/Barrier active region as shown in **Error! Reference source not found.**. It is spin coated with positive tone e-beam grade resist ZEP520A at 2000 rpm for 60 seconds and baked at 180 °C for 3 minutes. The thickness of the e-beam resist after the spin coating is around 523 nm and can be varied by changing the spin speed as required for the PC design. Later the sample is loaded into Zeiss 1540XB Crossbeam e-beam lithography tool to pattern the photonic crystal with circular airhole shapes. Post exposure, the sample is dipped in the N-amylacetate solution to develop the e-beam resist pattern. Later, the airholes are etched into the GaAs layer using III-V Reactive-Ion Etching (RIE) process using 1 sccm of $SiCl_4$ flow in TRION Minilock chamber at 2 mTorr pressure and 38 W RIE power.

(a)   (b)
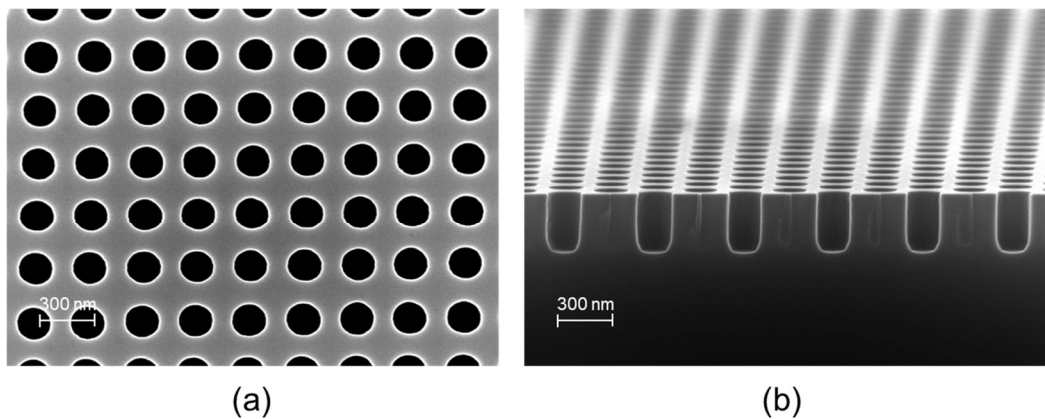
Figure 4-2 SEM images of the etched circular airhole square lattice photonic crystal cavity (a) top view showing the uniformity of airhole shape; (b) cross-section view showing the etch depth

After the etching process, the e-beam resist is removed by dropping the sample in n-methyl-2-pyrrolidone bath at 80 °C on hot plate for 10 minutes, followed by 5 min ultrasonication. The sample is then transferred into Isopropanol alcohol (IPA) solution for 10 minutes ultrasonication. Finally, the sample with clean surface is dipped in 1:10 Hydroflouric acid: Water (HF:H_2O) solution for 60 sec to remove any oxide layer formed inside the airholes. In addition, oxygen plasma ashing is carried out for 30 minutes to remove any e-beam resist residues or organic material inside the airholes.

4.1.2 Epitaxial Regrowth using MBE Process

The third fabrication step is to regrow a p-AlGaAs cladding layer and p-GaAs contact layer on the PC samples using molecular beam epitaxy (MBE) process. Though the regrowth process is extensively implemented in the fabrication of distributed feedback (DFB) lasers, the considerable higher aspect ratio features in PCSELs create challenges. To mitigate electrical and optical losses, interface quality plays a critical role in achieving high power lasing. In addition, it is important to match the resonance of the PC cavity to the photoluminescence (PL) from the active region. While epitaxial regrowth provides a structural advantage compared to wafer bonding, it complicates the optimization of PC design parameters such as air-hole size and shape, as there is infilling during regrowth. Optimization of regrowth conditions account for infilling becomes key challenges for obtaining PC cavity airholes of the desired size and shape.

MBE is an ultra-high vacuum growth system and is highly sensitive to the surface contaminants during the regrowth process. This may cause surface defects and interfaces quality issues that result in higher electrical and optical losses. Before loading the samples in MBE reactor, sample is soaked in H_2SO_4 for 5 minutes and subjected to thermal cleaning

at 550 °C to remove the native surface oxide [50], [51]. This avoids the 610 °C high temperature oxide desorption process inside the MBE chamber that may deform the hole shape. This process yields regrowth surface with low surface defect density and consistent airhole shape and size as shown in Figure 4-3(a) cross-section SEM images after the regrowth process. The growth rate usually depends on the various crystal planes (such as (100), (110) and (111)) inside the air holes. The growth rate is reduced inside the airhole due to reduction of gas source inside the airholes forming a tear-drop embedded airholes. As a result, these airholes are sealed-off before the crystal growth within the airholes with good interface quality. The surface normal reflection spectrum measured to confirm the resonance after the regrowth is in good agreement with the simulated spectra as shown in Figure 4-3(b).
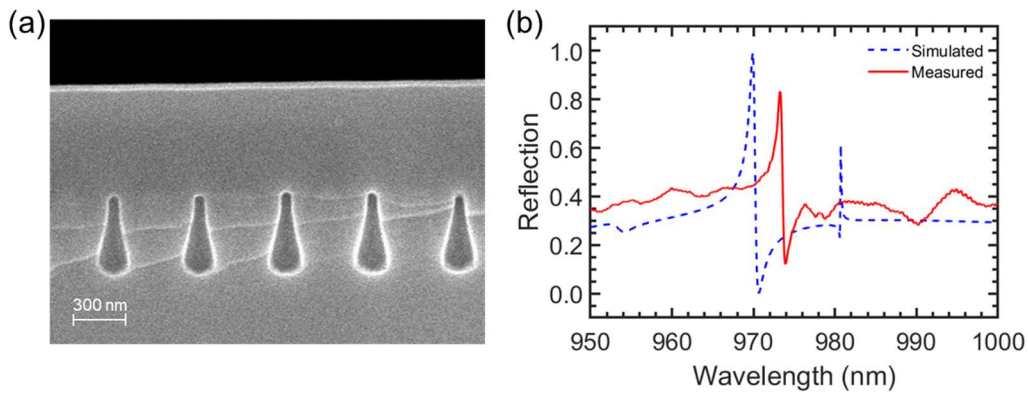
Figure 4-3 (a) Cross-section SEM image of the circular airhole PC cavity after the MBE regrowth; and (b) measured and simulated surface normal reflection spectra

4.1.3 Circular Airhole PCSEL Fabrication with P-ring Epi-up Design

After the regrowth process, the PC sample is optically tested to confirm the resonance and surface quality. Once characterized, standard micro-photolithography processes are used for the complete device fabrication. P-ring electrode design was

employed for the fabrication of PCSEL. In this design, first p-ring electrode of Pd/Ti/Pd/Au

with 100 µm emission window and 25 µm ring-width is deposited using e-beam

evaporation process as shown in

Figure 4-4.

(a) Epitaxial growth   (b) Photonic crystal pattern   (c) Regrowth

(d) p-ring deposition   (e) Mesa etching   (f) N-ring deposition
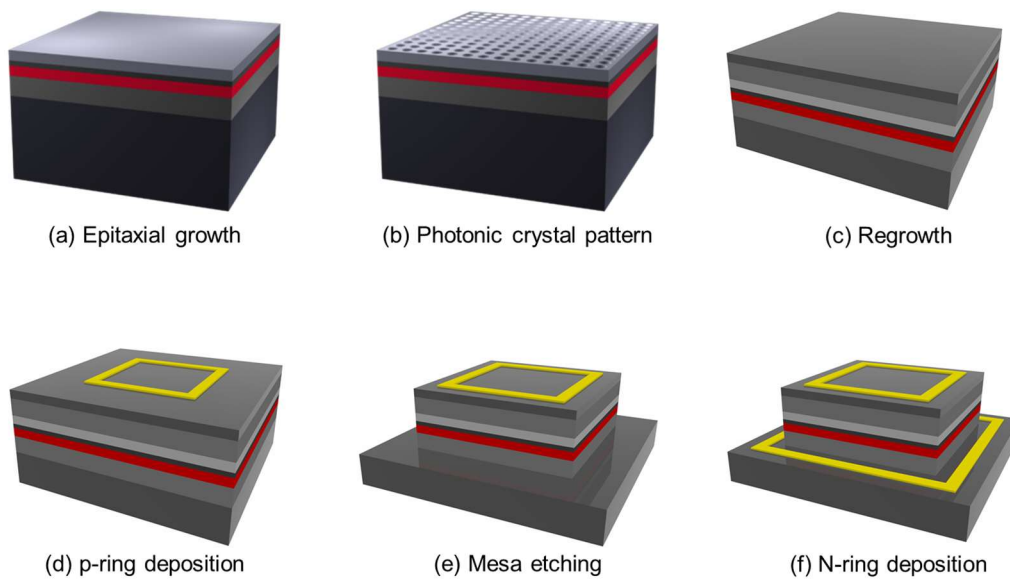
Figure 4-4 Schematic of the PCSEL p-ring electrode design fabrication process (a) initial epitaxial growth; (b) patterning of photonic crystal cavity; (c) AlGaAs and GaAs regrowth process using MOCVD; (d) p-ring electrode deposition using e-beam evaporator; (e) p-mesa etching to access n-contact layer; and (f) n-metal ring electrode deposition using e-beam evaporator and annealing

The samples are loaded into CHA solution e-beam evaporator and sequential

metal layers are deposited at 3.5×10^{-6} Torr pressure condition. Followed by 300 sec p-

mesa wet etching process using H_3PO_4:H_2O_2:H_2O solution at 1:1:10 ratio to achieve etch

depth of 3.5 µm. This gives access the n-GaAs contact layer. The n-ring electrode

Ni/Ge/Au/Ti/Au is deposited on the n-GaAs contact layer using e-beam evaporation process as shown in

Figure 4-4(f) and annealed at 400 °C for 60 seconds.

4.1.4 L-I-V and Emission Characteristics of Circular Airhole PCSEL

The double-ring structure as shown in Figure 4-5(a) contains p-ring electrode in the center on the mesa of width 250 µm and n-ring electrode outside the mesa on the n-contact layer. The side length of the PC cavity is 200 µm and the p-ring emission window is 100 µm with the width of p-ring electrode to be 25 µm. This epi-up design PCSEL is electrically injected by using Newport ILX Lightwave LDP 3811 current source under quasi CW operation with pulse width of 500 ns and 50% duty cycle. The positive probe of the current source is connected to the island p-pad which extends to the center p-ring electrode. Similarly, the negative probe is connected to the island n-pad outside the mesa area. With current injection above 300 mA, high illumination around the p-ring electrode is captured using Moticam 1080P high resolution camera mounted on 10X objective lens on Cascade Microtech MPS 150 probe station as shown in Figure 4-5(b). It is clearly visible that the emission intensity is not uniform. High intensity is observed near the electrode region than the center region indicating current crowding and charge is not laterally diffusing.

Figure 4-5(c) and (d) shows the spectrum and L-I-V characteristics of the double-ring PCSEL measured under pulsed operation. The emission from the electrically pumped PCSEL is collected into a multi-mode pigtail fiber placed close to the emission window in surface normal direction, which is coupled into optical spectrum analyzer (OSA) for the spectral analysis. Above the threshold at 400 mA CW operation at room temperature, single dominant mode is observed near 998 nm with multiple low-Q peaks around the

dominant mode with side mode suppression ratio (SMSR) of 6 dB. These small peaks correspond to other resonant bands as observed in the photonic band structure of the circular airhole PC cavity.
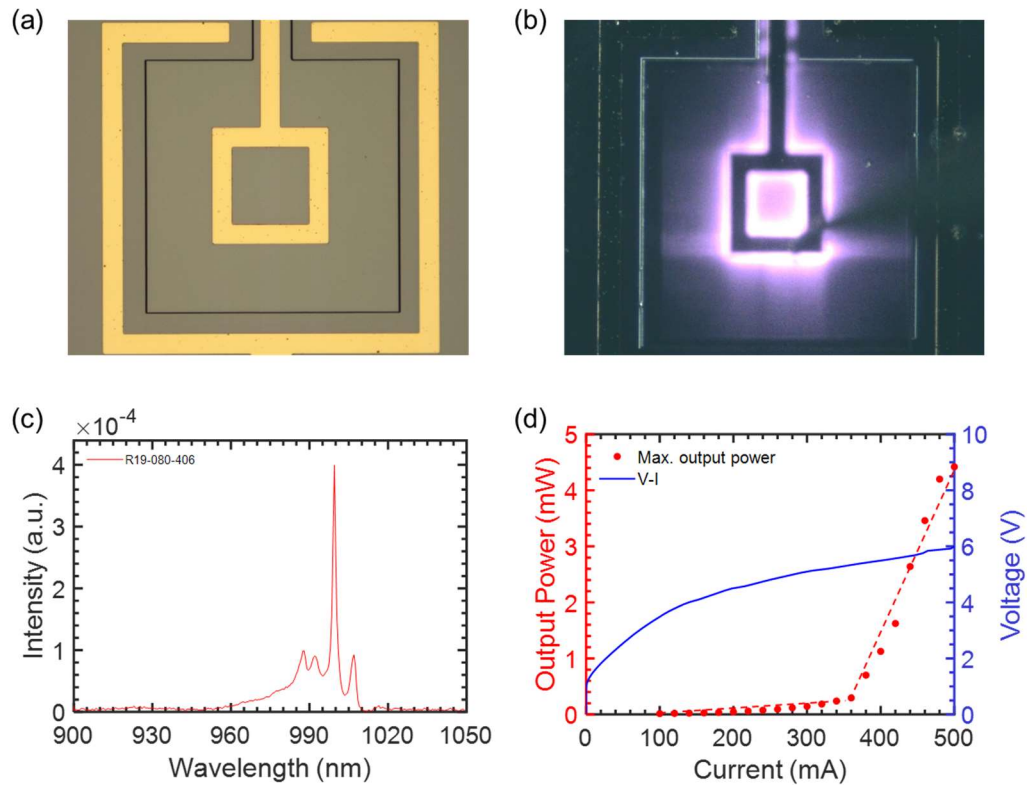
Figure 4-5 P-ring electrode design PCSEL lasing characteristics (a) Optical micrograph showing the p- and n-ring electrodes after complete device fabrication; (b) emission captured from the PCSEL at 400 mA current injection; (c) electrical spectrum measured above the threshold showing dominant mode at 997 nm; and (d) L-I-V plot showing the threshold value of 350 mA and larger voltage drop indicating high series resistance.

The multi-mode emission is mainly due to the high Q-factor values of all the modes near the Γ point, as such small airholes PC cavities increase the Q-values. This results in low gain-threshold values for all the modes. Eventually the gain-threshold difference between lasing mode and other modes would reduce causing multi-mode emission. In addition, non-uniform emission is observed causing temperature variation within the PC

region. As a result, the refractive index of PC layer varies locally causing multi-mode emission spatially. Due to current crowding as seen in Figure 4-6(a), the I-V curve in Figure 4-6(b) indicates a high series resistance of 42Ω against the simulated 0.7Ω which is almost two orders higher. The emitted power is around 5 mW at 500 mA of current, the slope efficiency is 4 mWA^{-1} and mainly limited by the thermal issues due to quasi-CW operation. As discussed in the section 3.1.5, circular airhole PC cavity mode gets destructive interference from vertically diffracted lightwaves in the PC cavity due to the in-plane symmetry in PC resulting in less or no surface normal emission. In order to increase the surface normal output power, the Q-values should be reduced, and the in-plane symmetry should be broken to achieve constructive interference between in-plane diffracted lightwaves. This can be achieved with triangular airhole PC cavity as discussed in section 3.2.1.

4.1.5 Current Crowding and Series Resistance

One of the main issues observed in p-ring electrode design is that emission can only be achieved near the p-ring electrode region. When a large p-ring contact with a 150 μm opening on top of the PCSEL is placed with less than 2 μm separation from the QW layer, the lateral carrier diffusion limits the hole injection uniformity in the QW region. This not only degrades beam quality, but also wall-plug efficiency is critically reduced due to non-uniform charge injection. High current crowding is observed at the regions below the metal contact as shown in Figure 4-5(b).

Due to the non-uniformity of charge injection, the surface emission profile is also non-uniform. This results in high series resistance and heating issues that limited the device performance in terms of power. In addition, the charge density is higher at some

regions, this results in temporal variation of refractive index locally at different PC regions and further degrades the beam quality.

(a)   (b)
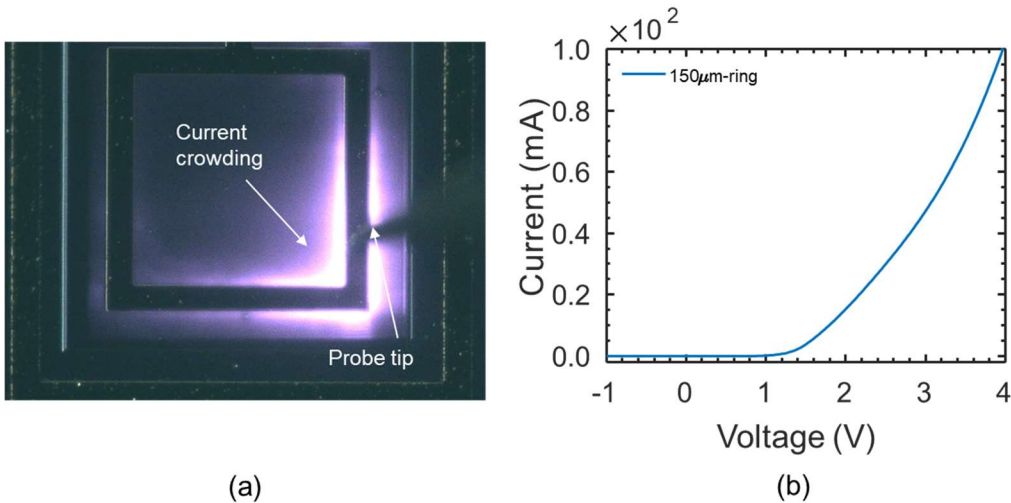
Figure 4-6 (a) Micrograph image showing the current crowding issue on the 150 µm window larger p-ring PCSEL design; and (b) I-V curve with larger series resistance of 42 Ω due to current crowding

4.2 Electrode Design Optimization

Detailed investigations were carried out experimentally and on simulations to investigate the charge distribution and current crowding issues. A 200 µm x 200 µm PCSEL model is developed with the heterostructure defined in **Error! Reference source not found.** using Rsoft LaserMOD software to simulate the electrical characteristics like I-V curves, charge density in the QWs region, charge accumulations at the interfaces of epitaxial layers and current crowding at the electrode edges. For a 150 µm emission window PCSEL with two ring contacts, we observe charge injection mostly in the contact

region as seen in Figure 4-7(a) and (c). This is mainly due to charge accumulation below the p-metal without sufficient lateral diffusion [52]. By replacing the p-ring with a p-disk contact as shown in Figure 4-7(b) and (d), uniform charge injection is obtained even for large cavity of size 200 µm. In both cases, a very large n-ring contact is placed at greater than 150 µm away from the QW region. Such a thick n-type layer ensures sufficient lateral charge diffusion and uniform charge injection into the QW region.
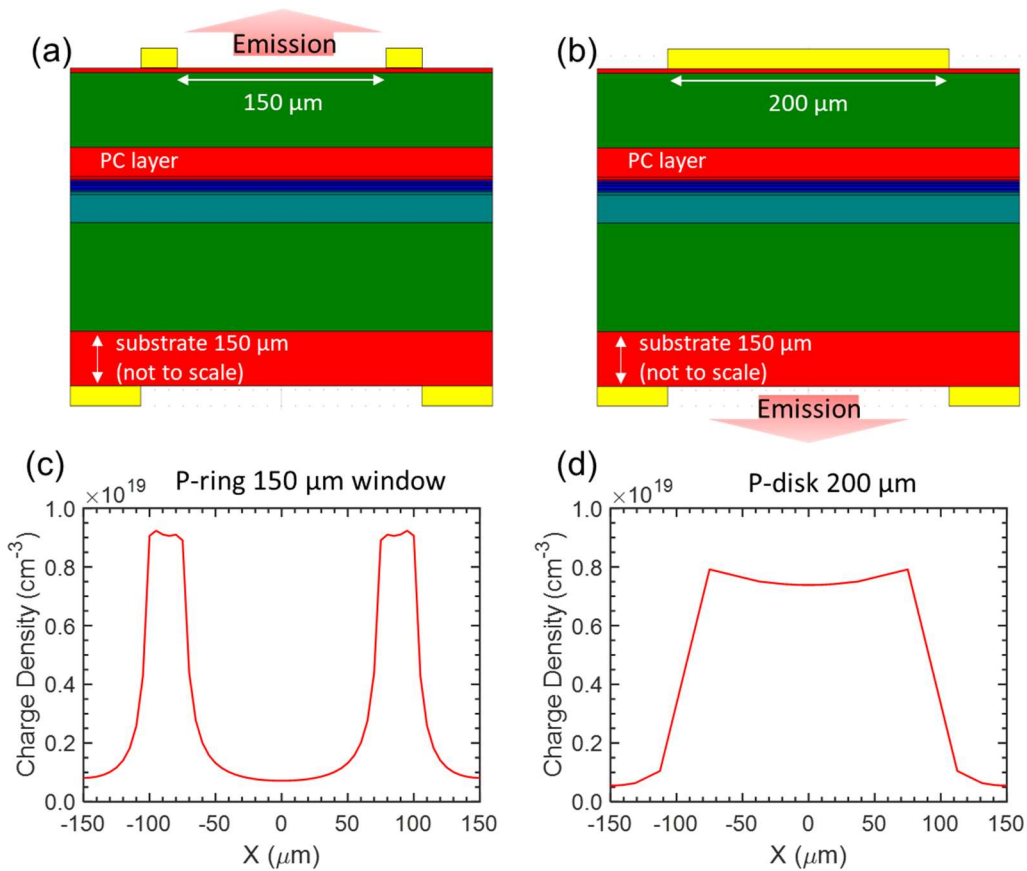
Figure 4-7 (a) Schematic and (c) carrier distribution of PCSEL structure with 150 µm p-ring (b) Schematic and (d) carrier distribution in QWs of PCSEL structure with 200 µm p-disk. Note a 200 µm n-ring electrode was placed with 150 µm n-type substrate

Further investigations on the impact of p-ring contact for smaller size PCSELs are carried out and the results are shown in Figure 4-8. For the double ring contact, the

maximum device size with uniform charge injection is ~10 μm, where the carrier concentrations vary from 2.2×10^{19} to 1×10^{19} cm^{-3}. Beyond that, we see much larger variations in carrier distribution, with center carrier concentration drops by almost an order of magnitude.
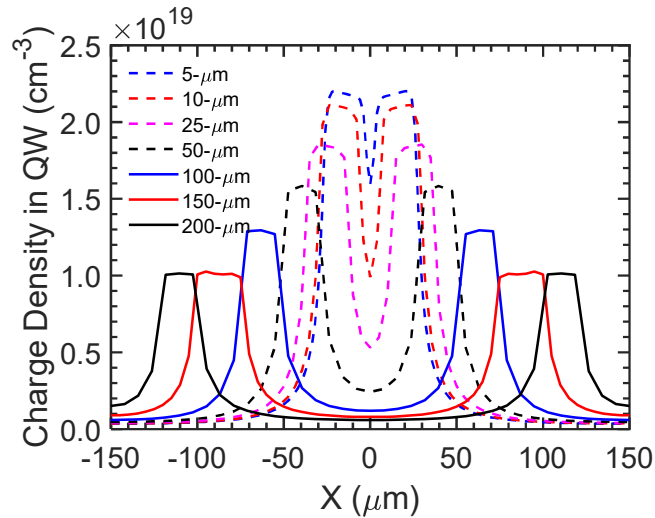
Figure 4-8 Charge density distribution with p-ring contact scheme for different aperture size PCSELs.

4.3 Contact Resistance Optimization

It is extremely important for the high current level operated PCSEL devices to have low series resistance R_{series} in the orders of a few milli ohms [53]. High series resistance may not be significant at low current operation, but at high current operation, high voltage drop occurs near the PCSEL device terminals that reduces the wall-plug efficiency. Typically, the series resistance of laser diode is due to three factors: resistance of the p- and n-metals ($R_{p\text{-}metal}$ and $R_{n\text{-}metal}$ usually both are negligible), contact resistance between metal contacts and semiconductor ($R_{p\text{-}contact}$ and $R_{n\text{-}contact}$), and resistance from the

semiconductor (R_{semi}) mostly due to intrinsic layers as shown in the Figure 4-9. Therefore, the primary step to reduce series resistance is to optimize ohmic-contact metals and annealing process.
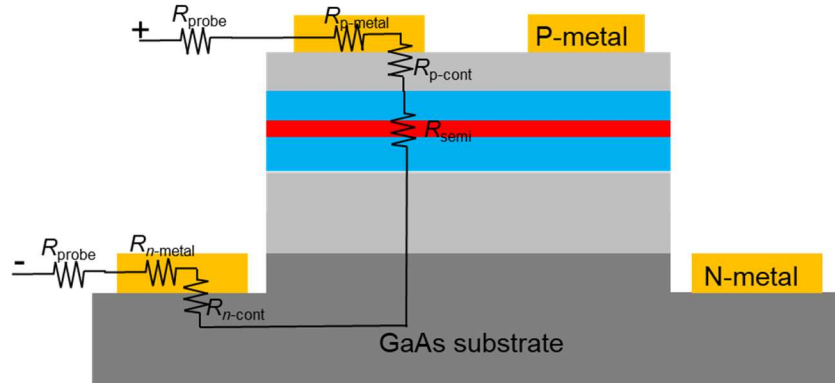
Figure 4-9 Schematic of the p-ring electrode design PCSEL showing series resistance caused at different regions and material interfaces

$$R_{series} = R_{p-met} + R_{n-metal} + R_{p-contac} + R_{n-contact} + R_{semi} + R_{probes} \qquad (4.1)$$

By reducing the contact resistance between the metal and semiconductor, the series resistance can be reduced. The standard process to reduce the contact resistance is Rapid Thermal Annealing (RTA) [54] process after the deposition of the metal contacts. RTA enhances the diffusion of the metal dopants into the semiconductor contact layers and provides local doping. Therefore, optimization of ohmic contact stack and annealing temperature are important aspects of device fabrication process.

To optimize the contact resistance, circular transmission line model (CTLM) structures are deposited on the substrate. The advantage of CTLM structures is that the etch step is not required to isolate the structures and current crowding is avoided providing better confinement of the current between the contacts [55]. Metal stacks are deposited

using e-beam evaporation process on a 20 mm x 20 mm samples and cleaved into several smaller 5 mm x 5 mm pieces. Each small piece is loaded into RTA tool separately to anneal at different temperatures. Figure 4-10(a) shows the top view of the CTLM structures on the sample with metal stack deposited.

The inner radius of the CTLM structure is defined as R_1 which is a constant value of 100 µm and the outer radius R_2 varies as the spacing S between the R_1 and R_2 is varied from 2 µm to 20 µm as shown in Figure 4-10(b) and (c). In the circular transmission line model, two electrical probes are used, one placed on the inner disk and other on the outer ring, to measure the voltage drop. The resulting I-V curves are plotted for each measurement and the slope of the curve is used to extract the total resistance R_T corresponding to different spacing between the inner disk and outer ring.
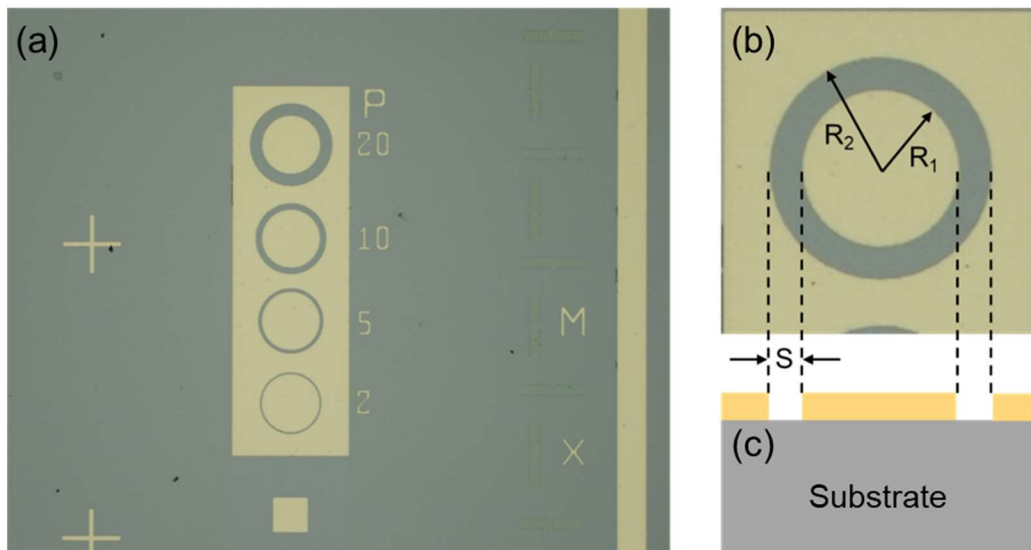
Figure 4-10 (a) Circular transmission line model (CTLM) structures of various spacing deposited on the heterostructure to measure the contact resistance; (b) top view of the CTLM showing the spacing, inner and outer radii; and (c) schematic of the CTLM cross-section view

The total resistance R_T between the two probes is defined as:

$$R_T = \frac{R_{sh}}{W_c}(S + 2L_t)C \tag{4.2}$$

$$W_c = 2\pi R_1 \; (\mu m) \tag{4.3}$$

$$R_c = \frac{R}{2} \; (\Omega) \tag{4.4}$$

$$L_t = \frac{L}{2} \; (\mu m) \tag{4.5}$$

$$\rho_c = R_{sh}L_t{}^2 \; (\Omega cm^2) = R_c W_c L_t \; (\Omega cm^2) \tag{4.6}$$

$$C = \frac{R_1}{S} \ln\left(\frac{R_1+S}{R_1}\right) \tag{4.7}$$

where R_{sh} is the sheet resistance, W_c is the perimeter of the inner disk, L_t is the transfer length, C is the correction factor, R_c is the contact resistance and ρ_c is the contact resistivity. Additional information relating to the derivation of this equation can be found in reference [56].
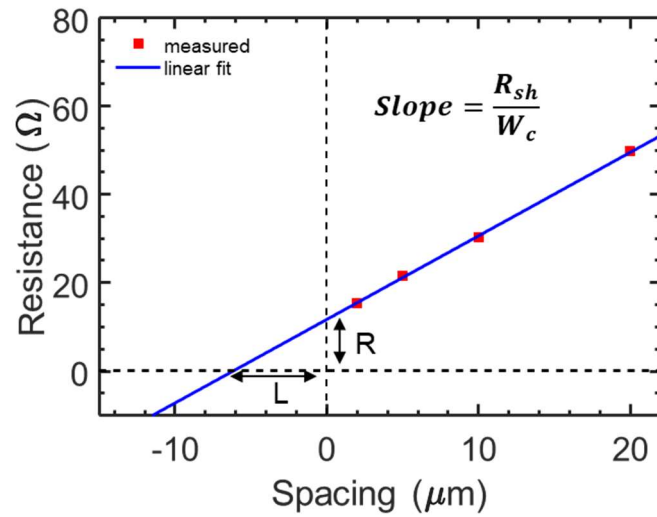
Figure 4-11 Measured resistance values at different spacing values of CTLM structures to extract the contact resistance R_c and contact resistivity ρ_c

As the contact geometry is different from the standard rectangular transmission line method (TLM) structures, correction factor C is applied to compensate this variation. Therefore, the accurate value of contact resistivity ρ_c can be extracted using CTLMs that matches the TLM. Figure 4-11 shows the measured resistance and linear fit as a function of spacing between the inner disk and out ring under same annealing temperature. The y-intercept of the linear fitted line the figure gives the value of $2R_c$ that includes the resistance of the two probes. The x-intercept give the value of $2L_t$ which is used in the calculation of contact resistivity ρ_c for the metal stack annealed at a particular temperature.

Multiple ohmic contact metal stacks are investigated that provides the low contact resistance for both p- and n-contact interface. All these metal stacks are annealed at different temperatures. Typical annealing temperature profile at 400 °C for 60 seconds is shown in Figure 4-12. The corresponding contact resistivities at different annealing temperatures are calculated. Figure 4-13(a) shows the contact resistivity of four p-metal stacks Ti/Pd/Au, Ti/Zn/Au, Pd/Ti/Pd/Au and Ti/Au deposited on highly doped p-GaAs wafer

with doping concentration in the order of 2 x 10^{19} cm^{-3}. These metal stacks are annealed at various temperatures from 380 °C to 440 °C in the presence of N$_2$ gas using JetFirst RTA tool. The lowest contact resistivity of 4 x 10^{-5} Ωcm^2 is observed for Pd/Ti/Pd/Au stack at 400 °C annealing temperature.
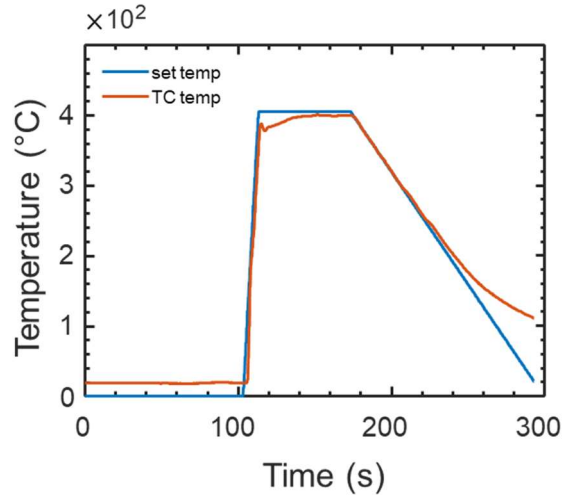
Figure 4-12 Annealing temperature profile optimized to reduce the contact resistance at electrode-semiconductor interfaces in PCSEL devices

A similar experiment was carried out by depositing Ni/Ge/Au/Ti/Au and Au/Ge/Au/Ni/Au metal stacks on n-GaAs substrate with doping concentration in the order of 2 x 10^{18} cm^{-3} as shown in Figure 4-13(b). The annealing temperature is varied from 300 °C to 420 °C. The graph shows decreasing contact resistance values as the annealing temperature is increased. The result indicates a lowest value of contact resistivity of 9 x 10^{-5} Ωcm^2 can be achieved for Ni/Ge/Au/Ti/Au stack at 400 °C annealing temperature. For the PCSEL fabrication, first Pd/Ti/Pd/Au is deposited on the p-GaAs, followed by the series of steps explain in section 3.3.4 and Ni/Ge/Au/Ti/Au deposited on the backside of the n-

GaAs substrate after polishing. Both the metals are annealed at 400 °C in the presence of N$_2$ gas for 60 sec.
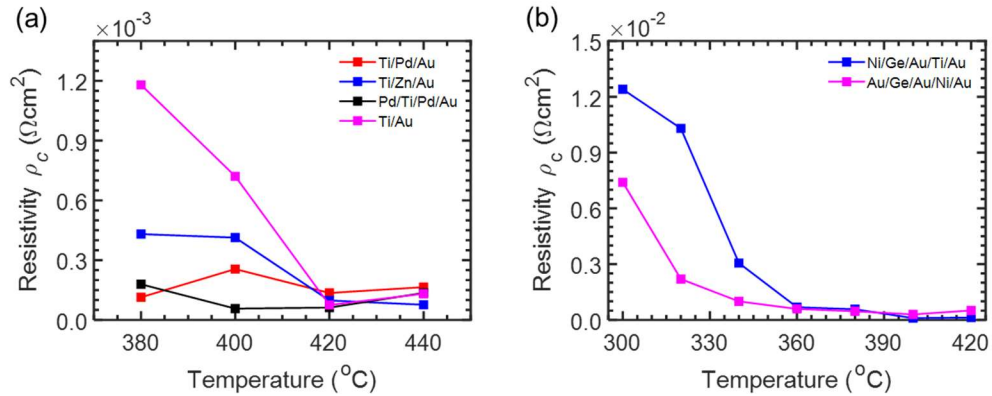
Figure 4-13 Contact resistivity measured at different annealing temperature conditions for (a) various p-metal stacks; and (b) various n-metal stacks

4.4 Triangular Airhole PCSEL Fabrication

The main advantage to change the PC design to triangular airhole from circular airhole is that the in-plane PC symmetry can be broken to reduce the destructive interference of the vertically diffracted lightwave in the plane of PC cavity. As a result, the output power can be maximized. The triangular airhole square lattice PCSEL is designed on the optimized heterostructure to reduce the series resistance caused due to accumulation of charge at the AlGaAs-GaAs layer interfaces. In addition, the electrode design is changed from the p-ring to p-disk based on the LaserMOD simulations. Thirdly, the contact resistance is reduced by changing the metal stacks and annealing temperatures of p-metal and n-metal ohmic-contacts.

4.4.1 Triangular Airhole PC Cavity

The e-beam lithography (EBL) process is further optimized to pattern the photonic crystal cavity on GaAs layer. Similar to the circular airhole PC sample, a 10 mm x 10 mm square piece (sample) is cleaved from the 2-inch wafer with peak photoluminescence wavelength at 1040 nm from $In_{0.25}Ga_{0.75}As$/GaAs QW/Barrier active region from improved 1040 nm heterostructure with e-blocking layer and graded AlGaAs layers as shown in **Error! Reference source not found.**. Later spin coated with the positive tone e-beam grade resist ZEP520A at 2000 rpm for 60 seconds and baked at 180 °C for 3 minutes. Later the sample is exposed to e-beam using JEOL JBX6300FS EBL tool to pattern the photonic crystal with triangular airhole shapes. An array of 8x8 PC cavities of size 200 μm are patterned with varying lattice constant '*a*' in the columns. The side length of the triangular airholes is maintained constant over all the 64 patterns to make sure uniform etch depth is achieved as PC etch rate mainly depends on feature size.

Post exposure, the sample is dipped in the N-amylacetate solution to develop the e-beam resist pattern. Similar to the circular airholes PC, the triangular airholes are etched using III-V Reactive-Ion Etching (RIE) process using 1 sccm of $SiCl_4$ flow in TRION Minilock chamber at 2 mTorr pressure and 38 W RIE power. After the etching process, the e-beam resist is removed by soaking the sample in n-methyl-2-pyrrolidone bath at 80 °C on hot plate for 10 minutes, followed by 5 min ultrasonication. The sample is then transferred into Isopropanol alcohol (IPA) solution for 10 minutes of ultrasonication. Finally, the e-beam resist is removed and sample with clean surface is dipped in 1:10 Hydroflouric acid (HF): Water H_2O solution for 60 sec to remove any oxide layer formed inside the airholes. Oxygen plasma ashing is carried out for 60 minutes to remove any e-beam resist residues or organic material inside the airholes.

This 2D PC cavity is of square lattice '*a*' varying from 309 nm to 323 nm across eight columns with step of 2 nm. The lattice constant tuning covers the entire gain spectra from 1040 nm $In_{0.25}Ga_{0.75}As$ QWs. As designed, the airhole has right-angled isosceles triangle shape with side length of 273 nm as shown in the Figure 4-14(a) top view scan electron microscope (SEM) images taken after RIE etching from a square lattice triangular airhole PC cavity with *a*=309 nm. The side length of each PC pattern is 200 μm and the airhole shape is uniform across different PC regions. Figure 4-14(b)shows the cross-section scan electron microscope (SEM) images of the etched sidewalls of the airholes that are very smooth and straight without any defects.

(a)   (b)
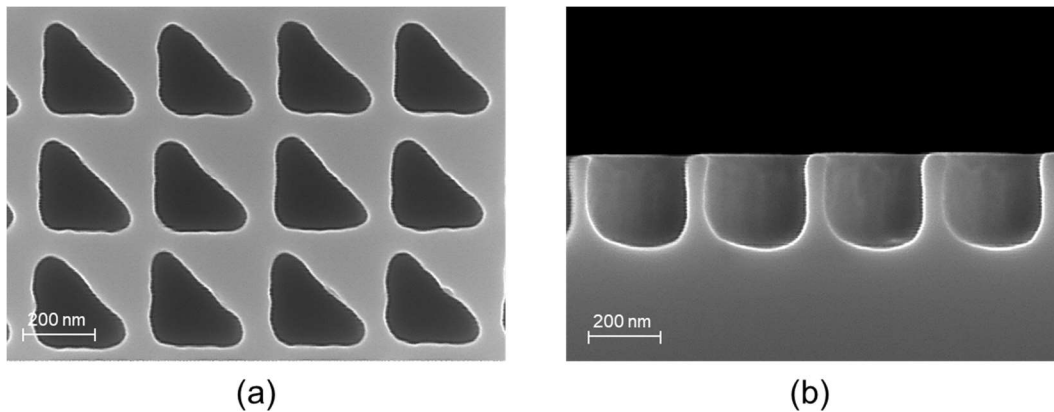
Figure 4-14 SEM images of the etched triangular airhole photonic crystal cavity (a) top view showing the uniformity of airhole shape; (b) cross-section view showing the etch depth

Following the RIE process, the PC cavities are immediately characterized using the micro-photoluminescence set up shown in Figure 5-1 to experimentally verify the wavelength of resonance modes match with the gain peak. In addition, Q values are also calculated for each resonant mode using the optical pumping and surface normal reflection measurement process explained in the later sections.

4.4.2 Epitaxial Regrowth using MOCVD Process

Once the resonance is confirmed, in the third fabrication step, a p-AlGaAs cladding layer and p-GaAs contact layer are grown on the PC samples. Unlike circular airholes PCSEL that is regrown with MBE process, triangular airholes PCSEL is regrowth using metalorganic chemical vapor deposition (MOCVD) process. The regrowth process is well optimized to preserve the PhC airholes as shown in Figure 4-15(b) cross-section SEM images after the regrowth process. The growth rate usually depends on the various crystal planes (such as (100), (110) and (111)) inside the air holes. The slow growth rate inside the airholes due to reduction of gas source inside the airholes forms a diamond shape embedded airholes with good interface quality and low surface roughness. As a result, these airholes are sealed-off before the crystal growth is completely planarized. Multiple cleaning recipes including HF:H_2O 1:10 dip is used before the regrowth process to achieve clean regrowth surface quality.

(a)   (b)
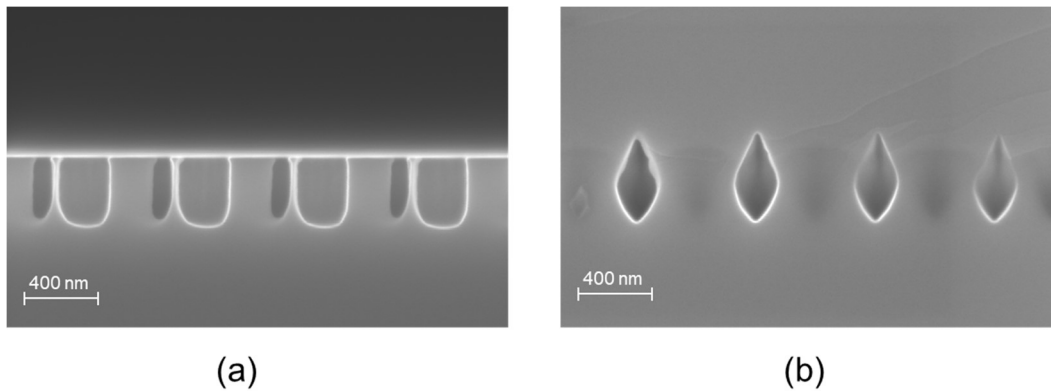
Figure 4-15 Cross-section SEM images of the triangular airhole PC cavity (a) before regrowth; and (b) after regrowth

4.4.3 Triangular Airhole PCSEL Fabrication

As observed in LaserMOD simulations summarized in section 3.3.3, disk shaped contact proves to be the ideal p-metal contact design for efficient and uniform charge injection into the MQWs active region instead of a ring structure. However, this disk-shaped metal hinders the surface normal laser emission from the p-side. Therefore, the emission should be collected from the substrate side. The next fabrication process is modified with a square p-metal contact and epi-down design for collection of laser emission. The thickness of the p-GaAs is also optimized as discussed in section 2.6.3 to maximize the extraction efficiency.

After the regrowth process, 10 mm x 10 mm sample wafer surface is thoroughly checked using microscope to make sure there are not defects or dirt on the surface. Later, the sample is dipped in acetone and sonicated for 10 minutes followed by another 10 minutes of sonication in IPA. N_2 gas is blown to dry the sample and sample is loaded into O_2 plasma ashing process to burn out any organic residues on the surface.Later, NR9 1500 PY negative tone photoresist is spin coated and standard photolithography process is carried out to deposit 200 μm x 200 μm p-electrode with Pd/Ti/Pd/Au metal stack using CHA solution e-beam evaporator as shown in Figure 4-16(d).

Extreme care is taken to avoid any native oxides between the p-GaAs contact layer and p-metal stack that increase the series resistance. A 3.5 μm p-mesa is etched using wet etching process by dipping the sample in H_3PO_4:H_2O_2:H_2O solution of 1:1:10 ratio for 300 sec to isolate the individual PCSEL devices in the 8x8 array. Clean and smooth surface is achieved after the wet etching process with isolated device mesas. The substrate is then polished using Ultrapol polishing tool with 0.5 μm polish sheet to achieve mirror surface. The polishing time depends on the required smoothness of GaAs backside substrate.

64

Higher the smoothness with reflective surface, the scattering losses for the emission from back side through substrate would be less.

The n-metal stack of Ni/Ge/Au/Ti/Au is deposited on the back side polished substrate by using NR9 3000 PY negative tone photoresist and standard photolithography process and annealed at 400 °C for 60 seconds in the presence of N_2 gas by using JetFirst RTA tool. Under such annealing conditions, the metal dopants can diffuse into the semiconductor to form a low resistance ohmic contact. The emission region is mainly controlled by the p-metal contact size as it is closer to the active region around 2 µm compared to the n-metal which is 300 µm away. Thicker substrate helps in efficient lateral charge distribution for such large emitter sizes.

(a) Epitaxial growth   (b) Photonic crystal fab   (c) Regrowth   (d) P-metal and p-mesa

(e) Substrate removal   (f) Flip-chip bonding   (g) N-metal deposition   (h) Wire bonding and Testing
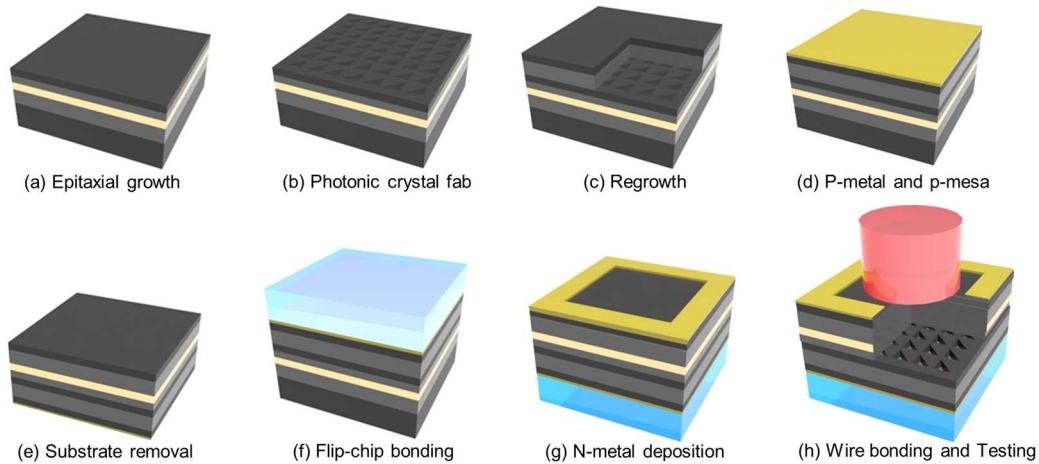
Figure 4-16 Schematic of the PCSEL p-disk electrode design fabrication process (a) initial epitaxial growth; (b) patterning of photonic crystal cavity; (c) AlGaAs and GaAs regrowth process using MOCVD; (d) p-disk electrode deposition using e-beam evaporator; (e) p-mesa etching and substrate removal process; (f) flip-chip bonding process using indium bumps; (g) n-ring metal deposition on the backside using e-beam evaporator; and (h) wire bonding for electro-optical characterization

PCSEL are operated at high current injection levels of a few Amperes, therefore thick interconnect metals are required to accommodation efficient carrier injections. After the annealing process, thick interconnect metal stack of Ti/Al/Ti/Au is deposited on the n-metal contact which is on the backside of the device. Now on the front side (epi-side), 500 nm of thick silicon dioxide layer is deposited by using plasma enhanced chemical vapor deposition (PECVD) process to conceal the MQWs exposed region.

To access the individual PCSEL devices, the silicon dioxide layer is etched away at the p-metal region through open-hole process that uses the dry reactive ion etching process to etch silicon dioxide layer. To make sure the oxide layer is properly removed, I-V tests are done. The p-probe connected to the p-metal and n-probe is connected to the backside n-interconnects to measure the laser diode characteristics.

In the next step, 3 μm thick indium bumps are deposited in the open hole region by using NR 9 3000 PY negative tone photoresist and standard photolithography process. The main reason to deposit indium is to accommodate flip-chip bonding process between 10 mm x 10 mm GaAs sample and 20 mm x 20 mm Silicon fan-out interconnect chip. Indium is a soft metal with low melting points and helps in electrical conduction and strong adhesion. Detailed explanation of flip-chip bonding process between GaAs and Si samples is explained in section 3.4.

4.4.4 Flip-Chip Bonding Process

PCSEL are operated at very high currents and results in a few tens of Watts of thermal power. As a result, the MQWs active region and PC layer junction temperature spikes during the operation due to low thermal conductivity of GaAs around 50 $Wm^{-1}K^{-1}$. This may cause device failure or thermally limited optoelectronic performance. Therefore,

efficient thermal management scheme should be designed and implemented for PCSEL testing and operation.

One of the key processes is the bonding of PCSEL on a submount for heat-dissipation and electrical current injection. Indium bump-based flip-chip bonding process is developed to dissipate the heat from the GaAs PCSEL junction with efficient bulk Si fan-out interconnects chip whose thermal conductivity is around 150 $Wm^{-1}K^{-1}$. The GaAs PCSEL devices are flipped and bonded to Si substrates through micro scale indium bumps.

In parallel to 10 mm x 10 mm PCSEL sample, a 20 mm x 20 mm silicon fan-out interconnect sample is also processed. Initially thick interconnect metal stack of Ti/Al/Ti/Au is deposited using NR 9 3000 PY photoresist and standard photolithography process. These interconnect lines are 5 mm to 8 mm long and are buried under 500 nm thick silicon dioxide layer deposited using PECVD process. The main reason to deposit oxide layer is to conceal the interconnect lines and avoid shorting with the adjacent ones when indium squeezes out during the flip-chip bonding process.
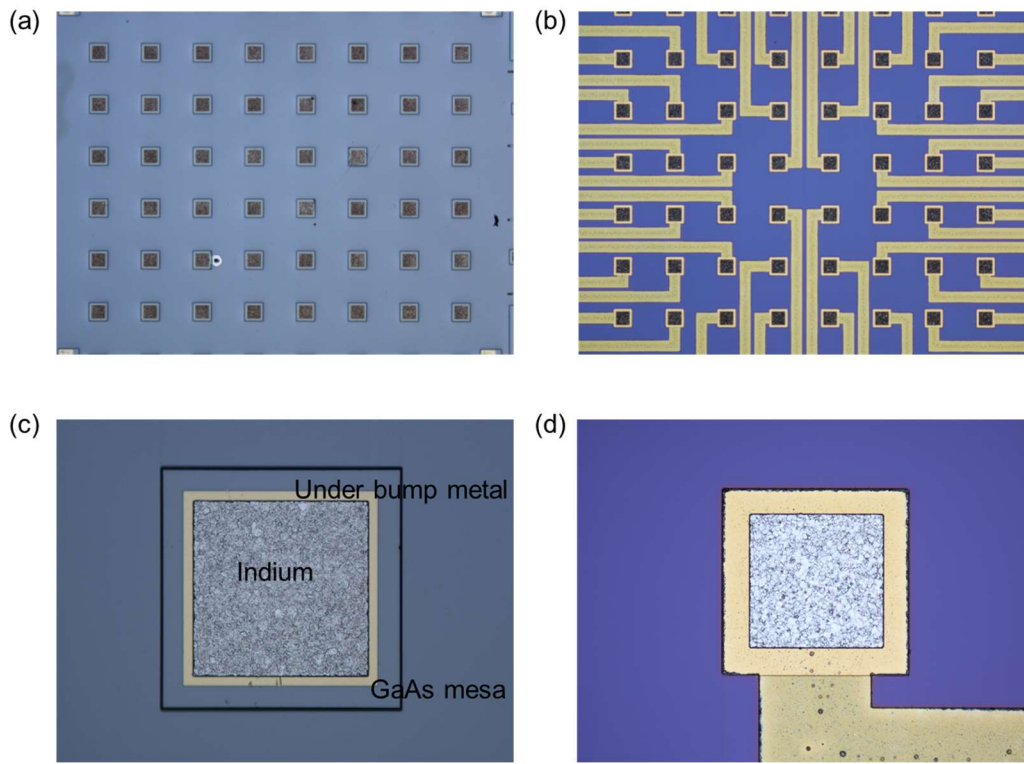
Figure 4-17 Micrograph images of (a) PCSEL chip with 8x8 array; (b) Si fan-out chip with 8x8 array interconnect pads; (c) one PCSEL device showing under bump metal and indium bump; (d) one interconnect pad with openhole and indium bump before flip-chip bonding

The oxide layer is etched away using dry reactive ion etching process at the probe pad and device locations to provide access for probing. We use sccm of CF_6 gas in the presence of sccm of He to etch the silicon dioxide layer in Trion Minilock etcher at UTA. Once the open hole process is completed, at the device region 3 μm thick indium is deposited using photolithography process. This forms a total of 6 μm thick indium on GaAs PCSEL sample and Si fan-out sample together that improves the flip-chip bonding adhesion as shown in Figure 4-17.
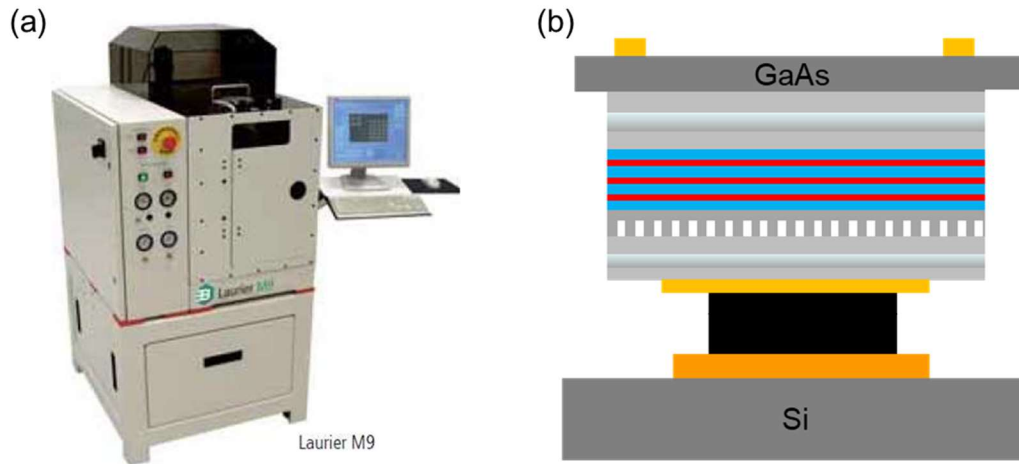
Figure 4-18 (a) Laurier M9 flip-chip bonder at UTA; (b) schematic of the GaAs PCSEL chip and Si fan-out chip integrated using indium bump flip-chip bonding process

This integration mechanism not only improves the thermal stability of PCSEL during high power operation, but also enhances the uniform charge injection through large area p-metal contact in the photonic crystal region. As shown in Figure 4-17,10 mm x 10 mm GaAs sample has 8x8 array of PCSEL devices each with 200 µm x 200 µm photonic crystal cavity. The Si wafer is also processed to have an array of 8x8 indium bumps with under bump metallization (UBM). Each individual PCSEL device is interconnected to a probepad for electrical injection as shown in Figure 4-17(d). The schematic of the integrated GaAs/Si package after the bonding is shown in Figure 4-18(b). The generated laser is emitted out through the flipped GaAs substrate.

The GaAs/Si integration is carried out using Laurier M9 flip chip bonder at UTA shown in Figure 4-18(a). Multiple calibration runs are evaluated to develop the correct recipe for indium bump bonding process. 3 µm thick indium is deposited on both GaAs PCSEL devices and Si UBM pads to provide strong adhesion. Laurier M9 bonder is equipped with a beam-splitter camera to accommodate multi-point alignment to achieve

post bond alignment accuracy of 0.5 µm. Strong bonding between GaAs and Si wafers is achieved at bond temperature 200 °C and uniform pressure of 500 grams is applied for 300 seconds. Shown in Figure 4-19(a) are the upper and lower chucks temperature and pressure profiles during the flip-chip bonding process optimized for 10 mm x 10 mm PCSEL device on Laurier M9 tool. The I-V performance before flip-chip bonding after integrating GaAs/Si chip are measured as shown in Figure 4-19(b). Note the current limit was set to 100 mA while testing the I-V characteristics before flip-chip bonding to avoid burning of devices at high current as the metal contact was thin. It is observed that I-V characteristics of PCSEL device have improved after the flip-chip bonding. This confirms the low resistance electrical connection between the PCSEL device and Silicon fan-out interconnect chip.
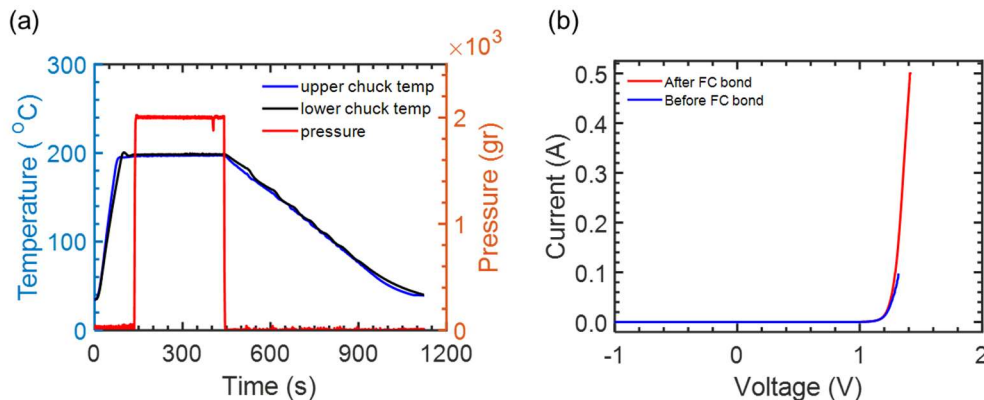
Figure 4-19 (a) Upper and lower chucks temperature and pressure profiles during flip-chip bonding process on Laurier M9 tool; and (b) I-V characteristics measured before and after flip-chip bonding. Note the current limit was set to 100 mA while testing the I-V characteristics before flip-chip bonding to avoid burning of devices at high current as the metal contact was thin.

After the bonding, the GaAs/Si chip is subjected to ultrasonication test for 60 seconds and spinning test at 5000 rpm for 60 seconds and hot plate test at 150 °C for 60 seconds to check the bond strength. The indium bonding successfully survived all the tests.

The Micrographs of the separated samples in the destructive test revealed the uniformity of boding among different PCSEL devices and no overflow of indium is observed.
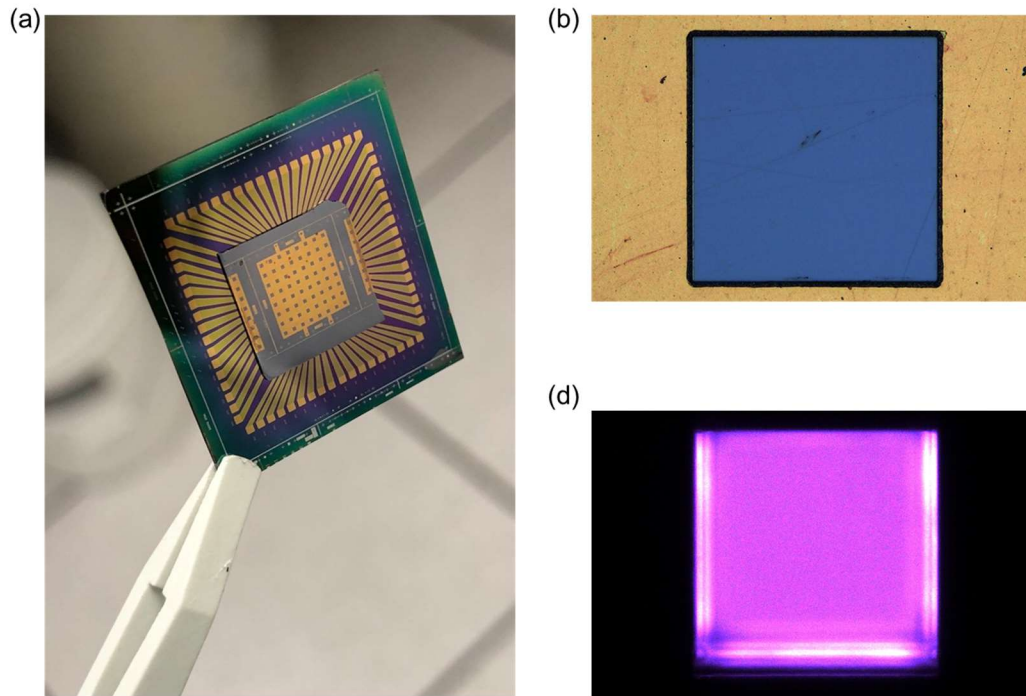
Figure 4-20 (a) Image showing the integrated PCSEL/Si package after flip-chip bonding; (b) micrograph of backside n-metal ring with emission window; and (c) Micrograph image captured from the backside emission showing uniform charge injection and emission profile

Chapter 5

MEASUREMENT AND LASING CHARACTERISTICS

5.1 Micro-Photoluminescence (µPL) Measurement

To characterize the optical properties of the PCSEL devices a dedicated micro-photoluminescence set up is developed to focus the optical pump source on the micro patterns and collect the response signal from the devices for optical analysis. Optical characterization of PCSEL devices is crucial before proceeding into electrical fabrication. The wavelength location of resonant modes, probable lasing mode and respective Q values can be evaluated using the optical characterization.

Another advantage of the optical characterization is that heating issues that are predominant in the electrical injection process can be eliminated. In addition, non-uniformity in charge distribution due to current crowding can be also eliminated by adjusting the size of the uniform circular laser beam spot on the PC pattern region. Size dependent optical characteristics of the devices can also be evaluated by using the optical test set up.

As shown in Figure 5-1, the optical characterization set up developed for the PCSEL consists of high power laser source for optical pumping, series of optics for beam expansion, low and high pass filters to select the required frequency components, power meter to track the incident power on to the sample, narrow numerical aperture (NA) objective lens to avoid collection of side or angular emission from PCSEL response single, a XYZ 3-diemsional (3D) stage for micro adjustment of the sample location with respective optical beam, high resolution camera to view the alignment of PC patterns and laser beam spots, white light source for illumination, and high resolution monochromator for spectral analysis of the PC response. The incident and collected signals go through a series of beam splitters to distribute the signal accordingly.
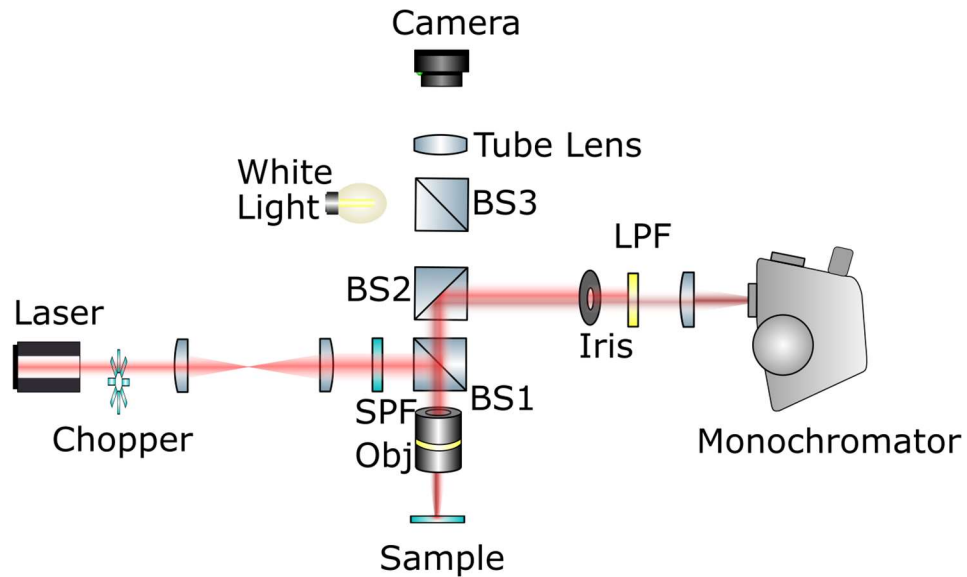
Figure 5-1 Schematic of the micro-photoluminescence optical measurement set up developed for the measurement of PCSELs before and after regrowth. Note SPF: short pass filter, BS1: 50-50 beam splitter, BS2: 90-10 beam splitter, BS3: 50-50 beam splitter and LPF: low pass filter

The PCSEL structure is optically pumped using Arrayo Instruments 680 nm high power laser diode source, that is mounted on thermo-electric cooler (TEC) mount to maintain constant peak wavelength. The emission from laser source is fiber coupled into the µPL set up. Mitutoyo 10x objective lens with 0.26 NA is used to focus the laser beam spot on the sample. The measured beam spot size on the sample is circular with 100 µm diameter. Uniform laser beam spot is required to accurately evaluate the optical and modal characteristics of the PC cavity. The variation in the size of the laser beam spot would also change the threshold conditions of PCSEL device. Therefore, the optimum laser spot with good emission intensity is found to be 100 µm.

The laser emission from the sample is collected using the same objective lens and coupled into the TRIAX 320 monochromator that has thermo-electric cooled InGaAs detector which is highly sensitive in 1 µm wavelength. Highly efficient gold-plated mirror gratings with 300 groves/nm density with blaze at 1 µm wavelength are used to achieve spectral resolution of 0.1 nm. A chopper and Stanford Model 8000 lock-in amplifier are used for the spectral acquisition of emission and analysis. In addition, an iris is used in between the objective lens and monochromator for the control of the emission light. All the tests were carried in CW and at room temperature for both before and after regrowth conditions.
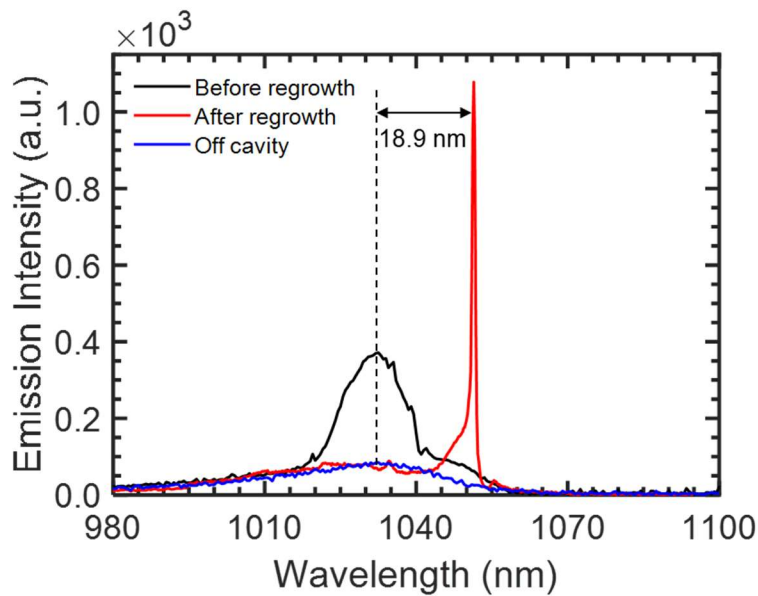
Figure 5-2 Measured optically pumped spectra of the triangular airhole PCSEL before regrowth on PC region (black), after regrowth on PC region (red) and off PC region (blue)

Figure 5-2 shows the optical pumping results immediately after PC cavity etching and after regrowth on the triangular airhole PC pattern with lattice constant of 311 nm, airhole side length of 273 nm and PC etch depth of 265 nm. The measured spectrum (black

74

curve) shows a resonant mode peak at 1037.5 nm that matches well with the peak wavelength of the gain spectrum or off cavity PL (blue curve). The four modes observed in the COMSOL have low Q values before the regrowth, the full-width half maximum (FWHM) before the regrowth is around 15 nm which is mainly due to merging of all the modes and shown a single low-Q mode.

The optical pumping spectrum after the regrowth process (red curve) is also measured under same test conditions. The dominant mode wavelength location and their respective peak emission intensities are compared. The dominant resonant mode observed at 1037.5 nm before regrowth on triangular PC cavity, shifted by 18.9 nm and located at 1056.4 nm with narrow FWHM of 0.5 nm after the regrowth. The narrowing of the dominant peak is due to the refilling of the airhole with the AlGaAs material during the regrowth process that reduces the size of the airhole embedded inside. As discussed in chapter 3, reduction in airhole size increases the Q-values and made the dominant mode to be narrow with FWHM of 0.5 nm after regrowth compared to before regrowth. But reducing the airhole size also results in red shift as observed, the 18.9 nm red shift in dominant mode is due to refilling of airhole.

The Q values are comparatively high after the regrowth providing favorable conditions for lasing. However, the 18.9 nm red shift moved the dominant lasing mode away from the peak photoluminescence (gain peak of active region) resulting in higher threshold current values than predicted. The electrically injection process induces heating in CW operation and red shifts the QWs PL peak a few nm closer to resonant mode, but the dominant mode would be still away from PL peak.

5.2 Pre-compensation of PC Lattice for Airhole Refilling

The wavelength of the resonant mode in PCSEL is mainly dependent on the lattice constant of the PC cavity. By reducing the lattice constant a value to 309 nm from 311 nm, the resonant mode is blue shifted by 7.54 nm and the dominant mode before the regrowth on triangular airhole PC is now located at 1027.6 nm which is on blue side of the PL peak as shown in Figure 5-3. After the regrowth, as expected the airhole size shrinks and the dominant lasing mode is located at 1044.9 nm which is around 10 nm away from the PL peak on the red side. The lattice constant can be further reduced to blue shift the the resonant mode to match the PL peak exactly with less than 2 nm offset. The thermal gradient generated in the electrical injection red shifts the PL peak of the MQW active to a few nm, therefore, 10 nm of buffer seems to be optimum to accommodate the red shift in PL peak at high current PCSEL operation. This pre-compensation of lattice constant for the reduction of airhole size due to AlGaAs refilling would reduce the current threshold and increase the slope-efficiency.
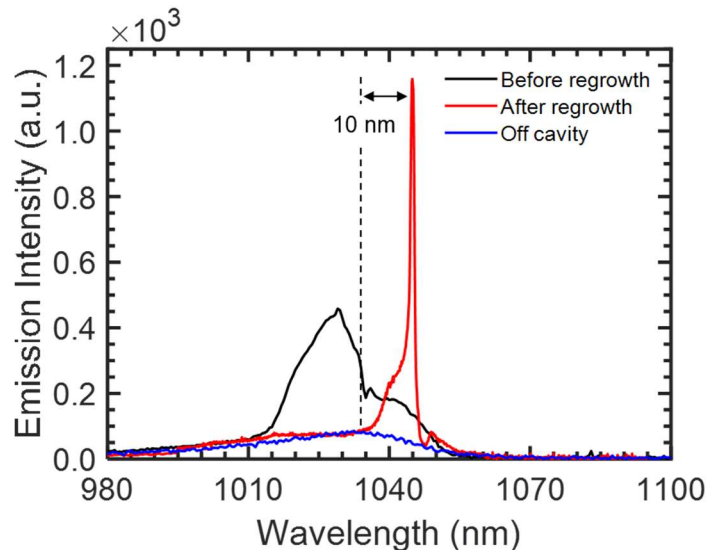
Figure 5-3 Measured optically pumped spectra of the triangular airhole PCSEL with pre-compensated lattice constant before regrowth on PC region (black), after regrowth on PC region (red) and off PC region (blue)

5.3 L-I-V and Spectral Characteristics

After confirming the resonant characteristics of the PCSEL pattern in the optical pumping tests, the electrical fabrication process is initiated. Thick interconnect metals are deposited, and substrate is polished to collect emission from the backside when the PCSEL is flip-chip bonded to silicon fan-out chip as described in section 3.3.4. The completely fabricated PCSEL device is electrically tested under pulsed and CW operation conditions to measure the emitted power and electroluminescence spectral characteristics.

5.3.1 Pulsed Operation

For the pulsed operation the PCSEL device is mounted on Cascade Microtech MPS 150 model probe station, that is equipped with two Formfactor DPP210 electrical probes of 50 µm diameter. The positive probe is connected to the silicon interconnect line and the negative probe is connected to interconnects on the backside of the PCSEL substrate. The PCSEL device is electrically injected at room temperature using Newport LDP 3830 precision pulsed current source that can generate continuous pulses of 1 µs pulse width with 1% duty cycle and pulse repetition rate is 10 kHz.

The optical power of the laser emitted from the back side of the PCSEL is measured using Newport Model 1830-C optical power meter that is connected to Model 818-SL silicon detector head with 11.3 mm diameter sensor which is placed just in front of the PCSEL emission window. 900 mW of output optical power is achieved from a single PCSEL emitter with a single-lobed narrow beam. The maximum output power is instrumentally limited by the laser diode driver Newport LDP 3830. As shown in **Error! Reference source not found.**(a), the threshold current I_{th} is observed to be 210 mA and slope efficiency η_{slope} is 0.36 WA^{-1}.
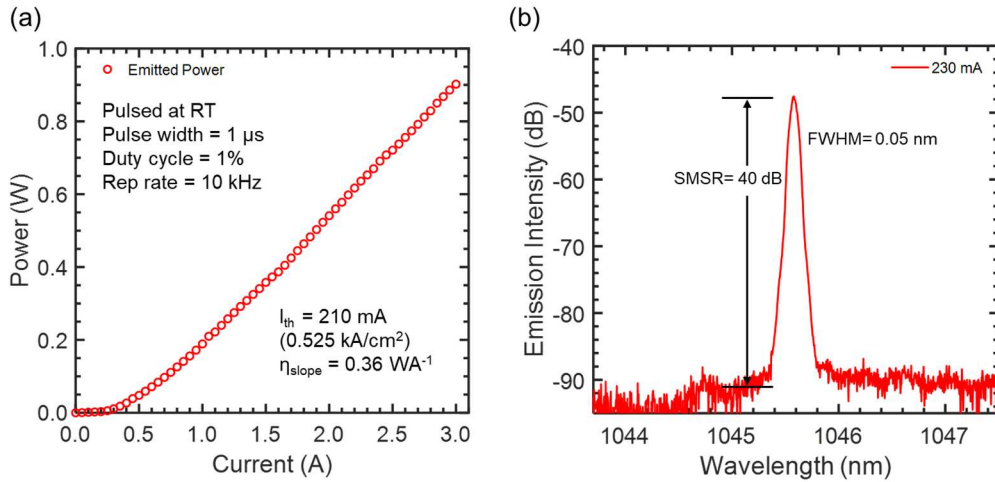
Figure 5-4 Electrically pumped triangular airhole PCSEL under pulsed operation (a) L-I curve showing threshold of 210 mA; and (b) spectra above threshold showing >40 dB side mode suppression ratio and full width half maximum of 0.05 nm

The lasing spectrum measured around 230 mA through a 50 μm core multi-mode fiber coupled into Yokogawa AQ6370B optical spectrum analyzer indicated a single dominant peak with side mode suppression ratio (SMSR) of >40 dB confirming single mode operation. The peak wavelength λ_{peak} is 1045.58 nm and full-width half maximum (FWHM) of the peak is less than 0.05 nm as observed in **Error! Reference source not found.**.

As observed from the power dependent spectral characteristics, at 210 mA mode B started to lase with dominant peak at 1045.58 nm. This is in good agreement with the COMSOL simulations summarized in chapter 3 where mode B has the lowest gain-threshold of 49.62 cm^{-1}. At 250 mA current injection, another peak started on the red side of mode B at 1046.63 nm, it is mode A with next lowest gain-threshold value of 78.88 cm^{-1} as shown in Table 3-2. The other two modes C and D are two low-Q peaks at 1043.06 and 1042.71 nm, respectively. Both of them have high gain-threshold values of 349.25 cm^{-1} and 1268.17 cm^{-1}, so they did not lase even at 10x I_{th} current injection.
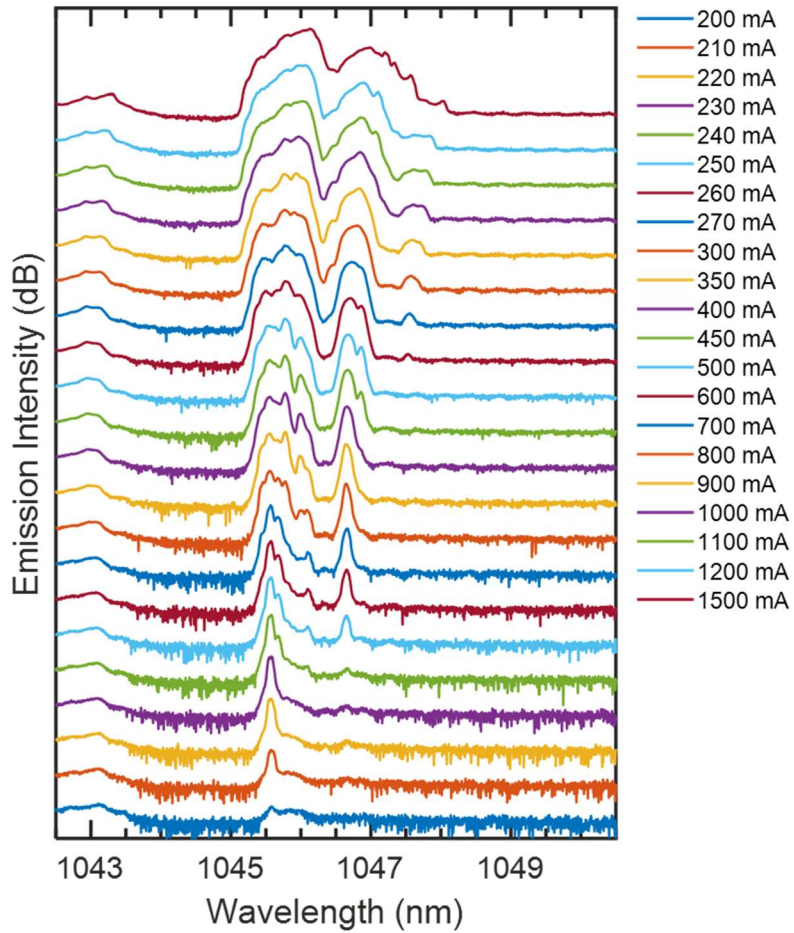
Figure 5-5 Electrically pumped PCSEL spectra at different current injection levels under pulsed operation

5.3.2 CW Operation

For the CW operation, the PCSEL device is connected to Keithley Model 2612 current source. Similar to pulsed operation, the device is mounted on Cascade Microtech MPS 150 model probe station. The emitted power is coupled into Model 818-SL silicon detector head. A maximum CW output power of 100 mW at 1.5 A is observed which is

limited by the instrument. As shown in **Error! Reference source not found.**(a), the threshold current I_{th} is 300 mA and slope efficiency η_{slope} is 100 mWA^{-1} in the CW operation.

The emission from the PCSEL window is collected using a 50 µm multi-mode fiber and coupled into optical spectrum analyzer. The lasing spectrum measured at 500 mA is also single mode with SMSR of 30 dB. The peak wavelength is 1055.34 nm which is red shifted compared to pulsed peak wavelength is due to thermal issues and FWHM is 0.1 nm as shown in **Error! Reference source not found.**(b).
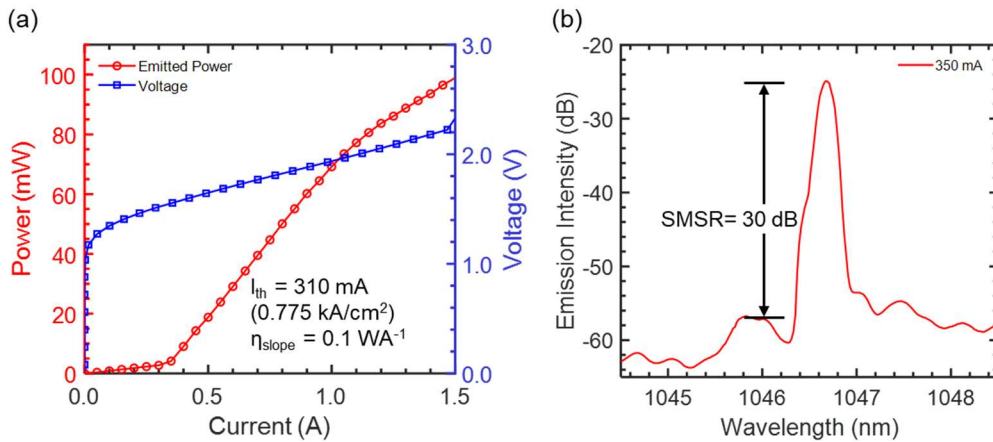
Figure 5-6 Electrically pumped triangular airhole PCSEL under c.w. operation (a) L-I-V curve showing threshold of 310 mA and slope efficiency of 100mWA^{-1}; and (b) spectra above threshold showing 30 dB SMSR and FWHM of 0.1 nm

The near field emission images captured from the backside of the substrate through n-electrode window at different pump current levels show uniform charge diffusion that is achieved by employing the uniform p-disk electrode as shown in Figure 5-7, unlike the p-ring electrode that triggered current crowding and non-uniform emission.
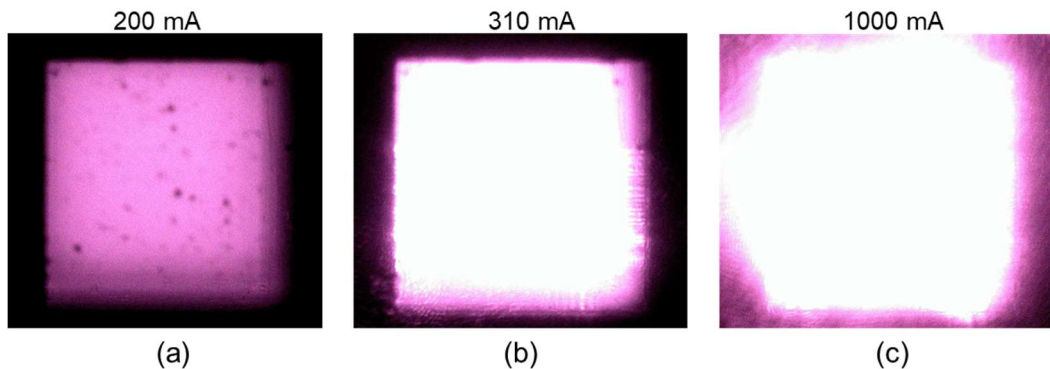
Figure 5-7 Near field radiation images showing uniformity in emission throughout 200 μm x 200 μm PCSEL emitter captured from the backside through substrate at different pump currents (a) below threshold at 200 mA; (b) on the threshold at 310 mA; and (c) above threshold at 1000 mA

Note the PCSEL device is operated at room temperature without any thermal management. This results in high temperature gradience in the MQW region and reduces the peak gain. As observed in the **Error! Reference source not found.**(a) L-I-V plot, the emitted output power started to saturate from 1 A, this is mainly due to high thermal impact on gain region. This is in agreement with the gain medium simulations at different temperature conditions using LaserMOD summarized in section. Therefore, the maximum power emitted in the CW operation is thermally limited and requires active thermal management.

Error! Reference source not found. shows spectral characteristics of the PCSEL measured in optical spectrum analyzer at different pump currents. Beyond 600 mA current injection the emission turned out to have multi-mode as observed in the spectral plot. This is due to low gain threshold difference between mode A and mode B as summarized in section modal characteristics.
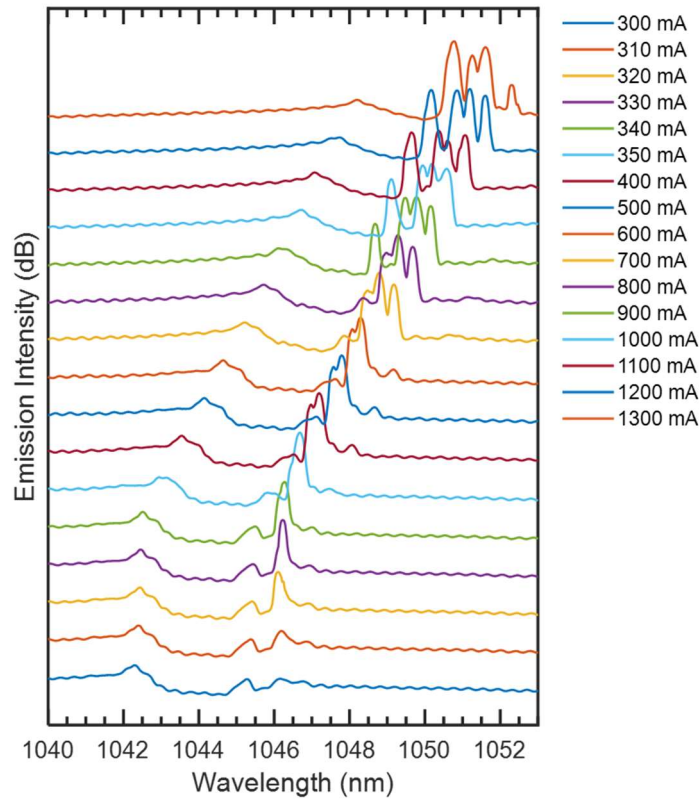
Figure 5-8 Electrically pumped PCSEL spectra at different current injection levels under c.w. operation showing significant red shift in the spectra at higher current injection levels due to thermal impact

At higher current injection, mode A also reach gain threshold condition and starts to lase turning the emission to be multi-mode. This multi-mode emission can be further improved by increasing the gain threshold for mode A. Detailed investigations on PC cavity designs and engineering approach to counter the multi-mode emission at high current operations is explained in section 5.1 and novel techniques are recommended.

5.4 Thermal Management for PCSELs in CW Operation

As observed from the previous experimental results, the impact of temperature gradience on PC cavity and lasing characteristics due to high current injection is significant. In pulsed operation, the wavelength of the lasing mode is almost unchanged at high current levels. This is primarily due to smaller pulse width of 1 µs and low duty cycle of 1%. However, as compared to CW operation, the output power was dramatically limited and large red shift is observed in the lasing mode spectral characteristics.

As predicted the PCSEL/Si flip-chip bonding is instrumental in thermal management in addition to uniform charge injection. But at higher current inject levels the thermal conductivity of Si is not sufficient to dissipate the joule heating. Detailed thermal simulations on Ansys Icepak software are carried out on PCSEL/Si indium bump flip-chip package to study the temperature gradient in the QWs due to heat generated in CW operation as shown in the Figure 5-9. The laser emitter is modeled as plane heat source with the thermal power calculated based on the wall-plug efficiency of the PCSEL device [57]. The package is placed on a copper base that acts as heat sink at 20 °C. All the simulations are carried out at room temperature.
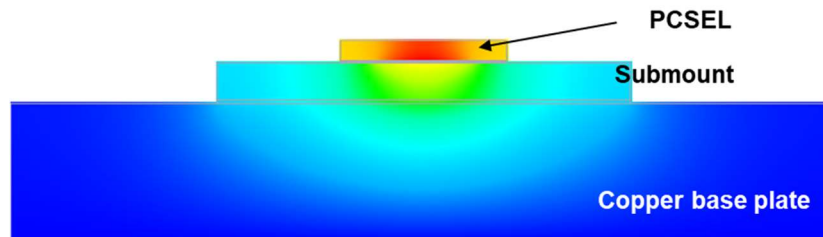
Figure 5-9 Si/PCSEL flip-chip bonded model developed in Ansys Icepak

The hot spots are located in the QWs region and peak temperature of 118 °C is observed for thermal power of 30 W when PCSEL device is mounted on Silicon fanout chip. On the other hand, temperature rise of 43 °C in QWs region is observed when PCSEL is mounted on CVD diamond whose thermal conductivity is around 2200 Wm^{-1}K^{-1} shown in

.

(a)   (b)
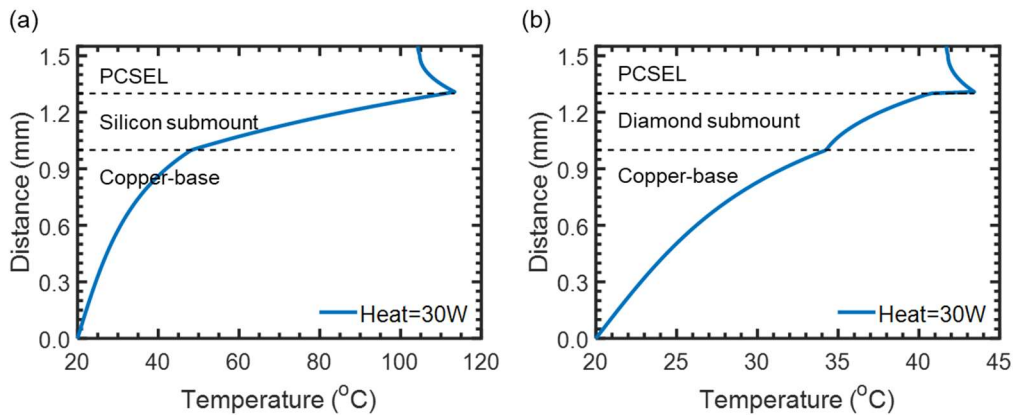
Figure 5-10 Simulated temperature profile in the PCSEL device and submount package when mounted on (a) Silicon; and (b) CVD diamond

For a 200 μm PCSEL operated at 3 A of current, the heating power is around 5 W based on wall-plug efficiency. This creates a temperature drift of more than 15 °C in PCSEL device when mounted on Silicon and operated under CW condition as shown in Figure 5-11. Such a high temperature in the QWs region degrades the gain and triggers non-radiative recombination. This increases the threshold current of the device and reduces the slope efficiency. In addition, the temperature gradience in the PC region impact the modal characteristics by altering the refractive index. The resonance modes are red shifted and Q-values are degraded at high current operation, in addition to thermal lensing.
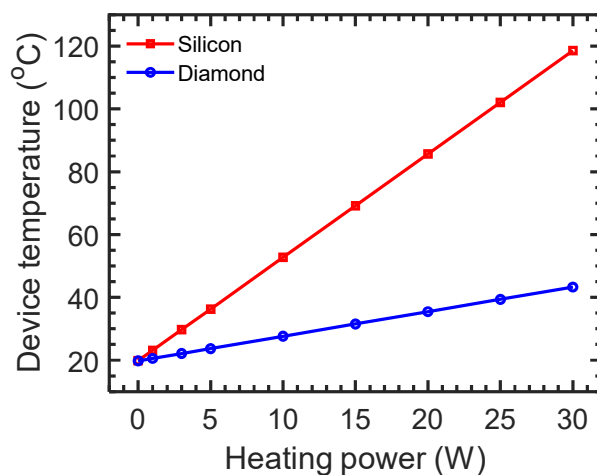
Figure 5-11 Simulated peak temperature rise in PCSEL QWs region at different heating powers when mounted on Silicon and Diamond submounts

5.3 Discussion and Analysis

The L-I-V characteristics reported here reveals the high output power levels upto Watts class can be achieved by a single triangular airhole PCSEL emitter. Unlike the wafer bonding technique employed by others for demonstration of PCSEL devices, epitaxial regrowth by MOCVD process was used. Molecular beam epitaxy (MBE) process is another approach for regrowth; however, it also offers challenges in reducing the defect densities on the surface after the regrowth. In wafer bonding techniques high series resistance and re-absorption of laser emission occurs due to the high density of defects at bonded interfaces and causes serious deterioration of opto-electrical properties. In addition, though defect free PC cavities are processed, defects from wafer bonding introduces non uniformity in airholes and increases the intrinsic loss in the PC cavity. MOCVD process proves to be a promising approach to reduce the defect density at the interfaces, planarizes the sample surface and safely preserves the airholes in the PC cavity. This enhances high output powers in PCSELs processed using MOCVD technique.

85

The triangular airhole shape is another factor that is responsible for high output power. As discussed in earlier sections, the circular airholes PC cavities offer good modal characteristics, however due to the symmetry preserved in the circular airholes, the vertical emission in the direction normal to the PC surface is reduced due to destructive interference between Bragg's first order diffraction of oppositely propagating waves in the PC surface plane. This results in infinite vertical Q values and the emission is highly reduced. By using triangular holes, the symmetry is broken, and the vertical emission is constructively interfered by the opposite travelling waves in the plane of PC. This helps in extracting more power in the surface normal direction.
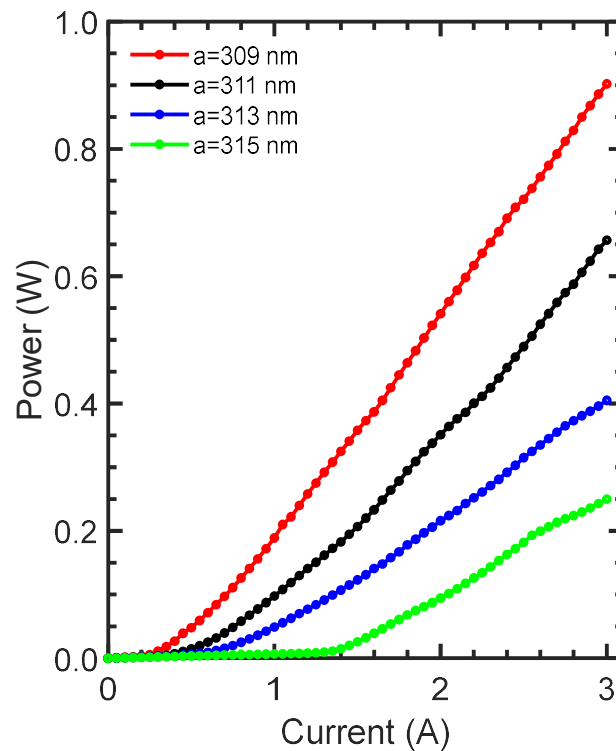
Figure 5-12 L-I curves of different triangular airhole PCSEL devices with lattice constant a varying from 309 nm to 315 nm under pulsed operation

The third factor contributing for high power levels is the pre-compensation of lattice constant to blue shift the resonant mode close to the MQW PL peak. This provides more gain to the resonant mode, reduces the current threshold value, increases output power and slope-efficiency as shown in Figure 5-12 with different lattice constants from 309 nm to 315 nm.

Another important factor is the epi-down design and collection of emission from the backside through the substrate. This enables the reflection of downward emitted power to upwards with the help of gold reflector or DBR structures. By optimizing the thickness of p+ GaAs layer, constructive interference can be achieved between the vertical upward and downward reflected waves and increases extraction efficiency. This approach almost doubles the power levels that are observed in epi-up design that uses double ring design. Another advantage of epi-down design is the p-disk metal electrode for uniform charge diffusion. This avoids current crowding and thus reduces series resistance for efficient charge injection.

The indium bump flip-chip bonding technique enables the GaAs/Si packaging in epi-down design. Thermal conductivity of Si is three times higher than GaAs and helpful in heat dissipation from the QW region. However, as the device size increases the thermal power also increases at high current operation and results in thermal limited emitted power as observed in L-I and spectral characteristics in the CW operation of PCSEL device bonded to Si base. This indicates that higher thermal conductive submounts like diamond ($2200 \ Wm^{-1}K^{-1}$) are required for flip-chip bonding and packaging of PCSEL devices in the future to demonstrate high power larger emitters.

The multi-mode emission observed in the spectrum at high current operation is due to less gain-threshold difference between transverse modes. The PC cavity designs can be modified to suppress the transverse and longitudinal modes other than lasing mode to increase the single mode emission regime even at high current operations. These modifications can be evaluated, and maximum single mode emission device size is estimated using the Q-k relation of multiple transverse modes.

Chapter 6

Q-k ENGINEERING FOR LARGE AREA SINGLE MODE EMISSION PCSELS

To achieve large area single mode lasing, it is critically important to design the PC cavity such that only one mode is favorable for lasing. In particular, the quality-factor of the lasing mode is investigated as a function of in-plane momentum (Q-k relation). Such Q-k relation determines the scaling of single-mode PCSEL [58]. Further a possible route to engineer the Q-k relation based on symmetry breaking is developed to estimate the maximum single mode emission single of the PCSEL.

6.1 Gain Threshold Discrimination for Higher Order Modes

Engineering the photonic band structure has led to significant advances in the development of optoelectronic devices [41]. Most band structure engineering focuses on the eigenfrequency of the modes as a function of the wavevector. Recently, engineering the Q-k relation has drawn increasing interests due to a number of applications such as light-trapping, two-dimensional lasing, and meta optics [9], [59]–[63].

One of the desired features in such engineering is to obtain a fully controllable finite and narrow high-Q peak. This allows the devices to interact with the electromagnetic waves only at a certain angle and frequency. This feature is also useful in achieving single-mode large-area lasing for high-power applications. Such devices have always been challenging to realize since as the device-size scales, the spacing between the modes in the wavevector space reduces, leading to a diminishing Q-difference and, hence, threshold-difference [29], [64]–[66].

Consider a generic condition to achieve a peaked Q value in an optical resonators with a light incident or output in the out-of-plane direction, with $k = (k_x, k_y)$ representing the

2D in-plane wavevector. The goal is to obtain a peaked Q as a function of the angles for a uniform dielectric slab, which can be found in VCSELs. There are Fabry-Pérot resonances in the vertical direction in the slab. Their Q-factors as a function of the wave incident angle are nearly constant near the normal direction.

This can be improved by introducing a 2D photonic crystal in the slab, as illustrated in. Here, the modes at the non-zero angles have a lower Q than the mode at the normal direction, i.e., the Brillouin zone center Γ. When used in a PCSEL, the mode at Γ would exhibit a lower threshold than other modes. This is in accordance with the recent success of PCSELs, where single-mode lasing is maintained in a much larger area compared to the VCSELs. Such a peaked Q(k) function can be viewed as a result of a quasi-bound states in the continuum (quasi-BIC) [67].
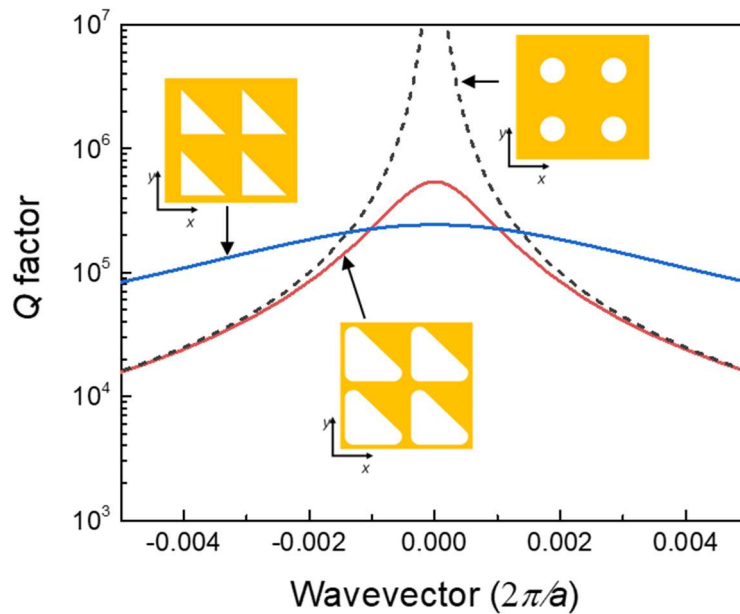
Figure 6-1 The *Q* factor as a function of in-plane wave vector *k* for three different hole shapes, i.e. circular (black), triangle (blue), and a deformed triangle (red).

Given the above analysis, it is of importance to engineer the Q-k relation to pursue single-mode lasing in a larger device. Consider an approach based on symmetry-breaking in the plane of PC surface. It is known that if the PCSEL preserves the C_{4v} symmetry, a singly degenerate mode at Γ becomes a bound-states-in-the-continuum (BIC). An example is shown in (black dashed curve), where we assumed circular holes in the PCSEL. It is observed that the Q factor of the mode at the Γ point becomes infinite. Such a mode at the Γ point will not emit light in the vertical direction, thus can't be used for surface emission in a PCSEL structure. The PCSEL structure with a triangular-shaped hole breaks the C_{4v} symmetry and can form a laser at Γ, yet the Q-k function is relatively flat, as shown in the blue curve Figure 6-1. To increase the Q-factor contrast between the 0th order and 1st high-order modes, consider a deformed triangle hole, also shown in the inset of Figure 6-1. In practice, such deformations occur naturally in device processing, and the degree of the deformation can be further controlled by designing different masks in lithography. The deformation brings the triangle shape closer to the circular shape. As a result, the Q-k curve becomes peaked at Γ, yet the quality factor at Γ point remains finite. The end-result is the Q-factor contrast between the fundamental mode and the first-order modes is larger compared to that of the original triangle hole shape, which can lead to single-mode emission up to a device emitter size of 400 μm as the gain threshold difference between 0th mode and 1st order modes is reduced drastically below 1 cm^{-1} beyond 400 μm device size as shown in. These results match well with the experimental results reported by Noda *et. al* [9], [29].
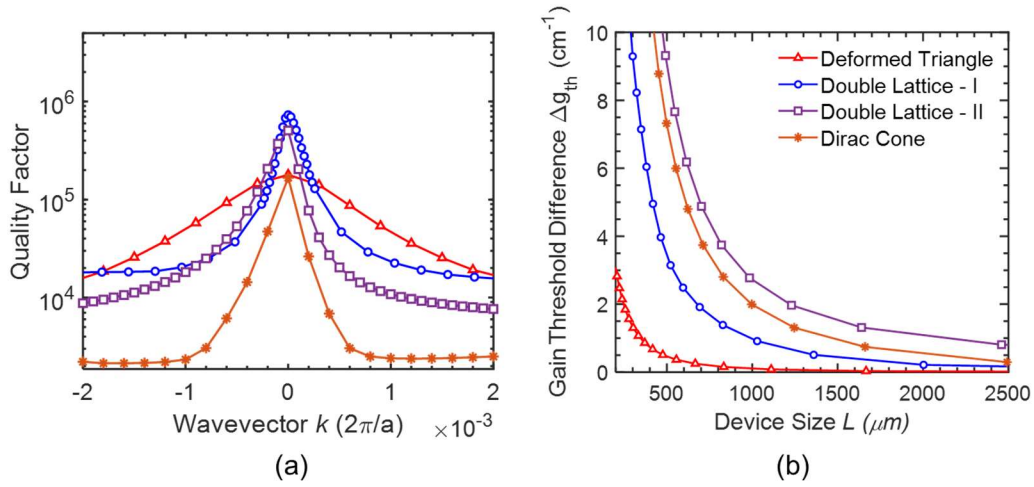
Figure 6-2 (a) *Q-k* function; (b) Δg_{th}-*L* (gain threshold difference vs device size) plots of deformed triangular airhole, double lattice designs and Dirac-cone with circular airhole.

Similarly, by using the Dirac-cone band structure [58] finite high Q-factor and narrow Q-k curve with larger Q-factor discrimination between the 0th order mode and the 1st high-order can be obtained. Based on the Q-k relationship, the threshold gain is also calculated as the function of the wavevector k. The lowest threshold gain value g_{th0} is observed at k=0 for the fundamental mode, corresponding to the highest Q-factor in Q-k plot. The threshold gain difference (Δg_{th}) between the fundamental mode and 1st higher order mode for different Δk is calculated as the difference between $g_{th}(k)$ and g_{th0}. The device size diameter (L) is the reciprocal of Δk. The corresponding gain threshold differences Δg_{th} are plotted for different lattice designs as shown in Figure 6-2(b). The maximum single mode emission device size is the length L where Δg_{th} is greater than 1 cm^{-1} for any given photonic crystal cavity design near the current threshold (I_{th}) condition. Note this value may change depending on the bias conditions. At high current operation around 5 × I_{th}, due to band confinement effect (BCE) and spatial hole burning effect (SHB) affects, Δg_{th} value between 0th order and 1st modes decreases causing higher order modes

to lase. In order to maintain single mode emission even at higher current operation, PC cavity is designed such that Δg_{th} value is around 4 cm^{-1} [29]. The Δg_{th} changes as the operating conditions are changed. Based on this Δg_{th}-L relation, a circular airhole PCSEL with the Dirac cone design can be scaled to for maximum single mode emission up to a device size of 2,000 μm, compared with 400 μm maximum device size for a triangular airhole square lattice PCSEL with single mode operation. Noda *et al.* [68] employed composite double-lattice photonic crystal cavities with secondary lattice shifted by one-quarter wavelength in x- and y-directions. This enhances destructive interference between 180° diffracted waves to reduce the lateral confinement and suppress higher order modes with large gain threshold difference between fundamental mode and higher order that are located at the edge of the resonator. The device size can be scaled between 1,000 μm to 3,000 μm by adjusting the separation between primary and secondary airhole lattices. Based on the above analysis, it is possible to consider different lattice structures with engineered dispersion properties for large area single mode PCSELs. As shown in Figure 6-3, three different lattice designs can be considered for different size single mode PCSELs.
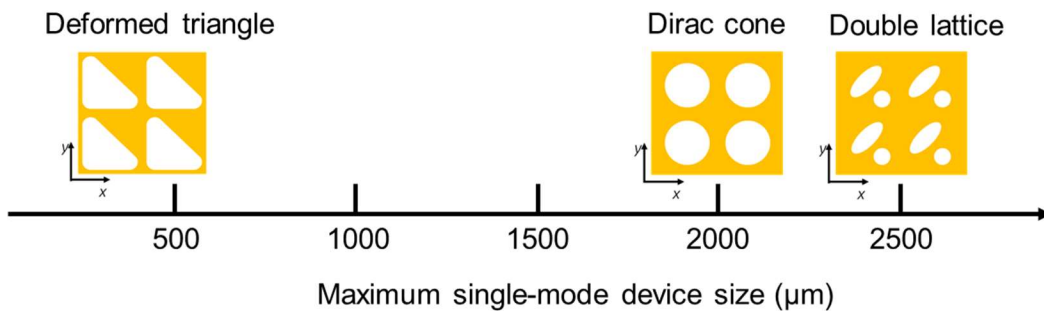
Figure 6-3. PC lattice designs for the scaling of PCSELs with single mode emissions

6.2 Multi-mode Emission at High Current Injection

Another issue with such a large area emitter is the change in the lasing mode at higher current injection levels. Though PCSELs offer high brightness (single mode emission) along with high power with broad area resonance, at higher current injections (around $4 \times I_{th}$) the transition from single mode lasing to multi-mode (higher order modes) lasing may occur, as reported by Noda *et al.* [68], thus reducing the beam quality.

This occurs due to two reasons: the band confinement effect and the spatial hole burning effect. In PCSELs, the photonic crystal cavity diameter would be larger than the p-metal contact diameter. Under higher current injection operation ($5 \times I_{th}$), the charge carriers spread up to ~25 μm radially. However, the charge carrier density would be higher under the metal contact compared to the surrounding region, even with p-pad contact. BCE is caused by the reduction in the refractive index of the PC layer in the emitter area (electrode region) when a large number of carriers are injected compared to the surrounding region. This temporal change in the gain distribution and reduction in refractive index results in higher band-edge frequency for the lasing mode in the current injection region than the surrounding area as shown in Figure 6-4(b). As a result, the surrounding area acts as a photonic band gap which means the photonic bandgap in the edges and surroundings of the emitter region is larger than that of the emitter region. This strengthens the in-plane optical confinement for the higher order modes which are typically located at the edges of the emitter and reduces the threshold gain difference between fundamental mode and higher order modes.
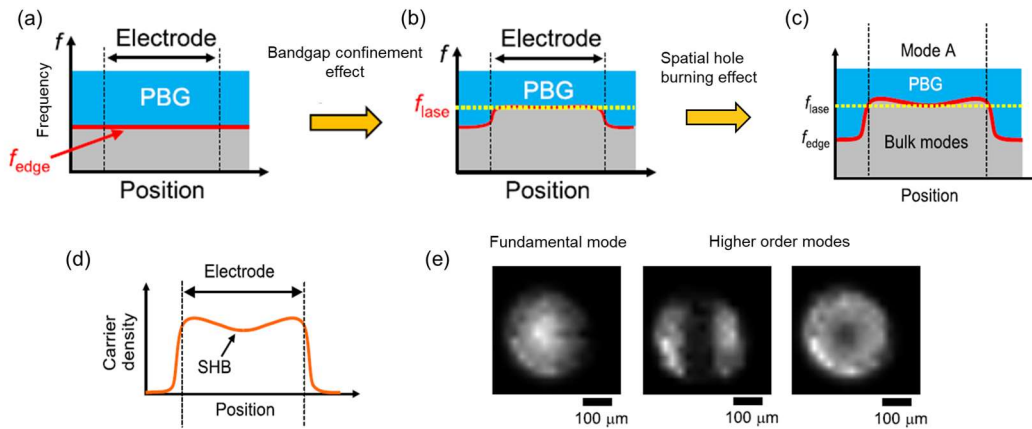
Figure 6-4. Schematic of the change in band-edge frequency f_{edge} (a) no current injection; (b) current injection causing bandedge confinement; (c) spatial hole burning resulting depletion of carriers at the center. Impact of bandedge confinement and spatial hole burning on (d) carrier distribution in the PCSEL and (e) multi-mode emission [68]. Note PBG: photonic band gap and SHB: spatial hole burning.

Similarly, the SHB effect causes the carriers in the center of the emitter region to be depleted due to the high electric field density in high-power operation, resulting in an increment in relative gain to higher order modes and turning the emission into multi-mode. In addition, the depletion of carriers at the center due to SHB increases the refractive index and reduces the band-edge frequency slightly as shown in Figure 6-4(c). This creates yet another small photonic bandgap at the center that alters the profile of fundamental mode profile from Gaussian to super-Gaussian. This is clearly observed in the near field patterns (NFPs) of fundamental and higher order modes of PCSEL emission at high current injections (> 10× I_{th}) as shown in, as reported by Noda *et al* [68].

6.3 Lateral Heterostructure Designs

Since the BCE and SHB effects happen in the PC cavity plane, efficient solutions to eliminate the impacts is to have laterally designed PC structures. The PC lattice parameters, such as lattice constant, air filling ratio determines the band structure and lasing mode characteristics. By introducing PC regions with different air hole filling ratio, a band discontinuity can be created to modulate the optical feedback strength to the cavity mode [69]. Considering the combined effects of BCE and SHB on the cavity, which is influenced by the current injection area and density, a compensation of refractive index change can be introduced by the PC lattice designs in the region surrounding the cavity region [52], [68].

(a)   (b)   (c)
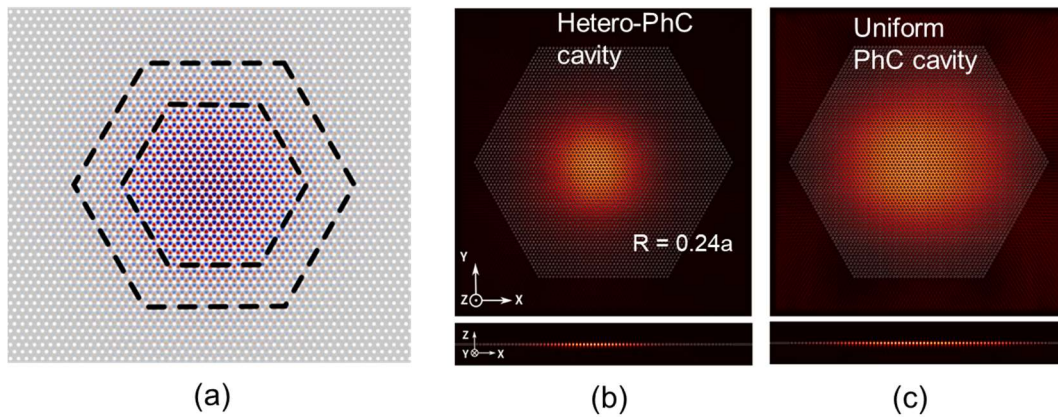
Figure 6-5 (a) Optical mode confinement in lateral heterostructure circular airhole hexagonal lattice photonic crystal cavity simulated using MEEP FDTD simulation; comparison of optical mode confinement in (b) lateral heterostructure PC cavity; and (c) uniform PC cavity [69].

Chapter 7

CONCLUDING REMARK AND FUTURE RESEARCH

In this thesis, monolithic Watt class high power photonic crystal surface emitting lasers are explored based on photonic bandedge effect and experimentally demonstrated at 1040 nm wavelength using multiple quantum well active region on GaAs substrate for LiDAR and 3D sensing applications. Various semiconductor laser configurations are detailed and limitations on power and beam characteristics are included. MBE and MOCVD growth techniques are evaluated and the impact on regrowth is verified for surface particles and interface defects. The epitaxial heterostructure is optimized for uniform charge injection, reduced current crowding, and higher extraction efficiency for high power lasers. Square lattice circular airhole, triangular airhole, double lattice and Dirac-cone are thoroughly investigated and the modal characteristics and gain-threshold estimations of bandedge modes in these photonic crystal cavities are summarized. The advantages of different photonic crystal cavities based on size, power and lasing characteristics are evaluated.

Circular airhole and triangular airhole photonic crystal cavities of size 200 μm x 200 μm are fabricated using relative-ion etching process. The impact of regrowth process on airhole shape and refilling is analyzed. Complete electrically injected PCSEL is processed after the regrowth process and innovative Si/PCSEL flip-chip bonding process is optimized using indium bumps to achieve uniform charge injection into the PCSEL cavity. The laser emission is collected from the backside of the polished substrate. The series resistance and electrode designs are optimized to reduce the cavity losses and to enhance uniform emission. Cavity pre-compensation is introduced to minimize the offset in wavelength of resonant mode caused due to refill of airhole in regrowth and achieved

97

excellent lasing characteristics in pulsed and CW operation. Upto 1 W output power is achieved under pulsed operation from a single 200 μm emitter at 3 A current injection which is limited by the current source. The full width half maximum of 50 pm and side mode suppression ratio of greater than 40 dB are recorded. The experimental lasing characteristics are in good agreement with the simulation. Output power can be further improved by adding anti-reflection coating and carefully optimizing the thickness of p+ GaAs layer for constructive interference between upward and downward reflected emission. Thermal impact on lasing mode is evaluated under CW operation and recorded 100 mW output power at 1.5 A which is thermally limited. The spectral characteristics in CW operation show 100 pm linewidth and 30 dB side mode suppression ratio. CVD diamond submounts and active cooling approaches re suggested to mitigate the thermal issues.

Various photonic crystal cavities are investigated for large area single mode emission. Innovative Q-k relationship is established to predict the differential gain-threshold between fundamental mode and higher order modes; and the theoretical concept is further developed to predict the maximum single mode emission size to reduce the time and computational resources to solve large area finite-size PC cavities. Circular airhole Dirac-cone cavity and double lattice cavities can be scaled to mm sizes while maintain the single mode emission to achieve output powers in hundreds of Watts range.

In the future, these Dirac-cone and double lattice PCSEL are fabricated to scale the emitter sizes to mm and cm range and achieve high beam quality emission. Further, wafer scale PCSEL can be realized by carefully optimizing the spacing between the primary and secondary lattice in composite double lattice designs. Huge output power levels upto kW can be realized in wafer scale emitter which are excellent candidates for military and courter-measure applications.

In addition, the emitter sizes of PCSELs can be scaled down to a few tens of micrometers to achieve high speed response for optical communication and data transfer applications. Optical simulations carried out using COMSOL indicated that upto 100 mW output power, 10 GHz speed and 1 MHz linewidth can be achieved in PCSELs considering the trade-off between size, speed and Q-factor.

Unlike the VCSELs where the availability of high reflective DBR materials create bottle neck to scale the wavelengths of operations, PCSELs offer multiple advantageous in scaling the wavelength. Other wavelength regions 250 nm, 1.3 μm and 2 μm can be explored based on AlGaN MQW [70]–[72], GaAs quantum dots [73] [74] and GaSb quantum dashes [75]. The base substrate can be used to realize the PC geometry and high output power levels can be demonstrated in wavelengths ranging from UV-C to Near IR and Far IR regions.

Large scale production of PCSELs for commercial applications can be ramped up with the robust and high yield fabrication process developed and reported in this thesis. Wafer scale production enables cost effective and reliable PCSELs overcoming the technical challenges of PC fabrication and regrowth.

Appendix A

OPTICALLY PUMPED ULTRA-VIOLET EDGE EMITTING LASER

A.1 Introduction

Since the first demonstration of laser diode (LD) on group III-nitride materials some 20 years ago, technology has significantly matured with the availability of high quality GaN and, recently, AlN substrates. This led to the demonstrations of high-performance laser diodes ranging from infrared to visible and down to the UV spectral regime claiming their applications in high-density data storage, spectroscopy, sterilization, chemical detection, communications, and manufacturing industry [76], [77]. However, the development towards deep UV (<300 nm) lasers remains a great challenge mainly due to the lack of high quality single crystalline native AlN substrate. On the other hand, AlGaN devices grown on foreign substrates such as sapphire and silicon carbide suffer higher threading dislocation densities up to 10^{10} cm^{-2} and reduce the internal quantum efficiency. In addition, strain in AlGaN epitaxial layers due to lattice mismatch forms cracks when layers exceed critical thickness [78]–[80]. This results in an increase in non-radiative recombination centers, higher threshold and lower slope efficiency.

Optically pumped lasers based on AlGaN/AlN heterostructures at deep UV have recently been demonstrated by some groups using the MOCVD growth technique. Most of the reports are based on 3 to 10 periods of MQWs with threshold power densities ranging from 1200 kW/cm^2 down to 6 kW/cm^2. In 2004, a 3-pair 5 nm/10 nm nm $Al_{0.66}Ga_{0.34}N/Al_{0.76}Ga_{0.24}N$ MQWs LD structure was demonstrated by Takano *et al*. at 241.5 nm with threshold of 1200 kW/cm^2 grown on 4H-SiC substrate [81]. Wunderer in 2011 reported a 3-pair AlGaN MQWs laser structure with threshold of 126 kW/cm^2 at 267 nm [82]. In 2014, Guo *et al*. reported a 10-pair 1.6 nm/4 nm $Al_{0.5}Ga_{0.5}N/Al_{0.7}Ga_{0.3}N$ MQW edge

emitting laser at 265 nm with threshold of 150 kW/cm^2 [83]. The per QW threshold is calculated to be 15 kW/cm^2, but the full width half maximum (FWHM) is 1.8 nm. Most recently in 2018, Kirste *et al.* reported a 3-period 2.5 nm Al$_{0.55}$Ga$_{0.45}$N/AlN MQW laser at 267 nm with low threshold power density of 6 kW/cm^2 by reducing unintentional point defects in the active region through high supersaturation growth conditions for waveguide layer. However, the FWHM is still approximately 1 nm [84]. The threshold power density was decreased by increasing the Al composition in barriers thus increasing the barrier height to confine the carriers within the wells. These trends show a reduction in threshold power density by reducing the point defects, increasing the barrier height and optimizing the number of QWs and their thickness. However, the narrowest reported lasing linewidth is around 0.8 nm [79], [85]. Similar to the threshold power density, the linewidth can also be further narrowed down with better growth quality of AlN epitaxial layers, thus increasing the laser characteristics.

In this work, a 21-period 2 nm Al$_{0.53}$Ga$_{0.47}$N/ 6 nm Al$_{0.7}$Ga$_{0.3}$N MQWs optically pumped laser on bulk AlN substrate by low pressure organometallic vapor phase epitaxy (LP-OMVPE) in a high-temperature reactor is reported [80], [86]. The results show a dominant deep UV laser peak at 280.3 nm, with lasing threshold of 320 kW/cm^2 and lasing FWHM of 0.08 nm at room temperature. Such a narrow spectral linewidth and low lasing threshold demonstrate high quality 21 QWs heterostructure growth [87].

A.2 Laser Cavity Design and Fabrication

Shown in Figure 0-1 is the complete laser structure grown on an AlN substrate by LP-OMVPE in a high-temperature reactor. Following an initial 400 nm AlN homoepitaxial layer on the AlN substrate, a Si-doped 600 nm n-Al$_{0.74}$Ga$_{0.26}$N contact/cladding layer was

grown prior to the 21-period 2 nm $Al_{0.53}Ga_{0.47}N$/6 nm $Al_{0.7}Ga_{0.3}N$ MQWs active region. XRD was carried out to verify the material growth quality.
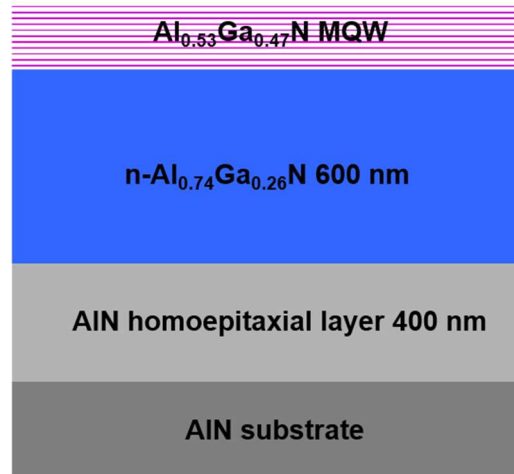
Figure 0-1 The deep UV laser heterostructure grown on AlN substrate with MQWs directly exposed to the air

Figure 0-2 shows the high-resolution X-Ray Diffraction (XRD) reciprocal space map. The measurement was carried out along (002) the direction with high-resolution triple axis scans. As shown in the RSM for a 21 AlGaN QW grown on AlN substrate, high quality pseudomorphic growth was achieved with very close agreement with simulation for a completely pseudomorphic structure.
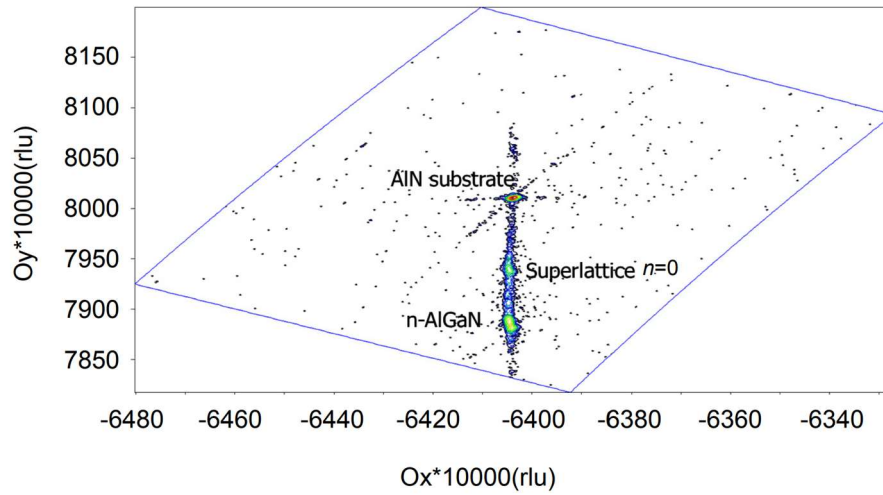
Figure 0-2 Pseudomorphic growth: High resolution XRD reciprocal space map

Figure 0-3 shows the simulation of mode profile in the heterostructure with 3, 15, and 21-period MQWs. This helps us to understand the confinement factor in the QWs and in turn the gain threshold value. We observed increments in the confinement factor as the number of QWs were increased. The heterostructure was designed to obtain a large modal confinement factor in the QW region. For the same heterostructure design, the optical mode confinement factor is stronger for 21 QWs with 18.51% for TE mode and 14.35% for TM mode respectively compared to 3 and 15-period QWs.
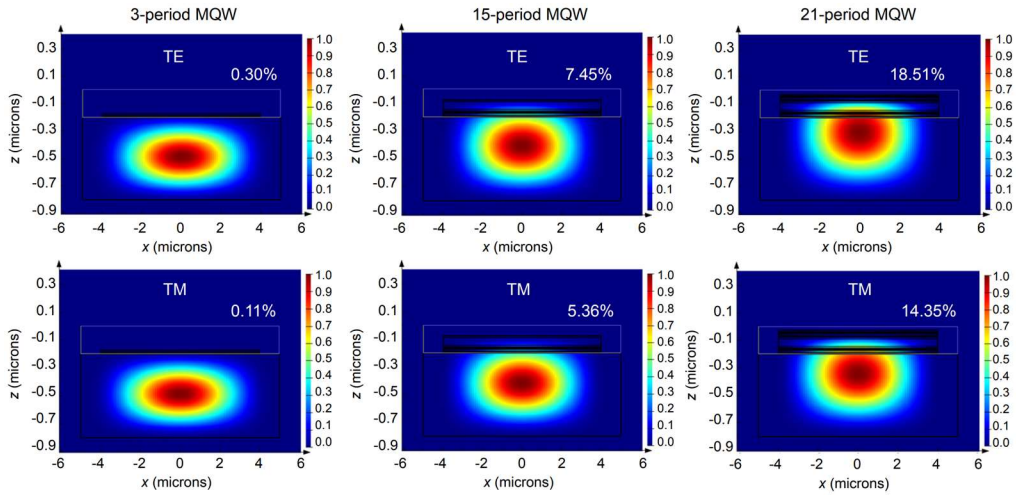
Figure 0-3 Simulations of TE and TM mode profiles in the heterostructure with 3, 15 and 21-period MQWs

Based on the design simulation results, different sets of QW designs are grown and tested to compare the peak intensity and gain region. Table 0-1 shows the heterostructure information of each sample including the number of QWs, Al composition in QWs and barriers. The surface photoluminescence (PL) was measured to identify the QWs emission and gain region.

Table 0-1 Structure information for different sets of QW designs with different numbers of QWs and different Al compositions

Sample	# of QWs	QWs composition $Al_xGa_{1-x}N$	QBs composition $Al_xGa_{1-x}N$	Peak Wavelength (nm)
S1	3	0.75	1	234
S2	15	0.75	1	234
S3	21	0.72	1	234
S4	21	0.58	1	251
S5	21	0.53	0.7	273

A circular 193 nm laser beam of 800 μm diameter was incident on the sample and emission was collected at 45° with respect to the incident beam. The measured PL spectra from each sample are shown in Figure 0-4(a). Figure 0-4(b) shows the peak PL emission intensities of heterostructure designs with 3, 15 and 21 MQWs at different pumping power densities. It is observed that for a given pump power density, the peak PL emission increased linearly with the number of QWs. Therefore, 21-period MQW structure is used for the laser device fabrication.
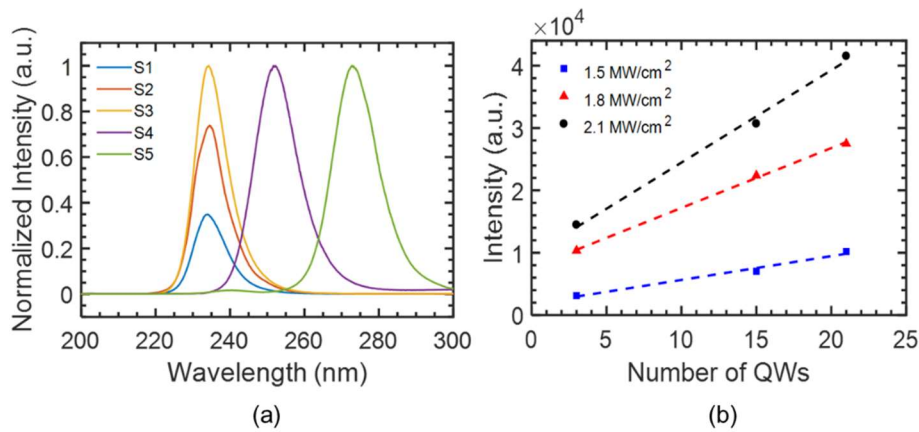
Figure 0-4 AlGaN QW growth on bulk AlN substrates (a) Photoluminescence spectra of different sets of QW designs with different number of QWs and different Al compositions shown in Table; and (b) Peak photoluminescence intensity for different sets of QWs

The emission intensity increased with the number of QWs as shown in Figure 0-4(b). Sample S5 with emission peak centered at 273 nm is considered to process the laser device as the emission from S5 sample is stronger than all the other samples at similar testing conditions. It is approximately 1.77 and 2.25 times stronger than S4 and S3 samples respectively. A subsequent chemical mechanical polishing (CMP) process was performed to thin down the substrate to around 70 μm.

A.3 Gain Measurement and Laser Characterization

The sample was then cleaved on one side to measure the net modal gain and loss using the variable-stripe length method. Figure 0-5 shows the photoluminescence experimental set up developed for the measurement of net modal gain.
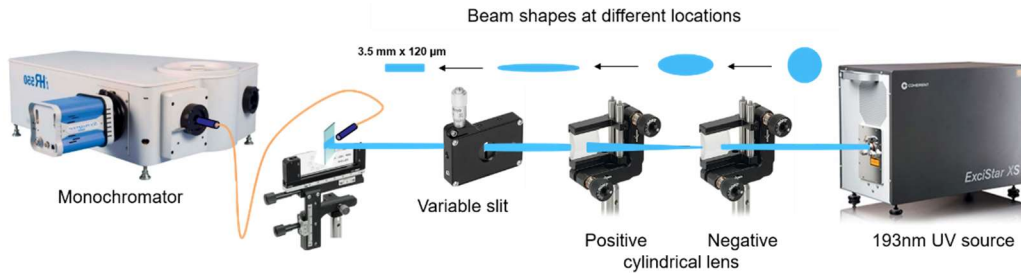
Figure 0-5 Schematic experimental set up to measure edge emission from cleaved facets

The stripe length is varied from 0.1 mm to 1 mm and emission from the facet is collected at various pump power densities. The onset of super-linearity is observed as the stripe length is increased from 0.5 mm, as shown in Figure 0-6.
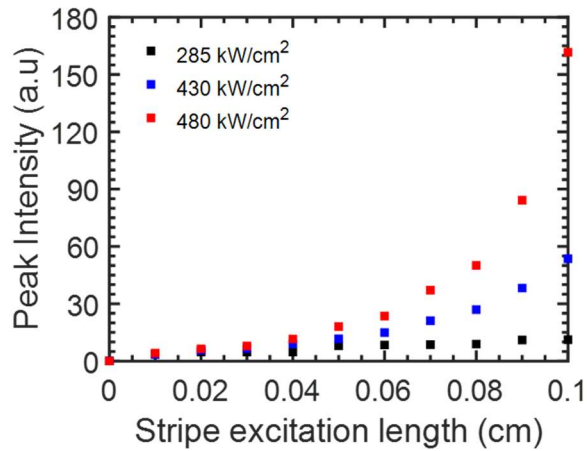
Figure 0-6 Peak emission intensities at different stripe excitation lengths for different pumping power densities

The net modal gain is calculated by fitting the peak emission intensities vs stripe excitation length plot by using Matlab to the equation:

$$I_{ASE}(l, \lambda) = \frac{A}{G(\lambda)} \left[e^{G(\lambda).l} - 1 \right] \qquad \text{(A.1)}$$

where I_{ASE} is the amplified spontaneous emission intensity at different stripe lengths l and wavelengths λ, A is the constant related to the spontaneous emission intensity, and G is the net optical gain as a function of wavelength. Figure 0-7(a) shows the gain spectra at different pump power densities. The net modal gain linearly increased with pump power up to 60 cm^{-1} and saturated from 500 kW/cm^2, as shown in Figure 0-7(b).
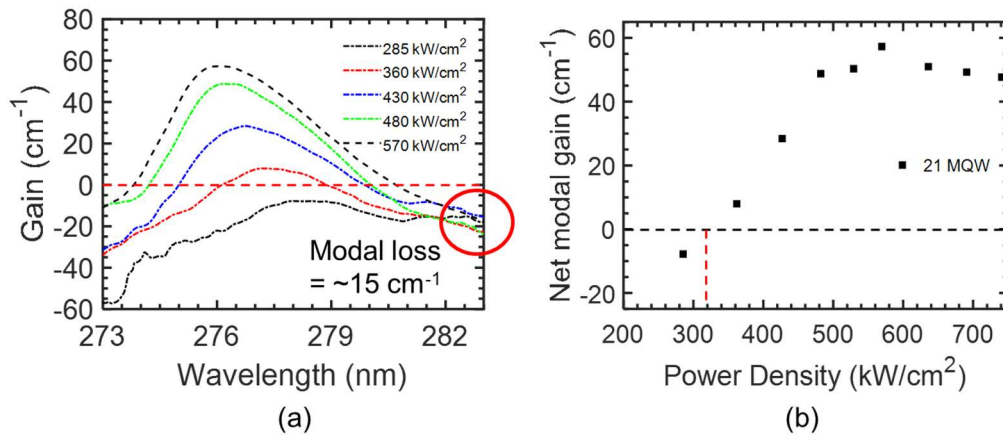
Figure 0-7 Optical gain measurement (a) measured gain spectra at different pump power densities; and (b) peak net modal gain at different pump power densities

Later, the other side was also cleaved to form two parallel facets, with a cavity length of 3.5 mm. The QWs were directly exposed to the air on the top side with Si-doped cladding on the bottom. The laser structure was optically pumped using a coherent 193 nm ArF deep UV excimer laser source with a 7 ns pulse width and 200 Hz repetition rate. Cylindrical lenses were inserted in the pumping beam path to control the pump beam shape and beam uniformity. All tests were carried out at room temperature. The emission was

collected from one of the cleaved edge facets into a fiber cable and coupled into an iHR550 monochromator of 2400 groves/mm grating with a spectral resolution of 0.01 nm. Figure 0-8(a) shows the measured spectral outputs at various pumping power densities with a pump beam width of 120 μm over the entire laser cavity length of 3.5 mm. Although the gain guided region is significantly broad, a dominant single mode lasing emission peak at 280 nm appeared above the threshold power density of 320 kW/cm^2. Figure 0-8(b) shows the light-light (L-L) characteristics on primary y-axis and FWHM variation with pumping power density in secondary y-axis. The linewidth was observed to be 0.08 nm, much narrower than any other DUV lasers reported so far (typ. 0.8 nm) [79], [85]. An elliptical shaped far-field pattern from the MQWs region was observed on the UV sensor card above the threshold at pumping power density of 350 kW/cm^2. The increase in the number of QWs has raised the threshold power density, but the threshold power density per QW is 15.2 kW/cm^2 which is still low for AlGaN MQWs structure with AlGaN barriers. These results with the low per QW threshold power density and narrow linewidth suggest excellent QW heterostructure cavity and low optical loss in the processed laser structure.

Polarization properties were also measured, as shown in Figure 0-9. Below threshold, we observed TE dominated emission with a TE/TM ratio of 2. On the other hand, above threshold, the emission is 100% TE polarized without any TM modes. These results are also in agreement with earlier reported work indicating dominant TE mode above 240 nm [88].
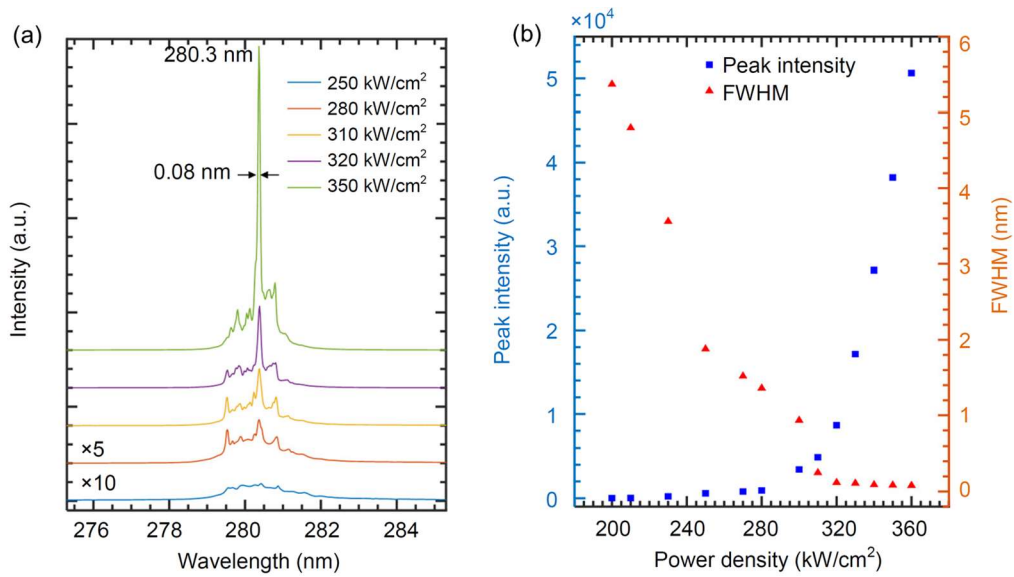
Figure 0-8 Optically pumped laser emission measurement (a) Edge emission spectra measured from the cleaved facet at different pump power densities; and (b) Measured L-L curve and FWHM at different pump power densities
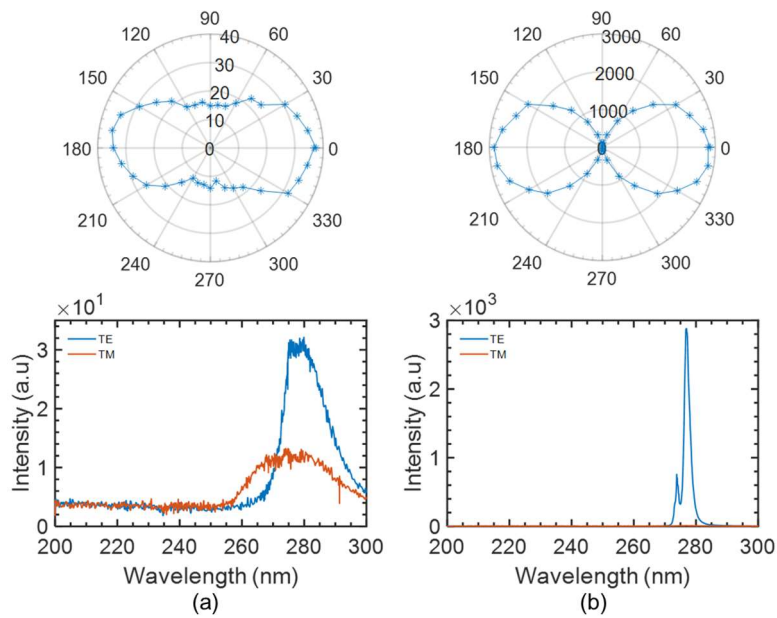
Figure 0-9 Polarization measurement (a) below threshold at 230 kW/cm²; and (b) above threshold at 350 kW/cm²

A.4 Conclusion

We successfully demonstrated an optically pumped 280 nm deep UV edge emitting laser under pulsed operation at room temperature with a threshold of 320 kW/cm^2 and lasing linewidth of 0.08 nm. The threshold per QW is only 15 kW/cm^2, suggesting high-quality crystal growth and processed laser cavity.

Appendix B

LIST OF PUBLICATIONS

Journal Publications

1. **A. Kalapala**, A. Song, M. Pan, C. Gautam, L. Overman, K. Reilly, T. Rotter, G. Balakrishnan, R. Gibson, R. Bedford, J. Coleman, S. Fan, and W. Zhou, "Scaling Challenges in High Power Photonic Crystal Surface-Emitting Lasers", IEEE Journal of Quantum Electronics (2022). (In press doi: 10.1109/JQE.2022.3165314)
2. **A. Kalapala**, D. Liu, S. J. Cho, J. Park, D. Zhao, R. Dalmau, J. Albrecht, B. Moody, Z. Ma, and W. Zhou, "Optically pumped room temperature low threshold deep UV lasers grown on native AlN substrates", Opto-Electronic Advances 3(04), p.190025 (2020).
3. A. Song, **A. Kalapala**, R. Gibson, K. Reilly, T. Rotter, S. Addamane, H. Wang, C. Guo, G. Balakrishnan, R. Bedford, W. Zhou, and S. Fan, "Controllable finite ultra-narrow quality-factor peak in a perturbed Dirac-cone band structure of a photonic-crystal slab", Applied Physics Letters, vol. 119, p. 031105, (2021).
4. M. Pan, Z. Liu, **A. Kalapala**, Y. Chen, Y. Sun, and W. Zhou, "Complete 2π Phase Control by Photonic Crystal Slabs", Optical Express 29, 40795-40804 (2021).
5. K. Das and **A. Kalapala**, "Spectral Properties of Optical Glare or Positive Dysphotopsia for Different Types of Intraocular Lenses", Biomedical Optical Express (2022) (Submitted).
6. K. Reilly, **A. Kalapala**, S. Yeom, S. Addamane, E. Renteria, W. Zhou and G. Balakrishnan, "Epitaxial Regrowth and Hole Shape Engineering for Photonic Crystal Surface Emitting Lasers", Journal of Crystal Growth, vol. 535, p. 125531 (2020).
7. C. Reuterskiöld Hedlund, J. Martins De Pina, **A. Kalapala**, Z. Liu, W. Zhou, and M. Hammar, "Buried InP/Airhole Photonic-Crystal Surface-Emitting Lasers," Phys. status solidi A, p. 2000416 (2020).
8. D. Liu, S. J. Cho, H. Zhang, C. Carlos, **A. Kalapala**, J. Park, J. Kim, Dalmau, J. Gong, B. Moody, X. Wang, J. Albrecht, W. Zhou and Z. Ma, "Influences of screw dislocations on electroluminescence of AlGaN/AlN-based UVC LEDs", AIP Advances, vol. 9, p. 085128 (2019).
9. A. Song, **A. Kalapala**, W. Zhou, and S. Fan, "First-principles simulation of photonic crystal surface-emitting lasers using rigorous coupled wave analysis", Applied Physics Letters, vol. 113, p. 041106 (2018).
10. M. Kim, H. Huang, J. D. Kim, K. Chabak, **A. Kalapala**, W. Zhou and X. Li, "Nanoscale groove textured β-Ga2O3 by room temperature inverse metalassisted chemical etching and photodiodes with enhanced responsivity," Applied Physics Letters, vol. 113, p. 222104 (2018).
11. D. Liu, S. Cho, J. Park, J. Gong, J. Seo, R. Dalmau, D. Zhao, K. Kim, M. Kim, **A. Kalapala**, J. Albrecht, W. Zhou, B. Moody, and Z. Ma, "226 nm AlGaN/AlN UV LEDs using p-type Si for hole injection and UV reflection", Applied Physics Letters, vol. 113, p. 011111 (2018).

Conference Proceedings

1. **A. Kalapala**, C. Guo, L. Overman, M. Vasilyev, J. Coleman, and W. Zhou, "Linewidth and Cavity Feedback in Photonic Crystal Surface Emitting Lasers", IEEE Photonics Conference (IPC), Oct. 18-21 (2021).

2. K. Das and **A. Kalapala**, "Spectral Properties of Glare or Positive Dysphotopsia for Different Types of Intraocular Lenses", Investigative Ophthalmology and Vision Sciences, vol. 68, p. 496 (2021).

3. **A. Kalapala**, S. Yeom, S. Addamane, K. Reilly, A. Song, R. Gibson, G. Balakrishnan, R. Bedford, S. Fan and W. Zhou, "Optically pumped 1 μm low threshold photonic crystal surface emitting lasers grown on GaAs substrate", IEEE Photonics Conference (IPC), San Antonio, TX, Sep. 29 - Oct. 3 (2019).

4. **A. Kalapala**, D. Liu, S. J. Cho, J. Park, D. Zhao, R. Dalmau, J. Albrecht, B. Moody, Z. Ma, and W. Zhou, "Optically pumped room temperature low threshold deep UV lasers grown on native AlN substrates", Photonics West, San Francisco, CA, Feb 2-7 (2019)

5. K. Reilly, **A. Kalapala**, A. Song, T. Rotter, Z. Liu, E. Renteria, S. Fan, W. Zhou, and G. Balakrishnan, "Fabrication of Photonic Crystal Surface Emitting Lasers (PCSELs) by Epitaxial Regrowth", CLEO, San Jose, CA, May 9-14 (2021).

6. A. Song, **A. Kalapala**, W. Zhou, and S. Fan, "First-principles simulation of photonic crystal surface-emitting lasers using rigorous coupled wave analysis", Photonics West, San Francisco, CA, Feb 2-7 (2019).

7. K. Reilly, S. Addamane, E. Renteria, **A. Kalapala**, S. Yeom, W. Zhou, and G. Balakrishnan, "Epitaxial Growth of Photonic Crystal Surface Emitting Lasers", Material Science & Technology Conference, Columbus, OH (2018).

References

[1] F. Kneubuehl and M. Sigrist, "Laser. 2. rev. and enl. ed. Laser," 1989.

[2] H. Dahnke, S. Stry, and G. von Basum, "Medical trace gas detection by means of mid-infrared cavity leak-out spectroscopy," in *Laser in Environmental and Life Sciences*, Springer, 2004, pp. 283–295.

[3] Susumu Noda, "Progress of Photonic Crystal Surface-Emitting Lasers: Paradigm Shift for LiDAR Sensing and Laser Processing," Mar. 2021, vol. 11672. doi: 10.1117/12.2593114.

[4] S. Noda *et al.*, "Photonic crystal lasers: Fabrication with AI-assisted technology and application to LiDAR system," 2021, vol. 11703, p. 117030M.

[5] B. Heinen *et al.*, "106 W continuous-wave output power from vertical-external-cavity surface-emitting laser," *Electronics letters*, vol. 48, no. 9, pp. 516–517, 2012.

[6] T.-L. Wang *et al.*, "Quantum design strategy pushes high-power vertical-external-cavity surface-emitting lasers beyond 100 W," *Laser & Photonics Reviews*, vol. 6, no. 5, pp. L12–L14, Sep. 2012, doi: 10.1002/lpor.201200034.

[7] Jean-Francois Seurin *et al.*, "Progress in high-power high-efficiency VCSEL arrays," Feb. 2009, vol. 7229. doi: 10.1117/12.808294.

[8] J.-F. P. Seurin, "High-Power VCSEL Arrays," in *VCSELs: Fundamentals, Technology and Applications of Vertical-Cavity Surface-Emitting Lasers*, R. Michalzik, Ed. Berlin, Heidelberg: Springer Berlin Heidelberg, 2013, pp. 263–290. doi: 10.1007/978-3-642-24986-0_8.

[9] K. Hirose, Y. Liang, Y. Kurosaka, A. Watanabe, T. Sugiyama, and S. Noda, "Watt-class high-power, high-beam-quality photonic-crystal lasers," *Nature Photonics*, vol. 8, no. 5, pp. 406–411, May 2014, doi: 10.1038/nphoton.2014.75.

[10] Holger Moench, Stephan Gronenborn, Michael Miller, and Peter Loosen, "High power VCSEL systems for tailored intensity distributions," Feb. 2011, vol. 7952. doi: 10.1117/12.873813.

[11] Holger Moench *et al.*, "High-power VCSEL systems and applications," Mar. 2015, vol. 9348. doi: 10.1117/12.2076267.

[12] A. Paranjpe, "The Right Conditions for Growth," *Physics World*, 2019.

[13] J. Zhang *et al.*, "High-power vertical external-cavity surface-emitting laser emitting switchable wavelengths," *Opt. Express*, vol. 28, no. 22, pp. 32612–32619, Oct. 2020, doi: 10.1364/OE.405062.

[14] S. Noda, "Photonic crystal lasers—ultimate nanolasers and broad-area coherent lasers [Invited]," *J. Opt. Soc. Am. B*, vol. 27, no. 11, pp. B1–B8, Nov. 2010, doi: 10.1364/JOSAB.27.0000B1.

[15] O. Painter *et al.*, "Two-dimensional photonic band-gap defect mode laser," *Science*, vol. 284, no. 5421, pp. 1819–1821, 1999.

[16] J. K. Hwang *et al.*, "Continuous room-temperature operation of optically pumped two-dimensional photonic crystal lasers at 1.6 µm," *IEEE Photonics Technology Letters*, vol. 12, no. 10, pp. 1295–1297, Oct. 2000, doi: 10.1109/68.883808.

[17] W. Zhou *et al.*, "Electrically injected single-defect photonic bandgap surface-emitting laser at room temperature," *Electronics Letters*, vol. 36, no. 18, pp. 1541–1542, 2000.

[18] H.-G. Park *et al.*, "Electrically driven single-cell photonic crystal laser," *Science*, vol. 305, no. 5689, pp. 1444–1447, 2004.

[19] H. Altug and J. Vučković, "Photonic crystal nanocavity array laser," *Optics express*, vol. 13, no. 22, pp. 8819–8828, 2005.

[20] M. Imada, S. Noda, A. Chutinan, T. Tokuda, M. Murata, and G. Sasaki, "Coherent two-dimensional lasing action in surface-emitting laser with triangular-lattice photonic crystal structure," *Appl. Phys. Lett.*, vol. 75, no. 3, pp. 316–318, Jul. 1999, doi: 10.1063/1.124361.

[21] M. Imada, A. Chutinan, S. Noda, and M. Mochizuki, "Multidirectionally distributed feedback photonic crystal lasers," *Phys. Rev. B*, vol. 65, no. 19, p. 195306, Apr. 2002, doi: 10.1103/PhysRevB.65.195306.

[22] G. Vecchi *et al.*, "Continuous-wave operation of photonic band-edge laser near 1.55 μm on silicon wafer," *Optics Express*, vol. 15, no. 12, pp. 7551–7556, 2007.

[23] T. Sakaguchi *et al.*, "Surface-Emitting Photonic-Crystal Laser with 35W Peak Power," in *Conference on Lasers and Electro-Optics/International Quantum Electronics Conference*, Baltimore, Maryland, May 2009, p. CTuH1. doi: 10.1364/CLEO.2009.CTuH1.

[24] D. Zhao *et al.*, "Printed Large-Area Single-Mode Photonic Crystal Bandedge Surface-Emitting Lasers on Silicon," *Scientific Reports*, vol. 6, no. 1, p. 18860, Jan. 2016, doi: 10.1038/srep18860.

[25] G. Li, J. Sarma, and R. Hogg, "Evaluating resonances in PCSEL structures based on modal indices," *IET Optoelectronics*, vol. 13, no. 1, pp. 17–22, 2019.

[26] R. J. E. Taylor *et al.*, "Electronic control of coherence in a two-dimensional array of photonic crystal surface emitting lasers," *Scientific Reports*, vol. 5, no. 1, p. 13203, Aug. 2015, doi: 10.1038/srep13203.

[27] H. J. Unold, M. Golling, R. Michalzik, D. Supper, and K. J. Ebeling, "Photonic crystal surface-emitting lasers: tailoring waveguiding for single-mode emission," in *Proceedings 27th European Conference on Optical Communication (Cat. No.01TH8551)*, Oct. 2001, vol. 4, pp. 520–521 vol.4. doi: 10.1109/ECOC.2001.989088.

[28] Susumu Noda, "Two decades of progress for photonic crystals: from the realization of complete 3D crystals to the state of the art for society 5.0," Mar. 2019, vol. 10927. doi: 10.1117/12.2518570.

[29] M. Yoshida *et al.*, "Double-lattice photonic-crystal resonators enabling high-brightness semiconductor lasers with symmetric narrow-divergence beams," *Nature Materials*, vol. 18, no. 2, pp. 121–128, Feb. 2019, doi: 10.1038/s41563-018-0242-y.

[30] Noda Susumu, Yokoyama Mitsuru, Imada Masahiro, Chutinan Alongkarn, and Mochizuki Masamitsu, "Polarization Mode Control of Two-Dimensional Photonic Crystal Laser by Unit Cell Structure Design," *Science*, vol. 293, no. 5532, pp. 1123–1125, Aug. 2001, doi: 10.1126/science.1061738.

[31] E. Miyai, K. Sakai, T. Okano, W. Kunishi, D. Ohnishi, and S. Noda, "Lasers producing tailored beams," *Nature*, vol. 441, no. 7096, pp. 946–946, Jun. 2006, doi: 10.1038/441946a.

[32] R. J. E. Taylor *et al.*, "Coherently Coupled Photonic-Crystal Surface-Emitting Laser Array," *IEEE Journal of Selected Topics in Quantum Electronics*, vol. 21, no. 6, pp. 493–499, Dec. 2015, doi: 10.1109/JSTQE.2015.2417998.

[33] H.-L. Chiu, K.-B. Hong, K.-C. Huang, and T.-C. Lu, "Photonic Crystal Surface Emitting Lasers with Naturally Formed Periodic ITO Structures," *ACS Photonics*, vol. 6, no. 3, pp. 684–690, Mar. 2019, doi: 10.1021/acsphotonics.8b01530.

[34] W. Zhou *et al.*, "On-Chip Photonic Crystal Surface-Emitting Membrane Lasers," *IEEE Journal of Selected Topics in Quantum Electronics*, vol. 25, no. 3, pp. 1–11, Jun. 2019, doi: 10.1109/JSTQE.2019.2902904.

[35] D. Zhao *et al.*, "Lateral size scaling of photonic crystal bandedge lasers on SOI substrates," 2016, pp. 17–21.

[36] A. R. K. Kalapala *et al.*, "Optically Pumped 1 µm Low Threshold Photonic Crystal Surface Emitting Lasers Grown on GaAs Substrate," in *2019 IEEE Photonics Conference (IPC)*, Oct. 2019, pp. 1–2. doi: 10.1109/IPCon.2019.8908472.

[37] C. Reuterskiöld Hedlund, J. Martins De Pina, A. Kalapala, Z. Liu, W. Zhou, and M. Hammar, "Buried InP/Airhole Photonic-Crystal Surface-Emitting Lasers," *physica status solidi (a)*, vol. 218, no. 3, p. 2000416, Feb. 2021, doi: 10.1002/pssa.202000416.

[38] J. D. Joannopoulos, S. G. Johnson, J. N. Winn, and R. D. Meade, "Molding the flow of light," *Princeton Univ. Press, Princeton, NJ [ua]*, 2008.

[39] C. M. Soukoulis, *Photonic crystals and light localization in the 21st century*, vol. 563. Springer Science & Business Media, 2012.

[40] S. Noda and T. Baba, *Roadmap on photonic crystals*, vol. 1. Springer Science & Business Media, 2003.

[41] K. Sakoda, *Optical properties of photonic crystals*, vol. 80. Springer Science & Business Media, 2004.

[42] R. Taylor, "Design of photonic crystal surface emitting lasers and the realisation of coherently coupled arrays," University of Sheffield, Sheffield, 2015.

[43] S. Shi, C. Chen, and D. W. Prather, "Plane-wave expansion method for calculating band structure of photonic crystal slabs with perfectly matched layers," *JOSA A*, vol. 21, no. 9, pp. 1769–1775, 2004.

[44] J. Martins de Pina, "Design and Fabrication of 1550 nm Photonic Crystal Surface Emitting Lasers," KTH Royal Institute of Technology, Sweden, 2018.

[45] S.-L. Chua, L. Lu, J. Bravo-Abad, J. D. Joannopoulos, and M. Soljačić, "Larger-area single-mode photonic crystal surface-emitting lasers enabled by an accidental Dirac point," *Opt. Lett.*, vol. 39, no. 7, pp. 2072–2075, Apr. 2014, doi: 10.1364/OL.39.002072.

[46] K. Sakai, E. Miyai, T. Sakaguchi, D. Ohnishi, T. Okano, and S. Noda, "Lasing band-edge identification for a surface-emitting photonic crystal laser," *IEEE Journal on Selected Areas in Communications*, vol. 23, no. 7, pp. 1335–1340, Jul. 2005, doi: 10.1109/JSAC.2005.851205.

[47] M. Meier *et al.*, "Laser action from two-dimensional distributed feedback in photonic crystals," *Appl. Phys. Lett.*, vol. 74, no. 1, pp. 7–9, Jan. 1999, doi: 10.1063/1.123116.

[48] Y. Kurosaka *et al.*, "On-chip beam-steering photonic-crystal lasers," *Nature Photonics*, vol. 4, no. 7, pp. 447–450, Jul. 2010, doi: 10.1038/nphoton.2010.118.

[49] B. Luk'yanchuk *et al.*, "The Fano resonance in plasmonic nanostructures and metamaterials," *Nature Materials*, vol. 9, no. 9, pp. 707–715, Sep. 2010, doi: 10.1038/nmat2810.

[50] K. J. Reilly *et al.*, "Epitaxial regrowth and hole shape engineering for photonic crystal surface emitting lasers (PCSELs)," *Journal of Crystal Growth*, vol. 535, p. 125531, 2020.

[51] K. J. Reilly *et al.*, "Fabrication of Photonic Crystal Surface Emitting Lasers (PCSELs) by Epitaxial Regrowth," 2021, pp. 1–2.

[52] A. Kalapala *et al.*, "Scaling Challenges in High Power Photonic Crystal Surface-Emitting Lasers," *IEEE Journal of Quantum Electronics*, pp. 1–1, 2022, doi: 10.1109/JQE.2022.3165314.

[53] G. D. Cole, E. Behymer, T. C. Bond, and L. L. Goddard, "Short-wavelength MEMS-tunable VCSELs," *Optics Express*, vol. 16, no. 20, pp. 16093–16103, 2008.

[54] Y. Wang, Y. Wang, L. Li, Y. Zhao, G. Feng, and X. Wang, "Research on rapid thermal annealing of ohmic contact to GaAs," 2012, pp. 61–63.

[55] B. Jacobs, M. Kramer, E. Geluk, and F. Karouta, "Optimisation of the Ti/Al/Ni/Au ohmic contact on AlGaN/GaN FET structures," *Journal of Crystal Growth*, vol. 241, no. 1–2, pp. 15–18, 2002.

[56] K. N. Patel, E. Stokes, J. Pagan, C. C. Burkhart, M. Hodge, and P. Batoni, "Circular Transmission Line Model (CTLM) Analysis for Non-Linear VI Characteristics on Mg doped GaN," *ECS Transactions*, vol. 11, no. 5, pp. 203–208, Sep. 2007, doi: 10.1149/1.2783873.

[57] M. De Zoysa *et al.*, "Thermal management for CW operation of large-area double-lattice photonic-crystal lasers," *J. Opt. Soc. Am. B*, vol. 37, no. 12, pp. 3882–3887, Dec. 2020, doi: 10.1364/JOSAB.411086.

[58] A. Y. Song *et al.*, "Controllable finite ultra-narrow quality-factor peak in a perturbed Dirac-cone band structure of a photonic-crystal slab," *Appl. Phys. Lett.*, vol. 119, no. 3, p. 031105, Jul. 2021, doi: 10.1063/5.0056243.

[59] J. Jin, X. Yin, L. Ni, M. Soljačić, B. Zhen, and C. Peng, "Topologically enabled ultrahigh-Q guided resonances robust to out-of-plane scattering," *Nature*, vol. 574, no. 7779, pp. 501–504, 2019.

[60] C. W. Hsu, B. Zhen, A. D. Stone, J. D. Joannopoulos, and M. Soljačić, "Bound states in the continuum," *Nature Reviews Materials*, vol. 1, no. 9, pp. 1–13, 2016.

[61] A. Kodigala, T. Lepetit, Q. Gu, B. Bahari, Y. Fainman, and B. Kanté, "Lasing action from photonic bound states in continuum," *Nature*, vol. 541, no. 7636, pp. 196–199, 2017.

[62] M. I. Molina, A. E. Miroshnichenko, and Y. S. Kivshar, "Surface bound states in the continuum," *Physical review letters*, vol. 108, no. 7, p. 070401, 2012.

[63] L. Zhu *et al.*, "Angle-selective perfect absorption with two-dimensional materials," *Light: Science & Applications*, vol. 5, no. 3, pp. e16052–e16052, 2016.

[64] S. Noda, K. Kitamura, T. Okino, D. Yasuda, and Y. Tanaka, "Photonic-crystal surface-emitting lasers: Review and introduction of modulated-photonic crystals," *IEEE Journal of Selected Topics in Quantum Electronics*, vol. 23, no. 6, pp. 1–7, 2017.

[65] W. W. Chow, K. D. Choquette, M. H. Crawford, K. L. Lear, and G. R. Hadley, "Design, fabrication, and performance of infrared and visible vertical-cavity surface-emitting lasers," *IEEE Journal of Quantum Electronics*, vol. 33, no. 10, pp. 1810–1824, 1997.

[66] T. Inoue, R. Morita, M. Yoshida, M. De Zoysa, Y. Tanaka, and S. Noda, "Comprehensive analysis of photonic-crystal surface-emitting lasers via time-dependent three-dimensional coupled-wave theory," *Physical Review B*, vol. 99, no. 3, p. 035308, 2019.

[67] K. Koshelev, S. Lepeshov, M. Liu, A. Bogdanov, and Y. Kivshar, "Asymmetric metasurfaces with high-Q resonances governed by bound states in the continuum," *Physical review letters*, vol. 121, no. 19, p. 193903, 2018.

[68] M. Yoshida *et al.*, "Experimental investigation of lasing modes in double-lattice photonic-crystal resonators and introduction of in-plane heterostructures," *Proceedings of the IEEE*, vol. 108, no. 5, pp. 819–826, 2019.

[69] X. Ge, M. Minkov, S. Fan, X. Li, and W. Zhou, "Laterally confined photonic crystal surface emitting laser incorporating monolayer tungsten disulfide," *npj 2D Materials and Applications*, vol. 3, no. 1, p. 16, Apr. 2019, doi: 10.1038/s41699-019-0099-1.

[70] T.-T. Wu, P.-H. Weng, Y.-J. Hou, and T.-C. Lu, "GaN-based photonic crystal surface emitting lasers with central defects," *Appl. Phys. Lett.*, vol. 99, no. 22, p. 221105, Nov. 2011, doi: 10.1063/1.3665251.

[71] T. Wu, P. Weng, Y. Hou, and T. Lu, "Characteristics of GaN-based Photonic crystal surface emitting lasers with central defects," in *2012 Conference on Lasers and Electro-Optics (CLEO)*, May 2012, pp. 1–2.

[72] S. W. Chen, T. C. Lu, and T. T. Kao, "Study of GaN-based photonic crystal surface-emitting lasers (PCSELs) with AlN/GaN distributed Bragg reflectors," *IEEE Journal of Selected Topics in Quantum Electronics*, vol. 15, no. 3, pp. 885–891, 2009.

[73] M.-Y. Hsu and G. Lin, "Quantum-dot photonic-crystal surface-emitting lasers with bottom distributed bragg reflector," 2018, vol. 5, no. 3, p. 27.

[74] H.-Y. Lu *et al.*, "Extracting more light for vertical emission: high power continuous wave operation of 1.3-μm quantum-dot photonic-crystal surface-emitting laser based on a flat band," *Light: Science & Applications*, vol. 8, no. 1, p. 108, Nov. 2019, doi: 10.1038/s41377-019-0214-2.

[75] H.-W. Cheng, S.-C. Lin, Z.-L. Li, K.-W. Sun, and C.-P. Lee, "PCSEL performance of type-I InGaAsSb double-QWs laser structure prepared by MBE," *Materials*, vol. 12, no. 2, p. 317, 2019.

[76] S. Nakamura, S. Pearton, and G. Fasol, *The blue laser diode: the complete story*. Springer Science & Business Media, 2000.

[77] T. Kinoshita *et al.*, "Performance and reliability of deep-ultraviolet light-emitting diodes fabricated on AlN substrates prepared by hydride vapor phase epitaxy," *Applied Physics Express*, vol. 6, no. 9, p. 092103, 2013.

[78] H. Yoshida, Y. Yamashita, M. Kuwabara, and H. Kan, "A 342-nm ultraviolet AlGaN multiple-quantum-well laser diode," *Nature Photonics*, vol. 2, no. 9, pp. 551–554, Sep. 2008, doi: 10.1038/nphoton.2008.135.

[79] J. Xie *et al.*, "Lasing and longitudinal cavity modes in photo-pumped deep ultraviolet AlGaN heterostructures," *Appl. Phys. Lett.*, vol. 102, no. 17, p. 171102, Apr. 2013, doi: 10.1063/1.4803689.

[80] V. Adivarahan *et al.*, "250nmAlGaN light-emitting diodes," *Appl. Phys. Lett.*, vol. 85, no. 12, pp. 2175–2177, Sep. 2004, doi: 10.1063/1.1796525.

[81] T. Takano, Y. Narita, A. Horiuchi, and H. Kawanishi, "Room-temperature deep-ultraviolet lasing at 241.5 nm of AlGaN multiple-quantum-well laser," *Appl. Phys. Lett.*, vol. 84, no. 18, pp. 3567–3569, May 2004, doi: 10.1063/1.1737061.

[82] T. Wunderer *et al.*, "Pseudomorphically Grown Ultraviolet C Photopumped Lasers on Bulk AlN Substrates," *Applied Physics Express*, vol. 4, no. 9, p. 092101, Aug. 2011, doi: 10.1143/apex.4.092101.

[83] W. Guo *et al.*, "Stimulated emission and optical gain in AlGaN heterostructures grown on bulk AlN substrates," *Journal of Applied Physics*, vol. 115, no. 10, p. 103108, Mar. 2014, doi: 10.1063/1.4868678.

[84] R. Kirste *et al.*, "6 kW/cm2 UVC laser threshold in optically pumped lasers achieved by controlling point defect formation," *Applied Physics Express*, vol. 11, no. 8, p. 082101, Jul. 2018, doi: 10.7567/apex.11.082101.

[85] Z. Bryan, I. Bryan, R. Kirste, R. Collazo, and Z. Sitar, "Status and challenges in deep UV semiconductor lasers," in *2015 IEEE Summer Topicals Meeting Series (SUM)*, Jul. 2015, pp. 123–124. doi: 10.1109/PHOSST.2015.7248225.

[86] Akhil R. K. Kalapala *et al.*, "Optically pumped room temperature low threshold deep UV lasers grown on native AlN substrates," Mar. 2019, vol. 10918. doi: 10.1117/12.2508717.

[87] A. R. K. Kalapala *et al.*, "Optically pumped room temperature low threshold deep UV lasers grown on native AlN substrates," *Opto-Electronic Advances*, vol. 3, no. 4, pp. 190025–1, 2020.

[88] J. E. Northrup *et al.*, "Effect of strain and barrier composition on the polarization of light emission from AlGaN/AlN quantum wells," *Appl. Phys. Lett.*, vol. 100, no. 2, p. 021101, Jan. 2012, doi: 10.1063/1.3675451.

Biographical Information

Akhil Raj Kumar Kalapala was born in Nuzvid, India. He received Bachelor's degree in 2016 from Rajiv Gandhi University of Knowledge Technologies, specializing in Electronics and Communications Engineering. During his undergrad studies, he participated in various research activities and competitions including space solar power satellite design conducted by NASA and Ohio University in 2014.

In Spring 2017, Akhil joined Dr. Weidong Zhou's Nanophotonics group at University of Texas at Arlington as a PhD candidate. His research interests include design, fabrication and characterization of photonic crystal surface lasers (PCSELs) and edge emitting lasers based on quantum dots. He has extensive simulation experience in Rsoft, RCWA, and FDTD packages. He demonstrated Watt class high power PCSELs for LiDAR and 3D sensing applications at 1.040 μm IR wavelength range.

He worked on ultra-violet edge emitting laser based on AlGaN MQW structures for deep UV-C band (<300 nm) wavelength applications. In addition, he was also involved in fabrication and demonstration of 1.3 μm quantum dot high speed edge emitting lasers for low-cost energy applications. He interned with Alcon Vision LLC. in summer of 2019, working on intraocular lens design with focus on positive dysphotopsia eye condition. He also worked on advanced innovative lens fixture designs and received Memorandum of Innovation.

Akhil plans to pursue a career on nanofabrication, development and packaging of novel photonic crystal devices for LiDAR and 3D sensing applications. He is a recipient of Student Employee Award of Excellence in 2020 from UTA.